Quantitative Determination of Residual Stress on Additively Manufactured Ti-6Al-4V

by

Mercedes M. Ferraro

Submitted in Partial Fulfillment of the Requirements

for the Degree of

Master of Science in Engineering

in the

Mechanical Engineering

Program

YOUNGSTOWN STATE UNIVERSITY

May, 2018

Quantitative Determination of Residual Stress on Additively Manufactured Ti-6Al-4V

Mercedes M. Ferraro

I hereby release this thesis to the public. I understand that this thesis will be made available from the OhioLINK ETD Center and the Maag Library Circulation Desk for public access. I also authorize the University or other individuals to make copies of this thesis as needed for scholarly research.

Signature:

Mercedes M. Ferraro, Student	Date

Approvals:

Dr. Jae Joong Ryu, Thesis Advisor	Date
Dr. Hazel Marie, Committee Member	Date
Dr. C. Virgil Solomon, Committee Member	Date
Dr. Salvatore A. Sanders, Dean of Graduate Studies	Date

Abstract

Additive manufacturing (AM) is a method to build a three-dimensional part through the layering of material. One category of AM, Direct Energy Deposition (DED), is commonly used with the titanium alloy, Ti-6Al-4V, and has shown to be useful for aerospace, transportation, and biomedical applications. However, the DED process induces anisotropic material properties due to the nonuniform temperature distribution, which causes residual stresses. In addition, when handling titanium and its alloys, the processing history and post-heat treatment greatly influence the microstructure, residual stresses, and mechanical properties. Previous research has been done to investigate the residual stresses by methods such as X-ray diffraction, contour methods, and finite element simulations. However, a less established technique for determining the residual stresses is through nanoindentation. Nanoindentation is the use of instrumented indentation to determine the mechanical behavior and properties of a small volume based on the load versus depth results. By applying nanoindentation techniques to a DED Ti-6Al-4V, it was found that the nanoindentation results varied based on the cross-sectional height of the sample. The reason for this occurrence was believed to be due to the microstructure and the existence of residual stresses. The nanoindentation results were then used to quantify the residual stresses present in the DED Ti-6Al-4V part using the basic methodology of Suresh and Giannakopoulos. Similar to the nanoindentation hardness and elastic modulus results determined, the residual stresses also showed an increasing trend when increasing in height along the cross-section. More specifically, as the height along the build direction increased, the residual stresses present increased in compressive behavior. However, future work is required to verify the validity of the

Suresh model and its application to DED Ti-6Al-4V. Ultimately, by understanding the material characteristics of this part, it would help to further enhance the structural integrity of AM parts.

Acknowledgements

Firstly, I would like to send my gratitude to my advisor, Dr. JJ. Not only have you lent your knowledge and guidance in this research, but you have also done so in my undergraduate experience, which I am thankful for. I can always count on you for your truthful advice and patience. No matter how many questions I have (or anyone has), you always help to the best of your ability. I would also like to thank my committee members, Dr. Marie and Dr. Solomon. For this research, I appreciated your support, feedback, and suggestions. For my entire undergraduate and graduate experience, I feel you both always had my best interest in mind. Also, if it wasn't for Dr. Marie's insistence and assistance, I probably would not have furthered my education. Another person I would like to give my appreciation to is Kelsey Lyda. Your huge heart, advice, and moral support is valued by everyone you encounter.

In addition, this research's quality was further heightened by the assistance of Matt Caputo and Christina Seydlorsky. Thank you for your help even when you had a busy schedule. Furthermore, I would like to thank all of my fellow researchers, past and present, for their knowledge, assistance, and support. This would include Qasim Riaz, Sanjay Shrestha, Angelo Pelini, Yash Trivedi, Ed Cudjoe, and Mihir Patel. Most importantly, Sanjay, thank you for your patience, especially in teaching me the ways of the polishing, mounting, and indenting machines. Also, thank you for your guidance, suggestions, and setting of a seemingly unattainable standard for work ethic.

Additional people, organizations, and companies that I would like to thank are Jeff Tomita, Nanovea, Tim Styranic, Youngstown State University, and the YSU Mechanical Engineering Department.

Lastly, I would like to thank my family for their continuous support and love. During this period of my life, my parents and brother were my support system. The ears that would listen to me, but also the arms to ease my worries. But for my entire life, you have guided, helped, and loved in an indescribable way. I appreciate and will continue to appreciate everything you do for me.

Table of Contents

List of Figures

List of Tables

Nomenclature

Ti6Al4V	Titanium 6-Vanadium 4-Aluminum
AM	Additive Manufacturing
EDM	Electrical Discharge Machining
CMM	Co-ordinate Measurement Machines
ASTM	American Society for Testing Materials
ISO	International Organization for Standards
XRD	X-ray Diffraction
FDM	Fused Deposition Modeling
SL	Stereolithography
PC	Polycarbonate
LOM	Laminated Object Manufacturing
3DP	Three-Dimensional Printing
SLS	Selective Laser Sintering
SLM	Selective Laser Melting
EBM	Electron Beam Melting
DLD	Direct Laser Deposition
DMLS	Direct Metal Laser Sintering
DED	Direct Energy Deposition
LENS	Laser Engineered Net Shaping
ABS	Acrylonitrile Butadiene Styrene
PPSF	Polyphenylsulfone

HCP	Hexagonal Closed Packed
BCC	Body Centered Cubic
SEM	Scanning Electron Microscope
EDS	Energy-Dispersive X-Ray Spectroscopy
HAZ	Heat-Affected Zone
MEMS	Microelectromechanical Systems

Chapter 1: Introduction

1.1 Residual Stress

1.1.1 Basics

The existence of residual stresses in structural components and parts is important to understand due to their effect on structural integrity and mechanical behavior. Residual stress, or internal stress, exists when a part experiences a stress distribution without the application of an external load. Residual stresses can either be in tension or compression and need to be balanced to achieve equilibrium in the part. In addition, these stresses can be present in a variety of materials, such as metals, ceramics, and glasses.

Residual stresses can be found in various components and are developed through inhomogeneous plastic deformation and manufacturing processes. Inhomogeneous plastic deformation can arise when a part with a stress riser is pulled in tension [1]. The area around the stress riser could go beyond the yield strength of the material and a plastic region could be formed [1]. Thus, plastic deformation in a localized area will occur [1]. However, once the load is no longer applied, the plastic zone would still exist and there would be internal compressive forces acting on it [1]. This phenomenon is what occurs in plastic hole expansion. For example, a hole, such as in rivet joints, is expanded to cause plastic deformation [1]. Once the external load is released, compressive forces would act around the hole, which would improve the fatigue resistance of the part [1].

Further manufacturing processes and material handling that induce residual stresses include machining, welding/joining, additive manufacturing (AM), surface rolling, shot peening, and heat treatment. When welding, the joining of two materials could cause non-uniform thermal strains, therefore leading to induced tensile stresses [1].

This would be detrimental to the part and lower the fatigue life [1]. Large thermal gradients are also present when coatings are created for optical fibers, which creates internal stresses due to a mismatch in thermal expansion [2]. The thermal mismatch is also seen in semiconductors, which can either lead to a shorter lifetime for the part or, if the appropriate amount is present, the mobility of charge carriers and the speed of the device could improve [3]. Machining, surface rolling, and shot peening can induce residual stresses through plastic deformation and thermal effects as well. The residual stresses produced through machining are undesirable due to the lower fatigue life that could occur; however, with shot peening, the compressive residual stresses may help to prevent fatigue or stress corrosion [1].

As for additive manufacturing and heat treatment, the residual stresses could have both positive and negative effects on a material or part depending on the conditions used. For instance, with heat treatment, if the material is rapidly cooled or quenched, inhomogeneous cooling temperature would occur throughout the part and thermal stresses would be induced [1]. However, an appropriate heat treatment of additive manufactured parts that have residual stresses due to thermal strains could reduce the internal stresses.

A common method for decreasing the residual stresses in AM parts is through heat treatment, which includes annealing or putting the material through a stress relief cycle. These treatments usually occur at low temperatures, such as around 650°C for Ti-6Al-4V ranging from two to four hours [4]. In a study done with Ti-6Al-4V additively manufactured using the laser engineered net shaping (LENS) method, it was determined that after an annealing treatment, the internal stresses of the part reduced by 72% [5]. The

amount of stress relief is dependent on numerous factors, such as the processing parameters before the heat treatment, the temperature at which the relief occurs, and the duration of the heat treatment. The proper heat treatment of AM parts can not only decrease the internal stresses, but it can also decrease porosity and alter the microstructure to enhance the mechanical behavior. Even though this post-processing strengthens the material, it would be more beneficial if the AM process itself would account for temperature variations and porosity.

It has been determined that reducing the temperature gradient between each layer could decrease the residual stress [6]. This could be done through the manipulation of processing parameters. For example, when increasing the thickness or height of the part, it has been seen to reduce the amount of residual stresses [5-7]. This is due to the continuous reheating and greater accumulation of heat at the layers, therefore lowering the thermal difference [5]. In addition, minimizing the energy input has been seen to decrease internal stresses in AM parts [5]. More specifically, by increasing the energy, it would lead to a larger melting pool and larger contractions of the layers when solidifying, resulting in greater stresses along the horizontal direction of the build [5]. Furthermore, the scanning length has also shown to affect the amount of internal stresses in the horizontal direction [5]. If the scanning length is too large, the material could have varying localized temperatures, which would cause greater stresses [5]. Thus, it is important to be able to determine the residual stresses and the effects of the processing parameters to enhance the additive manufacturing process and durability of the parts that are produced.

1.1.2 Determination Methods

There are various destructive and non-destructive methods to quantify existing residual stresses in materials. Typically, a stress-free or stress-relaxed surface of the same material is required to compare and determine the residual stress. Some destructive tests include analyzing a cut surface or drilling a hole in a specimen. For example, the contour method requires the cutting of a material using wire-Electrical Discharge Machining (EDM) [8]. At the free surface, the residual stresses are relaxed, and the material consists of noticeable distortions that can be mapped using co-ordinate measurement machines (CMM) [8]. Then, using a finite element model and applying the inverse of the surface contour, the resulting stresses of the model would be the initial stress state of the part [8]. As for the hole drilling method, it is in accordance with ASTM E837-00 for drilling [6]. It utilizes the boring of a small hole into a specimen to relax the nearby stresses, while a strain gage tracks the changes in strain simultaneously [6]. However, factors such as the hole depth, the bonding of the strain gages, and the possible addition of stress could affect the accuracy of the measured results [9,10]. In addition, the destructive nature of these tests would have limited applications in industry, unlike non-destructive tests [10].

Some non-destructive methods include using Raman spectroscopy, X-ray diffraction (XRD), and nanoindentation techniques. For example, when utilizing a Raman spectrometer on a material, spectra can be obtained [2]. Based on the shift in the peak positions of the Raman spectra, the residual stresses can be determined [2]. This method is typically applied to non-metals [9]. However, one of the most common and established methods for finding residual stress is by X-ray diffraction [11]. This technique compares the interplanar spacing for stressed and unstressed lattices [11]. The lattice deformations

are determined using a radiation source and the residual stresses are computed based on plane stress conditions using X-ray elastic constants [5,7,11,12]. However, with this method, the measurements taken are only near the surface due to the shallow penetration of the x-rays [9,10].

A less established technique is the utilization of nanoindentation. Nanoindentation is the use of instrumented indentation to determine the mechanical behavior and properties of a small volume based on the load versus depth results [3,9]. Furthermore, common materials used include bulk solids, thin films, and coatings [3,9]. It has been proven that residual stresses affect the nanoindentation hardness, loading curve, unloading curve, material pile-up, and contact area [3,9]. This has led to the derivation of various models, such as the Suresh Model, Lee Model, Xu Model, and Swadener Model, which focuses on the use of different characteristic parameters and indenter types to calculate the residual stress [3,9]. Each nanoindentation model has its own assumptions, material applications, and limitations. For example, the Suresh, Lee, and Xu Model utilizes sharp indenters and assumes equi-biaxial stresses [3,9]. In addition, the Swadener Model considers a spherical indenter due to the belief that it is more sensitive to the stress effects, such as the change in area [3,9]. However, this model assumes a biaxial stress and may require a large indenter radius to achieve accurate results [3,9]. Experimentations have been conducted to compare the differences in stress results of the nanoindentation models. For instance, when nanoindentation measurements were conducted on aerospace aluminum alloys, the sharp-based indenter models, Suresh and Lee, were used [13]. It was noticed that the methods agreed with each other, whereas there was only a slight deviation when the applied compressive or tensile stresses were relatively large [13]. This discrepancy is related to the

assumption that Lee considers the residual stress to behave linearly, whereas, Suresh assumes non-linearity in the compressive and tensile regions [13].

Numerous studies have applied and compared the mentioned traditional non-destructive techniques with nanoindentation. It has been reported that there can be a high variability when measuring residual stresses due to the results being sensitive to metallurgical factors, like grain size, texture, and environmental factors [10]. More specifically, a study was performed on ceramic thin films in which residual stress was approximated based on the X-ray diffraction and nanoindentation (Suresh) method [9,11]. It was determined that the stresses determined by the Suresh Model were three times larger than the stresses computed from the X-ray diffraction [9,11]. This result could be due to the material not having the relatively fine grain size that is required for the X-ray diffraction method [13]. However, another experiment was conducted for stress analysis on aluminum films of multiple thicknesses using continuous indentation and X-ray diffraction [14]. It was concluded that the results were comparable between the two methods when the thickness was relatively small [14]. This phenomenon could be due to the greater variation of stresses throughout the thicker part and the techniques' lack of penetration [14]. Another study was conducted on carbon-coated optical fibers that exhibited thermally induced residual stresses [2]. Utilizing a theoretical model for the stress state of the carbon-coated optical fiber, Raman spectroscopy, and the Suresh model for indentation, the residual stresses were quantified [2]. It was concluded that the behaviors of the measured and theoretical stresses agreed, and the experimental results showed to be within experimental uncertainty of the theoretical [2].

1.2 Additive Manufacturing

Additive manufacturing (AM) is the technique of using a computer model to create a three-dimensional part. This part is built one layer at a time and can be made from a variety of materials, such as plastics and metals. A common application of AM is rapid prototyping. Rapid prototyping allows for the creation of preliminary parts to be used as visual aids and models, as well as the ability to understand the functionality or assembly of the components before production [15]. Therefore, this process greatly enhances the product development cycle [15]. Other AM advantages include the potential to lower manufacturing cost, decrease the building time, and create complex geometries or customizations [16,17]. These benefits make the application of AM appealing to aerospace, transportation, and biomedical industries [17]. For instance, it gives the potential to manufacture lighter structures to reduce the weight of an automobiles' or aircrafts' components [15]. Furthermore, a continued topic of interest is the use of AM with biocompatible materials to customize hip, knee, or dental implants for patients. AM allows for the control and manipulation of density and porosity, which could benefit the fusion of the implant to tissue and bone, as well as the strength of the implant [15].

1.2.1 Types

There are many types of AM approaches and technologies, which can be divided into liquid, solid, and powder-based systems. For liquid-based, common processes include Fused Deposition Modeling (FDM), Stereolithography (SL), and Polyjet. FDM utilizes melting and extruding to build various polycarbonate (PC) parts [15]. This process allows for no chemical post-processing, yet the resolution to achieve a smooth surface finish is low [15]. For SL and Polyjet, the means of manufacturing is through polymerization. More

specifically, this polymerization occurs when an ultraviolet light is applied to a liquid polymer, where it reacts to cause solidification [15]. SL is widely used and is more durable than Polyjet, even though there is potential for the over-curing or over-hardening of the polymer [15]. As for solid-based, the predominately used process is Laminated Object Manufacturing (LOM). LOM relies on applying heat, pressure, and a thermal coating to sheet materials to build a cohesive part [15]. With this method, there is no phase change or necessity for a supporting structure; however, complex geometries cannot be achieved [15].

An additional category of AM is the powder-based processes, which includes Three-Dimensional Printing (3DP), Prometal, Selective Laser Sintering (SLS), Electron Beam Melting (EBM), and Laser Engineered Net Shaping (LENS). 3DP and Prometal uses a jet to supply liquid binder to powder particles to build the part [15]. 3DP is similar to inkjet printing and does not required a phase change for the process [15]. However, SLS, EBM, and LENS focus on the melting of the deposited layer to build the part. The source for solidification of the powder layers includes an electron beam or a laser [15]. For instance, EBM uses an electron laser beam in a vacuum chamber to inhibit oxidation in metal parts [15]. SLS is similar to EBM in its deposition process, yet a wider range of materials can be used [15].

However, the AM process of interest is direct energy deposition. Laser engineered net shaping (LENS) is a subcategory of a method called direct energy deposition (DED) or direct laser deposition (DLD), which commonly manufactures parts from metal powders or wires [16,17]. DED utilizes an energy source, like a laser, to melt materials together in a layered fashion [18]. The LENS process takes place inside an inert gas atmosphere and is depicted in Figure 1 [16]. In this powder fed system, a melt pool is made on a substrate

(build material) by a focused laser beam [17]. Metal powder is then inserted in the melt pool, which eventually forms a bead of material at the end of a nozzle [17]. This deposition from the nozzle is translated until the layer is complete [17]. Then, the nozzle moves vertically relative to the surface to continue the next layer deposition [17]. Thus, the build direction, as well as other processing parameters to make the part, could be varied.

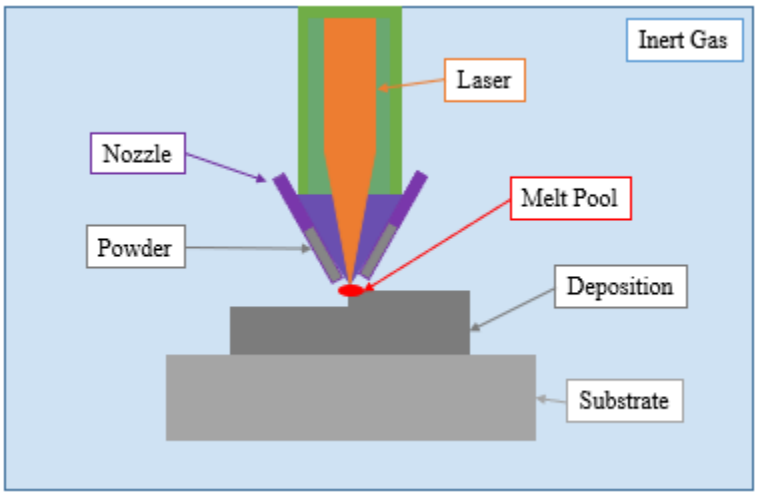

Figure 1. Direct Energy Deposition (DED) Setup

With DED, it has the capability to handle materials with high melting temperatures and build fully dense parts with equal or better mechanical properties compared to traditional manufacturing techniques [18]. Yet, there are some disadvantages that arise regarding powder delivery, porosity, and control of material properties [18]. It has been reported that DED parts exhibit anisotropic or variable properties [18]. This is believed to be due to the existence of pores and unmelted material from the inhomogeneous cooling rate and inconsistencies in the temperature distribution in the deposition [18]. Furthermore, the pores can act like stress concentrators in the part, potentially weakening the strength and fatigue resistance [16]. In addition, the continuous reheating and remelting of the top-most layer during the DED process is attributed to irregularities, like residual stresses, in

the part as well [16]. However, a post-heat treatment can make the part more uniform [16]. Figure 2 depicts the flow of influential factors associated with DED [16]. To achieve ideal functionality of the AM specimens, an understanding of the processing parameters is necessary due to their effects on microstructure and mechanical properties [16-18]. Processing parameters include laser power, layer thickness, scanning strategy, and scanning speed [16]. Common parameters used in the process can be seen in Table 1 [19].

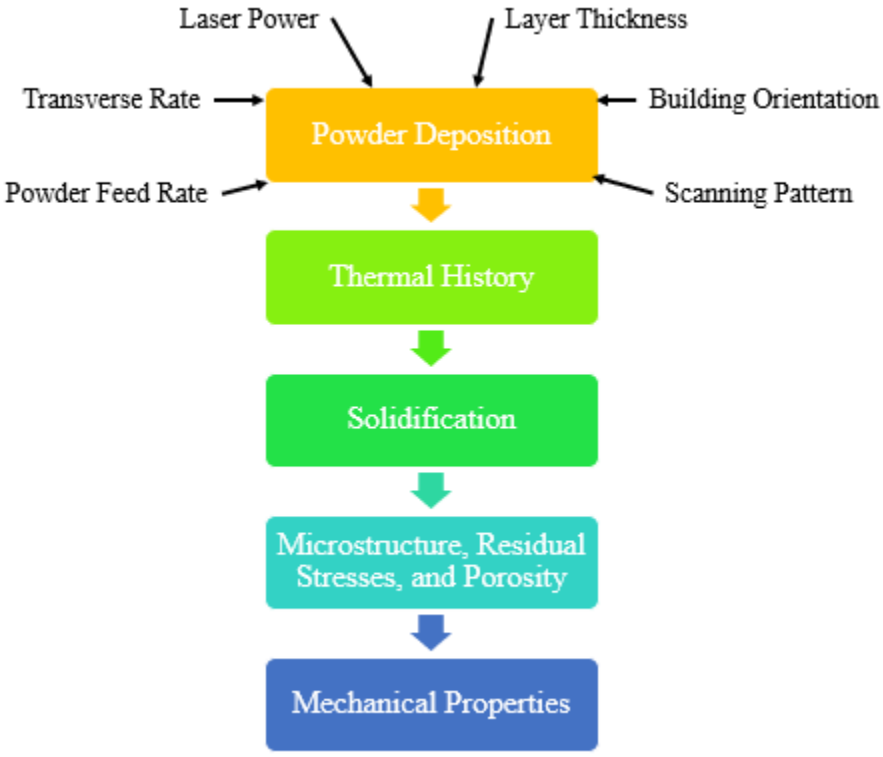

Figure 2. Flow of Influential Factors for DED Process

Table 1. Common LMD Process Parameters

Typical Equipment	Triumpt HLD 3504
Build Volume	250 mm x 250 mm x 400 mm
Powder Supply	3.5 kW max.
Laser Beam Size	500 μm – 4100 μm
Atmosphere During Processing	Argon Flow Protection
Scanning Speed	2 mm/s – 40 mm/s
Feed Type	Powder: 10 μm – 200 μm Wire: 1.2 mm – 1.6 mm
Layer Thickness	40 μm – 100 μm
Build Temperature	Naturally Heated
Build Density	>99.9%
Substrate	Ti-6Al-4V or Ti (room temperature or preheated to 200°C

1.2.2 Materials

The variety of materials that can be used in conjunction with AM is continuing to expand. It is believed that additional research and investigations need to be implemented for AM technology to handle more commonly used manufacturing materials [15,20]. Once this is accomplished, AM will further become a standard in industry, even though steps have been taken to standardize terminology and file formats by the American Society for Testing and Materials (ASTM) through ASTM F2792 and ASTM F2915, respectively [15,20]. On the other hand, the possibility to produce parts in which it is difficult to conventionally machine, like with composites and ceramics, is advantageous for AM [21]. Currently, different AM processes have limited or ideal materials that can be used accordingly. For example, when producing plastic composites with reinforced fibers, SL and LOM are the favored processes [21]. However, when considering FDM,

polycarbonates (PC), acrylonitrile butadiene styrene (ABS), and polyphenylsulfone (PPSF) are typical materials that are used [15]. Metals are also frequently used in the AM processes, such as EBM, Prometal, SLS, and LENS [15]. Commercially used metal alloys include nickel, copper, aluminum (Al-Si-Mg, 6061), stainless steels, titanium (Ti-6Al-4V, ELI Ti), and super alloys (IN625, Stellite) [20].

One of the most investigated and commonly used metal with AM metal processes is the titanium alloy, Ti-6Al-4V. In 2012, the use of Ti-6Al-4V was standardized through ASTM F2924 Specification for AM Titanium-6 Aluminum-4 Vanadium with Power Bed Fusion [20]. Ti-6Al-4V has proven to be useful in the aerospace and biomedical fields due to its high strength, high melting point, biocompatibility, high stiffness to weight ratio, and corrosion resistance [16,18]. For casted Ti-6Al-4V used in the biomedical field, the density is 4.43 g/cm^3, with the yield and ultimate tensile strengths being 847 MPa and 976 MPa, respectively [18]. Further physical properties of Ti-6Al-4V can be seen in Table 2 [19]. With AM processes, including DED, it is believed to enhance the properties of Ti-6Al-4V by increasing its strength and toughness [18]. It has been reported that, based on the ASTM requirement for the material properties of Ti-6Al-4V, the ultimate tensile strength for LMD, EBM, and SLM samples tests have surpassed the standard [19]. For example, it has been documented that the ultimate tensile strength for a Ti-6Al-4V sample manufactured by SLM reached as high as 300 MPa beyond the requirement of approximately 875 MPa [19]. Another factor that could affect the material strength is the post-heat treating. Heat treating can increase the ductility of the material and is common for SLS and SLM due to the components' reported nonuniform density [19].

Table 2. Physical Properties of Ti-6Al-4V

Density of Solid	4.43 g/cm^3
Density of Liquid	3.89 g/cm^3
Solidus Temperature	1877 K (1604°C)
Liquidus Temperature	1933 K (1660°C)
Temperature of (α+β) to β	1253 K (980°C)
Temperature of α to β	1023 K (750°C)
Thermal Conductivity of Solid	6.7 W/m-K
Thermal Conductivity of Liquid	32.5 W/m-K
Specific Heat Capacity of Solid	0.526 J/g-K
Specific Heat Capacity of Liquid	0.872 J/g-K
Coefficient of Thermal Expansion of Solid	8.6 μm/m-K
Temperature of Martensite Phase Transformation	883 K (610°C) or 1053 K (780°C)

1.2.3 Microstructure

For titanium, it consists of two main crystal structures, which includes hexagonal closed packed (HCP) α and body centered cubic (BCC) β. By adding alloying elements, they can either stabilize the α phase or stabilize the β phase, which would alter the transition temperature from α to β [22]. Thus, there are three categories of titanium alloys, which include α, β, and α + β alloys [22]. For α alloys, the combination of elements like aluminum and tin would stabilize the α phase [22]. For β alloys, titanium and the addition of vanadium and tantalum would stabilize the β phase [22]. Therefore, Ti-6Al-4V, which is an α + β alloy, exhibits a mixture of α and β stabilizers.

Titanium alloys' microstructure and mechanical properties are heavily related to the processing history and post-heat treatment [22]. Based on the processing with relation to the β transus (temperature at which α transforms to β), primary α may exist as extended

plates or equiaxed circular morphologies [22]. This could be due to deformation and the cooling rate of the material [22]. For instance, primary α after a sufficient amount of time above the β transus temperature should not exist [23]. However, if the phase is slowly cooled from the α + β region or above the transus temperature, it will transform into globular or primary α [23].

In addition, transformed β can have various morphologies, including plate-like, Widmanstätten, acicular, and α' [22,23]. Plate-like α morphologies result when slow cooling from the β field is achieved [23]. Furthermore, the structure will become coarser as the cooling rate is decreased [23]. As for the Widmanstätten structure, it can exist as needle-like, acicular grains or coarse, plate-like α phase [23]. This distinction depends on the rate of cooling, which affects the nucleation of the α phase on the β grain boundaries [22,23]. If the cooling rate is sufficiently fast, the nucleation of the α phase may exist not only on the grain boundaries, but also inside the prior β grains [22,23]. This would result in finer grains and may be considered as a basket-weave structure [22]. However, another possibility for the rapid cooling from the α + β phase is that the β phase can transform to a martensitic type α phase [22,23]. This metastable phase could consist of α' (hexagonal structure), α'' (body center tetragonal), and metastable β [22,23]. The structure of the β phase is related to the composition of β before rapid cooling [22,23].

For the DED process especially, there are also three distinct morphologies, which include columnar, columnar plus equiaxed, and equiaxed [16]. Equiaxed grains are defined as being equal in length based on all directions. The resultant microstructure depends on the local solidification rate of the melt pool, the solid-liquid interface temperature gradient, and the rate of cooling [16]. Characteristically, elongated columnar β grains exist in the

build direction on the macro-scale [16]. With columnar grains, the grain size in the direction perpendicular to the build direction tends to be smaller compared to the parallel direction [16]. This could relate to the anisotropic behavior in mechanical texture [16]. On the micro-scale, finer Widmanstätten structures usually exist at the top and bottom of the part [16]. This phenomenon is related to the top and bottom regions of the deposition having higher cooling rates, thus having finer microstructure, and resulting in greater hardness [16]. Overall, the α and β ratios can vary throughout the microstructure due to the reheating and cooling of the deposition. This inherently can affect the mechanical properties when considering that the β phase is more ductile, while the α phase is stronger [22].

1.2.4 Residual Stress in Additive Manufacturing

The documented anisotropy of DED materials is directly related to the processing parameters, which affects not only the microstructure, but the amount of residual stresses induced by the AM processes. With the additive manufacturing processes such as DED, SLM, and SLS, a high-power laser is utilized to liquify and solidify the material in a layer by layer fashion to build a part [6]. The laser beam size has been seen to range from 70 microns to 4100 microns with laser power varying from about 200 W to 940 W [18,19,25,26]. This laser energy source generates heat during the AM process, and the amount of heat in the part results in the amount of residual stresses [6]. Ideally, the amount of heat stored in the component should be minimized through the materials' ability to conduct heat [6]. This thermal phenomenon is inherent of the process. For instance, when a layer of material is deposited and solidified, and another layer of material is deposited on top of that, a temperature gradient between the two layers will exist due to the heating of

the top layer [6]. In addition, the heat will travel slowly through the previously placed layer [6]. The top layer will also experience expansion, cooling, and then shrinking [6]. This heating of the layer will also lower the yield strength, which in turn constrains the movement and results in plastic strains [6].

The existence and magnitude of residual stresses can affect the functionality of a part. For instance, it has been documented that residual stresses affect the mechanical behavior, such as fatigue strength, fracture toughness, and wear resistance, leading to a modified service life [3,6]. For instance, when compressive residual stress fields exist in areas where crack propagation will initiate, the fatigue strength is believed to be increased [6]. This further relates to components that have an externally applied tensile load. In this case, the existence of compressive residual stresses could decrease crack propagation, whereas tensile residual stresses could increase crack propagation [3]. In addition, large tensile residual stresses increase the cyclic stress state of a part [27]. Therefore, determining the causes and magnitude of residual stresses is imperative to understand the material and part functionality.

1.3 Research Objectives

The existence of residual stresses in structural components is important to understand due to their effects on material integrity and mechanical behavior. Through using traditional methods for finding residual stresses, it has been discovered that AM parts exhibit a stress distribution throughout the material. The occurrence of residual stresses is predominantly found in the processes that induce large thermal gradients, such as DED, SLM, and SLS. Due to these stresses, as well as the pores and defects that have also been displayed in AM parts, the fatigue behavior is greatly affected. However, the

amount of residual stresses and mechanical behavior have varied based on previous investigations due to the numerous processing parameter combinations that could be used. To continue the investigation of DED Ti-6Al-4V, the behavior of the mechanical properties, the microstructure, and the residual stresses have been investigated. Thus, this research could be used to potentially optimize the AM process and the parameters to engineer and create components that are of the utmost quality.

In addition, the technique for determination of the residual stresses was based on the nanoindentation model previously derived by Suresh and Giannakopoulos. Suresh and Giannakopoulos created what is believed to be the first general methodology for the influence of nanoindentation due to residual stress; however, other researchers have continued the work and incorporated experimental data and finite element models to compare and modify the theory. Therefore, for this research, the experimental results are believed to be a contribution to further verify the model. In solidifying the use of nanoindentation to determine residual stress, it could potentially become a standardized method that would be convenient and efficient for industrial applications.

1.4 Thesis Outline

This paper starts with outlining the necessary background information. Chapter 1 covers a range of topics from the creation of residual stresses, the determination of residual stresses based on traditional means, and the potential use of nanoindentation for stress estimation. Further introductory ideas include additive manufacturing, common processes that have been utilized, ranges of materials that can be used, and how residual stresses play a role in AM parts. In addition, specific features such as the direct energy deposition

process and Ti-6Al-4V were covered due to their importance in the experimental research further presented.

The investigation into the material properties of DED Ti-6Al-4V are explained in Chapter 2 through Chapter 5. Chapter 2 examines the microstructure and chemical composition of the DED Ti-6Al-4V sample. An image analysis and EDS results are presented to understand the variation of phases and composition on the cross-section of the DED sample. Chapter 3 and Chapter 4 outlines the use of nanoindentation to understand the hardness and elastic modulus of the material with respect to the distance along the build height. The difference between Chapter 3 and Chapter 4 is based on the nanoindentation technique. Chapter 3 describes the use of single load cycle and the results found, whereas, Chapter 4 utilized multi-load cycle indentation. Chapter 5 further investigates the experimental data previously found in Chapter 3 and Chapter 4 to determine the potential amount of residual stress along the cross-section of the DED Ti-6Al-4V sample.

The paper ends with Chapter 6, which depicts the overall conclusion and future work that could be done to further clarify the results of this study.

Chapter 2: Microstructure

2.1 Introduction

The titanium alloy, Ti-6Al-4V, has two main crystal structures, which are HCP α and BCC β. Based on the alloying elements, the β transus temperature can be altered. Thus, processing and post heat-treatment related to the β transus temperature can change the phases and microstructure. More specifically, in AM processes, the microstructure depends on the local solidification rate of the melt pool, the solid-liquid interface temperature gradient, and the rate of cooling [16]. For example, the critical cooling rate for martensitic phase to form is approximately 410°C/s [17]. When using the AM process, Electron Beam Melting (EBM), it exposes the material to high temperatures for long periods of time and has a slow material cooling rate [17]. In turn, the Ti-6Al-4V microstructure decomposes the martensitic phase formed in the build solidification [17]. When using the DED process, a laser is utilized to continuously heat the material. As the part is built layer by layer, reheating and melting of the material happens before the final solidification. Therefore, an inhomogeneous temperature distribution throughout the part exists with a rapid cooling rate. This rapid cooling rate allows for the martensitic phase to permeate. However, the cooling rate and other factors can be altered by the laser power, scanning speed, or other processing parameters, thus varying the morphology of the microstructure [17].

Previous research has been done to investigate and further understand the effect of the processing parameters on the microstructure and mechanical properties of DED Ti-6Al-4V [17]. For instance, with an increase in power input, the ductility of a tensile test specimen has been seen to increase [17]. This occurrence could be due to the increased energy causing a higher cooling rate, which would result in a finer microstructure and less

porosity [17]. For example, a particular study compared the microstructure of low and high-powered lasers to further investigate the effects [17]. It was seen that for the low power condition, acicular α' phase was present, while for the high-power setting, a mixed microstructure of α'and α + β lamellae existed [17]. This was related to a slower cooling rate due to a higher energy input per unit time [17]. In addition, the thickness of the heat affected zone (HAZ) or interface between the substrate and deposition was affected as well [17]. Thus, a variation of resulting microstructures can appear with the DED process based on the chosen processing parameters.

The processing parameters for the DED Ti-6Al-4V sample under examination was built using standard techniques with a room temperature base plate of wrought Ti-6Al-4V that was 2 mm thick. In addition, the scanning pattern was considered parallel and no dwells were utilized. The total thickness of the part was approximately 4 mm. To understand the effects of the process and the mechanical properties, the microstructure was investigated.

2.2 Method

2.2.1 Image Analysis

The DED Ti-6Al-4V sample was made using standard AM techniques. The initial temperature of the substrate plate was 25°C. The DED Ti-6Al-4V was deposited as a 2 mm layer on wrought Ti-6Al-4V substrate of 2 mm thickness. To observe the microstructure of the DED Ti-6Al-4V sample, the sample was cut (using a diamond cut-off wheel and water at a speed of 550 rpm) in the center to expose the cross-sectional surface. The dimensions of the surface examined were then 13 mm in length and 4 mm in height. It was grinded, polished, and etched based on ASTM E3-11 standard [28]. The etchant used was Kroll's

reagent, which is a commonly used etchant for titanium. It consisted of 92 mL of water, 6 mL of nitric acid, and 2 mL of hydrofluoric acid. The sample was submerged in Kroll's reagent for less than a minute to reveal the microstructure. The DED Ti-6Al-4V sample was cleaned and then observed through an optical microscope. Images were taken of the wrought and deposited material. Furthermore, an image analysis was performed to determine the amount of α and β phases at different heights of the sample. Sixteen images were taken in a 4 by 4 grid, focusing on the interface between the substrate and the deposition, as well as the deposition. The image analysis was done using the software, ImageJ, which converted the microstructure images to a binary image. Thus, the α phases were depicted as white pixels and the β phases were assigned to be black pixels. By counting the number of pixels in the representative image, the ratio of α and β was determined. The phase ratios within each row of images were averaged due to the assumption that the microstructure would be similar for the same height along the sample.

2.2.2 Compositional Analysis

Using energy-dispersive X-ray spectroscopy (EDS) as an attachment of the scanning electron microscope (SEM), an elemental and compositional analysis was conducted. For the EDS technique, electrons are emitted to the sample surface [29]. This triggers electrons to form vacancies that are eventually filled from a higher state electron [29]. X-ray energy is then emitted to balance the difference in energy due to the electron [29]. The amount of x-ray energy thus corresponds to specific elements and the elemental amount can be determined [29]. Data was retrieved based on three different heights along the cross-section: the substrate, the interface, and the deposition (Figure 11). For each

height location, three points were selected to allow for a more accurate representation of composition. The three points were averaged based on weight percentage.

2.3 Results

2.3.1 Microstructure

The microstructural images along the cross-section with respect to height can be seen in Figure 3 through 7. The figures decrease in height, starting with Figure 3 at the deposition and ending with Figure 7 at the substrate. The vertical distance between each image is 0.67 mm, ranging over a 4 mm surface.

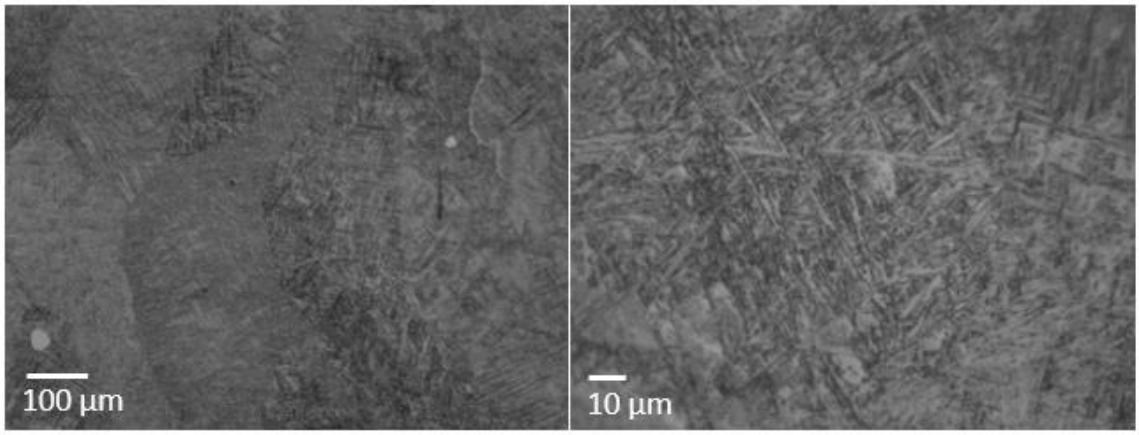

Figure 3. Microstructure at 3.34 mm from the Bottom (Deposition)

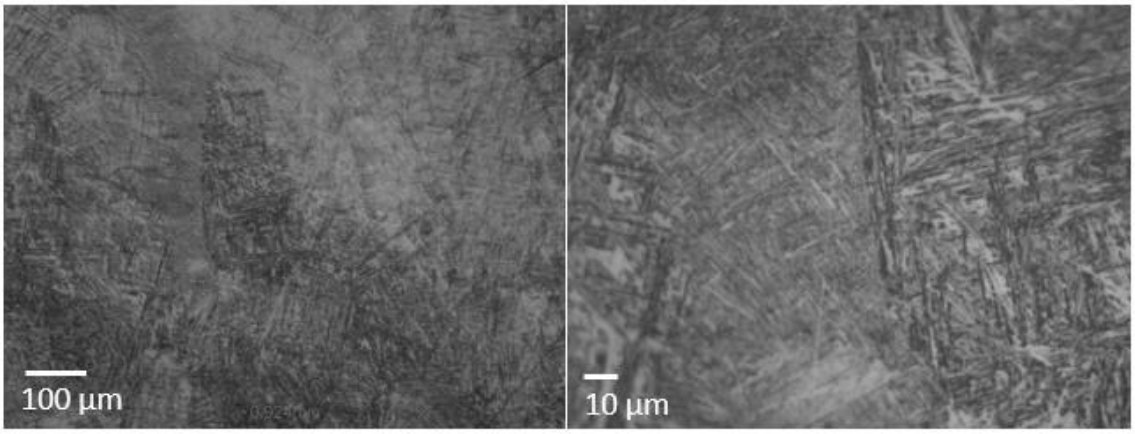

Figure 4. Microstructure at 2.67 mm from the Bottom (Deposition)

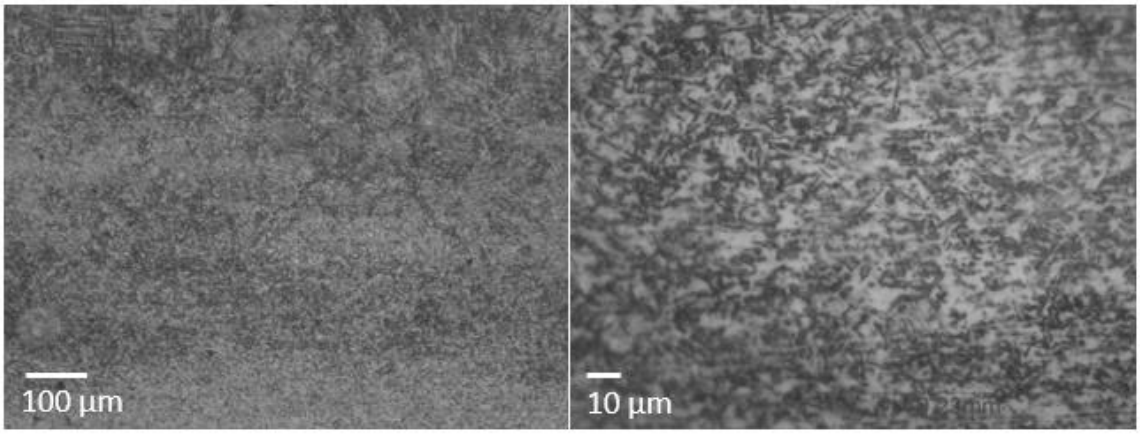

Figure 5. Microstructure at 2 mm from the Bottom (Interface or HAZ)

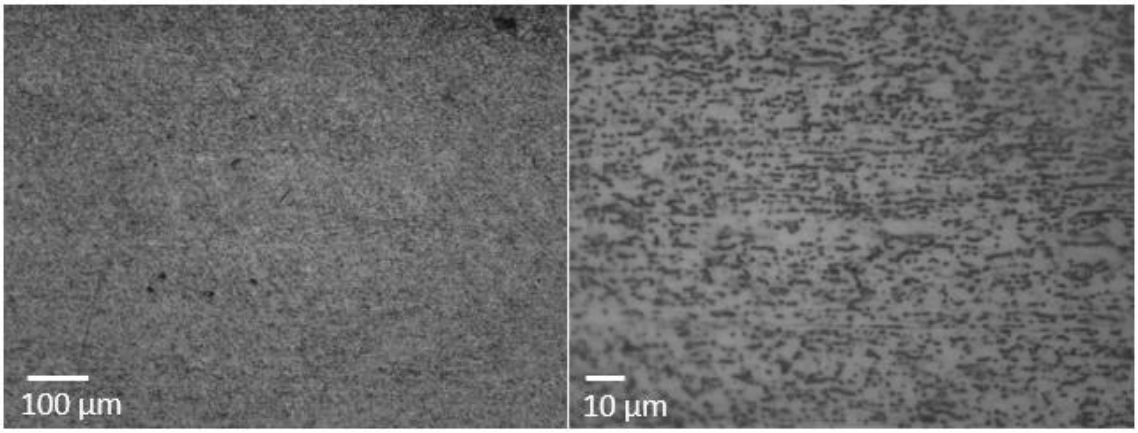

Figure 6. Microstructure at 1.34 mm from the Bottom (Substrate)

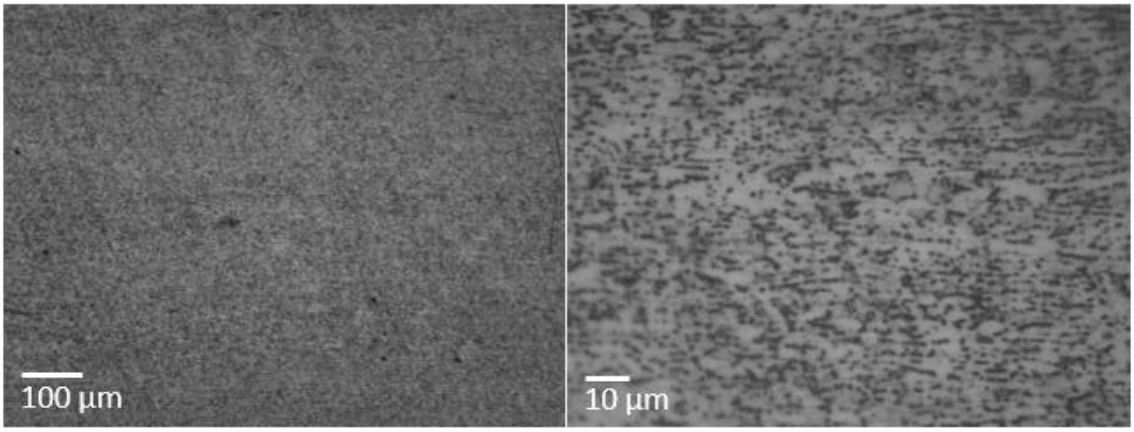

Figure 7. Microstructure at 0.67 mm from the Bottom (Substrate)

2.3.2 Image Analysis

The image analysis was performed along the deposition, as can be seen in Figure 8. A representation of the microstructure image and the conversion to a binary image is presented in Figure 9. The area chosen for Figure 9 corresponds to position 1 in Figure 8.

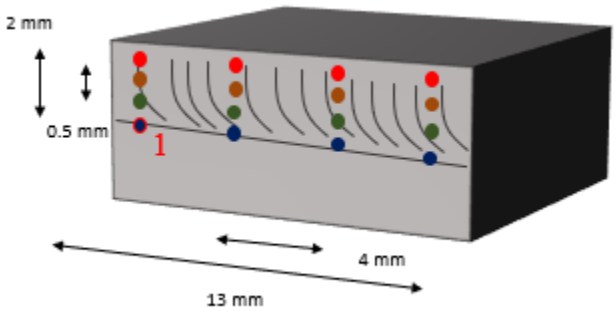

Figure 8. ImageJ Analysis Positions

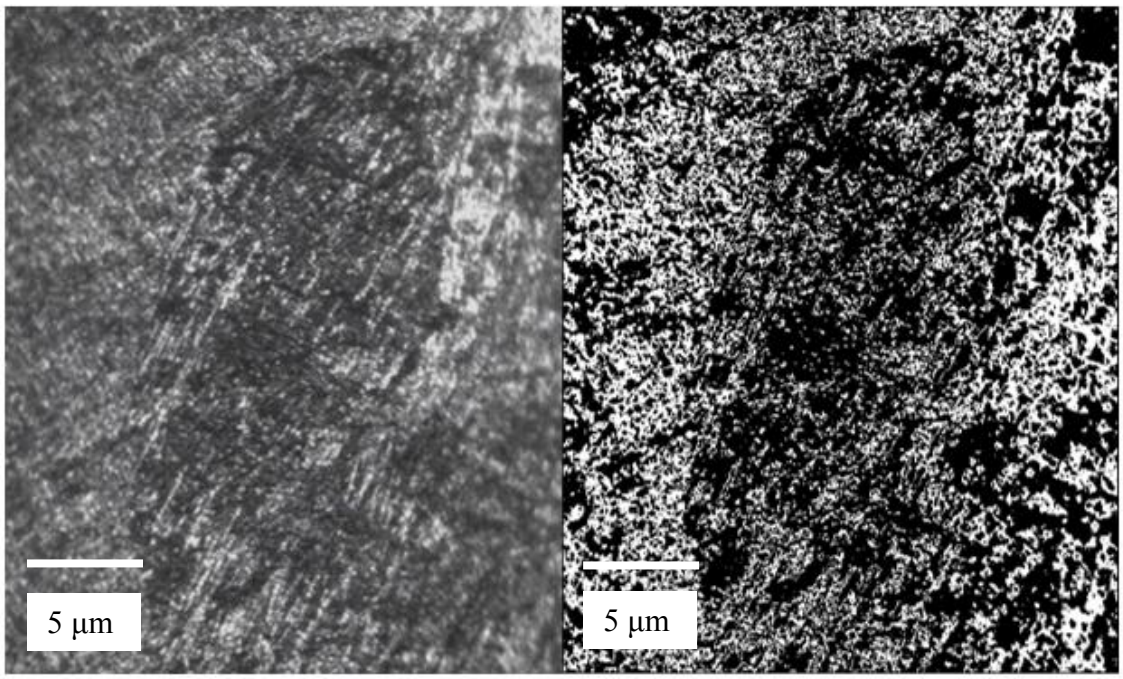

Figure 9. Microstructure Converted to Binary Image in ImageJ for Position 1

Based on the area ratios calculated in ImageJ for each position, the results were averaged based on the row or position from the bottom of the sample. The α ratio calculated with respect to height along the cross-section can be seen in Figure 10.

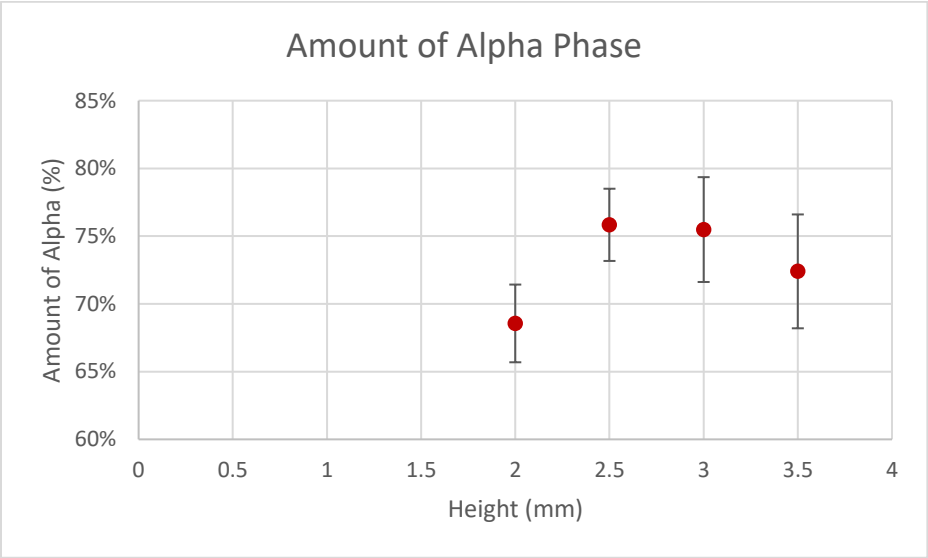

Figure 10. Amount of Alpha Phase Based on Deposition Height

2.3.3 Compositional Analysis

The location of the EDS results can be seen in Figure 11. For each position listed (A - Deposition, B - Interface, C - Substrate), three tests were performed in the vicinity and averaged together. The compositional results are shown in Figure 12 through Figure 14.

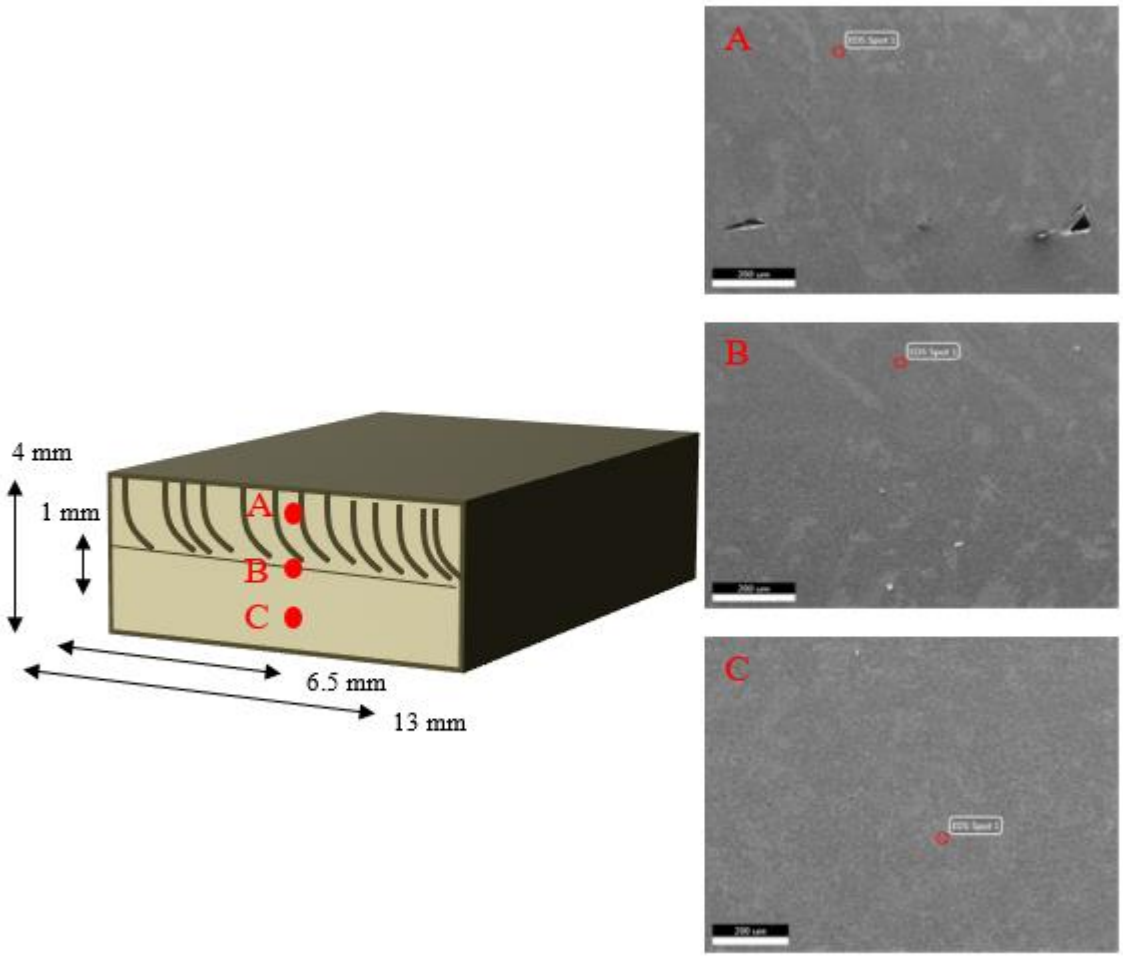

Figure 11. EDS Positions (A – Deposition, B – Interface, C – Substrate)

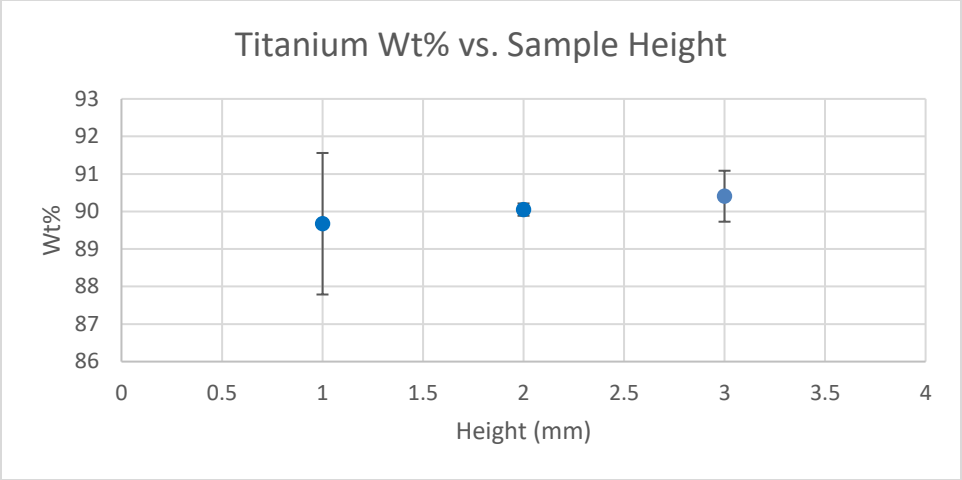

Figure 12. EDS Results for Titanium Composition

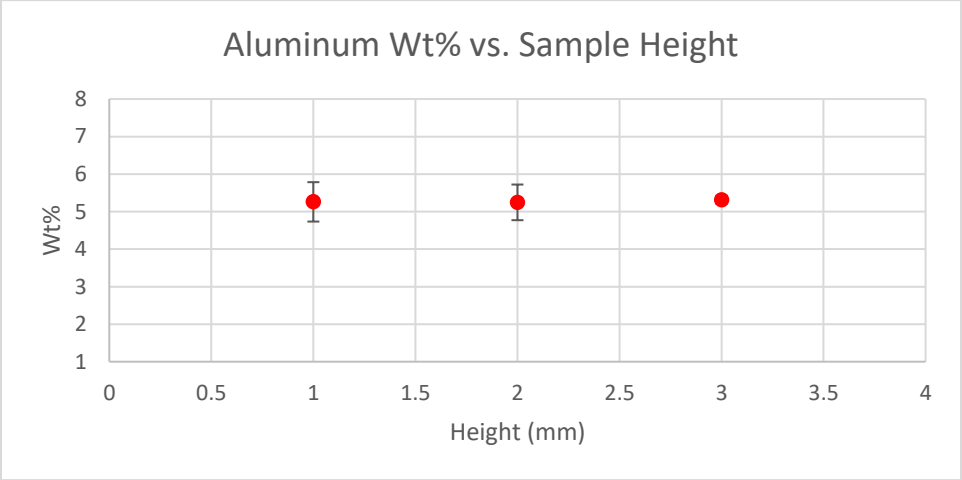

Figure 13. EDS Results for Aluminum Composition

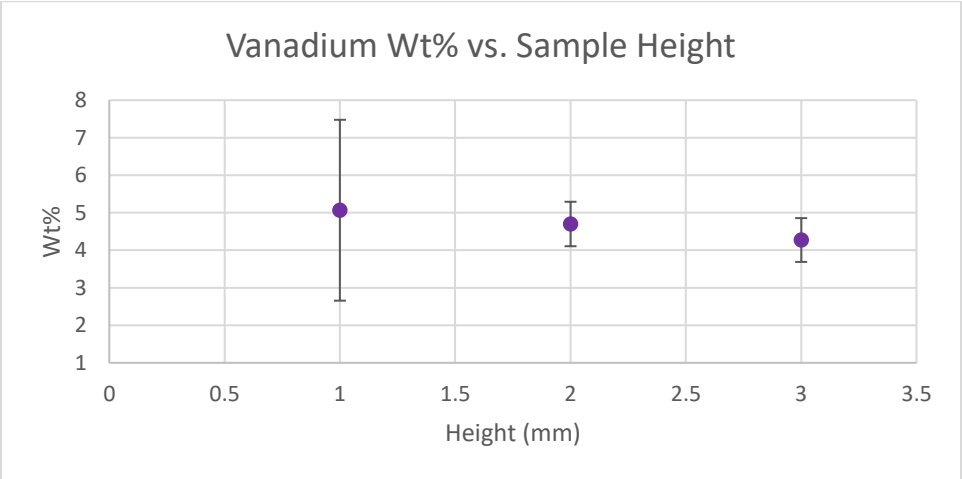

Figure 14. EDS Results for Vanadium Composition

2.4 Discussion

2.4.1 Microstructure

Based on visual inspection, the substrate and the deposition had two distinct morphologies. For the deposition, faint columnar grains were observed running parallel to each other in the direction at which the part was built. A slight curvature in the columnar grains was observed near the substrate interface. When using the optical microscope, the columnar grains showed more distinct β phases, which spanned in the vertical direction with a slight curvature in shape. The morphology for the deposition can be seen in Figure 3. This macrostructure was characteristic of DED Ti-6Al-4V. Due to the heat extraction that takes place as the material is deposited on a substrate base, the microstructure tends to have elongated, columnar grains in the build direction. Thus, the heat flow can be concluded to travel in the direction of the build, indicating unidirectionality solidification. The growth of the grains also related to the previous layer built having a more sustained cooling rate than the next layer [25]. In addition, with columnar grains, the grain size in the direction perpendicular to the build direction tends to be smaller compared to the parallel direction [16]. This could relate to the anisotropic behavior in mechanical texture [16].

Within the columnar grains, noticeably finer and non-directional grains were present as the microstructure. These thinner grains can be considered as Widmanstätten or basketweave-like structures formed for the α and β phases, as well as an acicular α' phase. It has been proven that the formation of the Widmanstätten microstructure is dependent on the cooling rate [30]. For slow cooling rates, α platelets in colonies exist with prior β grain boundary α phase [22]. When faster cooling rates and higher β stabilizing elements exist,

a basketweave structure is more prominent [22]. This correlates with the DED process and what was seen through the microstructure. In addition, it has been reported that for the microstructure of DED Ti-6Al-4V, finer Widmanstätten structures usually exist at the top and bottom of the part [16]. This phenomenon is related to the top and bottom regions of the deposition having relatively higher cooling rates, thus having finer microstructure, and resulting in a greater hardness [16]. However, conflicting microstructural features were observed in other studies. For instance, several studies examined that the top of the deposited layer was finer compared to the bottom, while others claimed the bottom layer was finer than the top layers [31]. The top layer exhibiting a finer microstructure makes sense due to the lack of reheating it experiences compared to the prior layers [31].

When decreasing in cross-sectional height along the sample, the grains change due to the transition from the deposition to the substrate. At the interface of the wrought Ti-6Al-4V and the DED Ti-6Al-4V, a heat affected zone (HAZ) of approximately 700 μm was prominent, which is presented in Figure 8. A heat affected zone appears in the microstructure when two materials are joined together [32]. It is a common phenomenon in welded materials [32]. Thus, the HAZ or macro-HAZ was present where the substrate and additively manufactured part met. This also occurred due to the partial melting of the substrate [17]. Similarly, when titanium is heated, the grains within the fusion layers and HAZ have been found to have a correlation with the size and growth of the solidifying grains in the melt pool [25]. A similar effect was seen with the DED sample in question. In addition, the HAZ effect is common for DED Ti-6Al-4V and has been investigated by other researchers [17]. For example, a study compared the amount of HAZ based on varying laser power [17]. When comparing the images with this research, the amount of

HAZ present for the sample under question correlated better with the high-powered laser condition, which exhibited a 500 μm thick zone [17]. Also, there could be slightly smaller regions of HAZ in DED Ti-6Al-4V, termed micro-HAZ or layer bands, which can occur between the deposited layers themselves [17]. However, this phenomenon was not observed on the DED sample in question. This could be due to differing process parameters and build dimensions.

As for the substrate, the microstructure showed possible equiaxed α grains, which was anticipated. In addition, it was seen that the amount of the α phase was seemingly larger compared to the β phase. This makes sense because when mill-annealing, it tends to deform the material by breaking up the α plates [4]. The deformation leads to recrystallization of the α phase, resulting in an equiaxed structure [4]. However, the resulting microstructure depends on the annealing temperature and the cooling rate [4]. Similar occurrences to this microstructure were documented for the cross-section of wrought Ti-6Al-4V by other researchers, in which the material was annealed and then rolled [33, 34]. The grain size was also determined in the mentioned study, which was found to be approximately 3 to 5 microns [34]. Furthermore, it was claimed that the titanium alloy was rolled or heat treated at a relatively low temperature in the α + β field (700°C) and the β transus temperature was 995°C [34]. This temperature is slightly higher than the average β transus temperature for Ti-6Al-4V. This knowledge was useful due to the unknown processing history of this study's substrate.

Another feature that was observed on the deposited layers was the porosity. Sporadic pores existed in the deposition, however, there shape was not constant. As seen in previous studies, pores can exist as sharp-edged defects as well as near circular voids

[27]. These features, especially for AM parts, are usually present due to unmelted material or nonuniform powder distribution [27]. Depending on the extent of the pores, it could greatly affect the mechanical properties due to the increase stress that would be concentrated near the holes [27]. Another paper concluded that there are two different types of pores for the DED process, which were termed interlayer and intralayer porosity [35]. Interlayer porosity happens due to the lack of fusion at the interface of each solidified powder layer and the discrepancy in the temperature distribution of the melt pool [35]. Intralayer porosity is related to gas being trapped in the material due to the vaporization at the melt pool [35]. It is believed that the interlayer porosity and solidification rate leads to anisotropic strength in relation to the build direction [35]. Further analysis was performed in the mentioned study and it was seen that for areas with a larger solidification cooling rate, the pores were shaped larger and more irregular [35]. For this study, however, the specific cause of the pores in the DED Ti-6Al-4V sample is difficult to determine.

2.4.2 Image Analysis

Sections of the microstructural features based on the height of the sample were examined for their α and β phase ratios. Previous papers have accomplished the determination of phases by counting the number of black (β) and white (α) pixels in a representative image to determine the ratio. For example, a report published by the company, Clemex, who regularly performs similar image analyses, utilized the pixel intensity method to measure the amount of α grains and transformed β grains, as well as the size of the α grains in standard Ti-6Al-4V [36]. Their α area percentages for the transversal and longitudinal samples were 72.90% and 72.71%, respectively [36]. Another phase analysis was done on a heat-treated AM Ti-6Al-4V [37]. The alpha percentage for

this sample was determined to be about 90.08%, which makes sense due the material being heat treated and increasing the α phase [37]. However, to the best of the author's knowledge, this technique had not been conducted on as-built DED Ti-6Al-4V specimens. It is also a widespread practice to use this pixel intensity method for determining the density of the part; thus, allowing the comparison between pores and the flat surface [27]. When determining density through this method, it introduces error due to only examining an area perspective [27]. Similarly, when calculating the phases using pixel intensity based on an area perspective, the surface or part is assumed to be fully dense. Another possibility for error is when the microstructural features are converted to a binary image. However, adjustments in coloring and contrast can be made to the picture to best represent the morphology.

When comparing the height along the cross-section to the α ratio, it was noticed that the α fraction ranged from 0.69 to 0.76 (Figure 10). When starting at the interface of the deposition and substrate, the α fraction appeared to be at the lowest amount. As the height into the deposition increased to the middle layers, the α fraction reached a maximum value of 0.76. However, at the highest part of the deposition, the α phase decreased slightly. Overall, the variation seemed to be small throughout the entire cross-sectional surface of the deposition. The α and β ratios were expected to vary throughout the microstructure due to the reheating and cooling of the deposition. This inherently would affect the mechanical properties when considering that the β phase is more ductile, while the α phase is stronger [22]. However, the effect or variation in the phases might not have been noticeable in the observed DED Ti-6Al-4V sample due to the sample height and deposited layer being only a few millimeters. As previously mentioned, other researchers have reported higher cooling

rates at the top and bottom of the deposited layer, leading to a finer microstructure and a greater hardness [16]. If it is assumed that the greater hardness at the top and bottom layers of the deposition is related to a greater amount of the α phase, that trend was nonexistent in the image analysis. In fact, it can be perceived that the middle layers of the deposition were harder than the edges of the deposition due to the slight variation in the phase ratio. This occurrence could deviate from what was anticipated due to the combination of processing parameters used, the deposition height chosen, or the inaccuracies induced when the microscope image was converted to a binary image.

2.4.3 Compositional Analysis

Using the data from the EDS of the DED Ti-6Al-4V sample, the weight percentages of each element based on the substrate, the interface, and the deposition were compared (Figure 12 through Figure 14). For the substrate composition, there appeared to be the greatest amount of variation in the elements, especially for titanium and vanadium with a standard deviation of 1.88% and 2.41%, respectively. This relatively large standard deviation could be due to the test locations and larger grain size in the substrate. Similarly, it has been documented that the α and β phases in Ti-6Al4V have slightly different elemental concentration [38]. For example, in a study, the vanadium was seen to change from about 4 wt.% in the α phase to approximately 8.5 wt.% in the β phase of a Ti-6Al-4V sample [38]. The location of the EDS tests in the current compositional analysis did not distinguish between phases, thus the results would have a larger standard deviation.

The composition of aluminum was consistently around 5.28% in weight for the substrate, the interface, and the deposition. In addition, the calculated aluminum weight percentage was slightly lower than the anticipated amount of 6%. Due to the minor

deficiency in aluminum, the vanadium was enhanced slightly in the composition to be larger than 4% in weight for each height along the cross-section. When referencing the chemical specification from Arcam EBM system, the titanium alloying elements are required to be within the ranges listed in Table 3 [39]. It can be observed that the compositions for aluminum based on each height were not within the required range by approximately 0.3 wt.%. Similarly, vanadium's weight percentage is slightly out of range for the interface (B) and substrate (C) heights by 0.2% and 0.5%, respectively. However, it has been reported that for standard Ti-6Al-4V plates, the composition can vary in a similar way (i.e. the aluminum weight percentage has been seen to be less than 5.5%) [40]. Thus, the composition for aluminum may be acceptable.

Table 3. Ti-6Al-4V Composition Standards

Element	**Arcam Ti6Al4V**	**ASTM F1108 (cast material)**	**ASTM F1472 (wrought material)**
Aluminum, Al (wt.%)	6	5.5-6.75	5.5-6.75
Vanadium, V (wt.%)	4	3.5-4.5	3.5-4.5
Carbon, C (wt.%)	0.03	<0.1	<0.08
Iron, Fe (wt.%)	0.1	<0.3	<0.3
Oxygen, O (wt.%)	0.15	<0.2	<0.2
Nitrogen, N (wt.%)	0.01	<0.05	<0.05
Hydrogen, H (wt.%)	0.003	<0.015	<0.015
Titanium, Ti (wt.%)	Balance	Balance	Balance

Traditionally, the shortage of aluminum and the enhancement of vanadium could affect the α and β stabilizing behavior, respectively, which would alter the β transus temperature (980°C). It has been reported that the more weakly stabilized the β phase is, a greater fraction of the α phase can precipitate [22]. This greater amount of α would increase

the strength that could be achieved [22]. However, it is the α phase that is relatively less stabilized in this case. This could lead to the sample having a greater fraction of β phase than expected. When considering that the deficiency in elemental composition is about 0.5%, the effects through the α and β phases may not be seen.

When strictly examining the average composition of each element for each height, the average amount of titanium increased by about 1% and the vanadium decreased about 1% in weight when traveling from the substrate to the deposition. This difference in elemental composition may be negligible. From a relative standpoint, a decrease in vanadium would indicate that there is less of a stabilizing ability from the β phase, which could relate to having more α phase. Since vanadium was already abundant, the decrease may not differ from traditional Ti-6Al-4V. However, a decrease in vanadium has been reported when using additive manufacturing processes on Ti-6Al-4V [41]. For example, a study was performed in which researchers weighed and combined the powder mixture of 90 wt.% titanium, 6 wt.% aluminum, and 4 wt.% vanadium [41]. Using direct energy deposition, the material was built on a Ti-6Al-4V substrate [41]. The composition along the build height direction was analyzed through area and line scans, in which the testing area consisted of 0.3 mm of substrate and 2.1 mm of deposition [41]. It was seen that a continuous decrease existed in the weight percentages of aluminum and vanadium, and the amount of titanium increased accordingly [41]. Based on the total distance tested, a decrease of 1.5 wt.% of aluminum and 2 wt.% of vanadium existed [41]. This decrease was claimed to be due to the different particle sizes and densities of the materials, which would result in the powder not being evenly distributed in the melt pool [41]. The researchers suggested implementing a multiple coaxial powder nozzle to evenly distribute the element

powder into the melt pool [41]. This incidence could possibly be what happened in the DED Ti-6Al-4V sample tested in this study.

Based on the image analysis conducted in relation to the compositional analysis, both had slight deviations when increasing in height from the interface to the deposition. As mentioned, the differences are not large, therefore, they could be negligible. When considering a general decrease in vanadium, more α phase has the potential to exist. Based on the image analysis, from the interface to the deposition, more α phase was present. Theoretically, this correlation is logical. However, a deficiency was present in aluminum, therefore, relatively less α could exist. Thus, it is difficult to state a firm conclusion on this correlation.

2.5 Conclusion

Common properties of DED Ti-6Al-4V parts includes columnar grains, fine Widmanstätten microstructure, and a HAZ when a base plate is used. These features were seen in the DED sample under investigation, and they can be concluded to be due to the heat extraction from the substrate and the relatively higher cooling rates induced by the DED process. In addition, there existed minor pores, however, they were not noticeable along the layer thicknesses. This could indicate that under-melting and over-melting may not have been an issue in the depositing of the material in conjunction with the laser energy. The microstructure of the substrate, wrought Ti-6Al-4V, was also what was anticipated based on other publications. Thus, the overall microstructure was characteristic of DED Ti-6Al-4V.

As for the image analysis, it was seen that from the interface to the deposition, there was an increase in the α phase fraction. In addition, the greatest amount of α was

determined to be within the layers of deposition instead of the anticipated lower α phases. It was expected that due to the top layer of deposition experiencing less reheating than the layers below it, the microstructure would be greater and finer alpha phases. If this outcome is true, the deviation from what was anticipated could be due to the combination of processing parameters used or the deposition height chosen in relation to other studies. However, the results are only as good as the images captured. In this study, the microstructural images were cropped to achieve defined grains. In addition, when converting the image to a binary one, the different grains may not be the true shape and size. Thus, some error was introduced when performing the image analysis. In addition, the variation could also relate to the locations chosen. Therefore, observing a greater area may lead to a more accurate correlation.

Regarding the compositional analysis, the elemental concentration was deemed to be acceptable. The aluminum weight percentages were consistent for the three heights of the cross-section. Slight deviations in titanium and vanadium based on the locations were counterbalanced by each other. More specifically, the vanadium decreased by 1% from the interface of the substrate and deposition (B) to the top of the deposition (A). Thus, there may be a trend that should be examined more closely, especially due to the image analysis inferring that more of the α phase could exist at the deposition compared to the interface. This phenomenon would be an attribute of a weakly stabilized β phase. In addition, the deficiency in aluminum and vanadium could be due to the DED process and the distribution of the materials. However, in this investigation, three data points were taken in the center of the sample for each height. Utilizing additional data points and spanning a larger area

may have led to a more accurate conclusion about the DED Ti-6Al-4V properties. Overall, the qualities investigated proved to be what was expected for DED Ti-6Al-4V.

Chapter 3: Nanoindentation Based Mechanical Characterizations – Single Indentation Experiments

3.1 Introduction

3.1.1 Nanoindentation

Nanoindentation testing is the use of instrumented indentation to determine the mechanical behavior and properties of a material, such as hardness, elastic modulus, and yield strength [3,9]. This is done through analyzing the continuous relationship between the indenter load and displacement response of the material, which is shown through a load vs. depth plot. In depth-sensing indentation testing, a load cycle consists of a loading and an unloading portion achieved at a prescribed rate. Furthermore, the loading of the indenter has a combined elastic and plastic deformation material response. The transitional load from elastic and plastic deformation depends on the material's response to strain [42]. However, when the indenter is unloaded, only the elastic behavior is recovered. Indentation testing can be performed on various scales, depending on the size of the indenter and the area of interest. For smaller volumes of material and an interest in the localized properties on a micro-level, nanoindentation is ideal. Due to the small scale, common materials used include bulk solids, thin films, and coatings [3,9]. Furthermore, the process can be either load-controlled or depth-controlled; this means that either a maximum load or depth will be specified, and the corresponding depth or load will be determined based on the materials' response.

Another characteristic of nanoindentation is the calculation of the contact area and the residual impression from the indenter in the material being only microns in size. Based on the geometry of the indenter and the contact depth, the area can be mathematically

calculated without the use of imaging techniques. However, a concern that can arise is the material behavior around the indenter when in contact with the indenter. Depending on the material, phenomena such as pile-up and sink-in can occur, which results in deviation from the mathematically calculated contact area. The existence of pile-up is related to low work-hardening and low strain-hardening exponents, which also can affect the slippage or friction between the indenter and material [43]. Typically, with moderate material pile-up or sink-in, friction is less significant and can be negligible [43]. Another consideration when indenting is if time-dependent characteristics, such as creep, are present. Indentation testing can produce large stresses and induce time-dependent effects; for example, it is possible that when a constant load is maintained, the indenter will continue to penetrate [43]. At room temperature though, creep is commonly neglected [43].

Depending on the experimental investigation, different indenter types can be used. Indenters are categorized based on tip bluntness or sharpness. Commonly, blunt indenters refer to a spherical and a flat, circular top in geometry. With the spherical indenter, the changing strain during the indentation allows for the elastic and elastic-plastic behavior to be examined more closely [44]. This smooth transition of the behavior on the load verses depth plot is necessary when determining the yield strength of the material and can also be applied to wear or scratch testing. Sharp geometry includes conical, Vickers, and Berkovich indenters. These are made to induce plastic deformation at the initial point of contact and are useful in determining the indentation hardness and elastic modulus of the material. In addition, sharp indenters can also be applied to understanding the fracture strength due to their ability to establish cracks [44].

However, the indenter of interest was the Berkovich indenter. The Berkovich indenter is pyramidal in shape and has three sides. This indenter is more easily manufactured than the Vickers indenter, which is a four-sided pyramid, to meet at a single point [44]. The face angle for the Berkovich indenter is approximately 65.27°, which directly relates to the projected area-to-depth ratio of the Vickers indenter [44]. Typically, for a new indenter, the tip radius is about 50 to 100 nm in size, but it can be worn down to 200 nm [44]. The indenter tip is usually made from diamond due to its hard, but brittle nature. These properties also reduce the indenter's effect on the measured displacement [45]. The elastic modulus for diamond ranges from 800 GPa to 1200 GPa, with a Poisson's ratio of 0.07 [44]. Further characteristics of the Berkovich indenter can be seen in Table 4 [44]. These factors are used for calculating the hardness and elastic modulus. The intercept factor of 0.75 is commonly used for pyramidal indenters due to the better representation of experimental data than the theoretical value of 0.72 [44]. In addition, the geometry correction factor can vary from 1.02 to 1.08. One application of the geometry factor is to account for the difference between the pyramidal shape and an axis-symmetric cone when using various equations for analytical purposes [44].

Table 4. Berkovich Indenter Characteristics

Area, A_c	$3\sqrt{3}h_c tan^2\theta$
Semi-Angle/Face Angle, θ (°)	65.27
Effective Cone Angle, α (°)	70.3
Intercept Factor, ε	0.75
Geometry Correction Factor, β	1.034

3.1.2 Objective

Investigation into the structural integrity of AM parts has been an ongoing topic of interest. There are vast AM methods that still require a greater understanding on how the parts are affected and how they can be enhanced. One process of importance is the direct energy deposition (DED) method. This technique utilizes an energy source, such as a laser. A commonly used material with AM and DED specifically is the titanium alloy Ti-6Al-4V. This is due to the material's high strength and low density that can be utilized in industries such as in automobiles, aerospace, and biomedical fields. The combination of AM and Ti-6Al-4V has shown to enhance mechanical properties, however, understanding the effects on the processing parameters would better the AM process and the part reliability.

It has been noticed through experimentation that the nature of the DED process induces anisotropic behavior in the parts. This occurrence relates to the processing parameters and how they directly affect the porosity, microstructure, mechanical properties, and residual stresses. For example, one cause of the varying mechanical properties is due to the temperature gradients exhibited by the material when the part is being built. The large temperature distribution therefore creates residual stresses in the parts. If factors such as residual stresses could be analyzed, it would benefit the AM process and parts.

In order to further understand the DED Ti-6Al-4V parts, quantifying the anisotropic behavior through nanoindentation and examining the effects of the residual stresses present are ideal. Therefore, the cross-section of the additively manufactured part was investigated. More specifically, when performing standard nanoindentation tests, the variation in load

verses depth curve, maximum penetration depth, final depth, hardness, and elastic modulus were analyzed based on the distance from the bottom of the substrate.

3.2 Method

3.2.1 Nanoindentation

When performing a nanoindentation test, the quantities tracked include the load of the indenter, the displacement of the indenter in the material, and time required for the loading and unloading process. By analyzing the load vs. depth graph, indentation hardness and elastic modulus can be calculated. This method was further developed by Oliver and Pharr through modifying Doerner and Nix's work on flat punch indenters [45,46]. One of the differences between the two methods is that Doerner and Nix concluded the initial unloading curve acted linearly [45,46]. This was due to the constant contact area that was achieved by using a flat punch indenter [45,46]. Oliver and Pharr concluded that when using a Berkovich indenter (70.3°), which can be modeled like a conical indenter, the unloading curve will have a slight curve [45,46]. Experimental data has shown that the curve can be best approximated by a power law function [45,46]. This has become standard practice, which is defined under ASTM E2546 (ISO 14577) [46,47]. An assumption required for modeling the Berkovich behavior as a conical indenter is that the area of contact sinks in, and that the indentations can be described as rigid punches of a simple geometry into a flat elastic half-space [46]. However, these assumptions do not account for the possible pile-up of the material on the indenter.

Quantities necessary for the calculation of hardness and elastic modulus can be extracted from the load vs. depth curve. These values include the maximum load of the test (P_{max}), the corresponding maximum depth (h_{max}), the final depth achieved after the indenter

was unloaded (h_f), and the initial unloading slope (S), which can be seen in Figure 15 and Figure 16 [46]. The initial unloading slope is utilized due to its more accurate representation of the elastic behavior of the material.

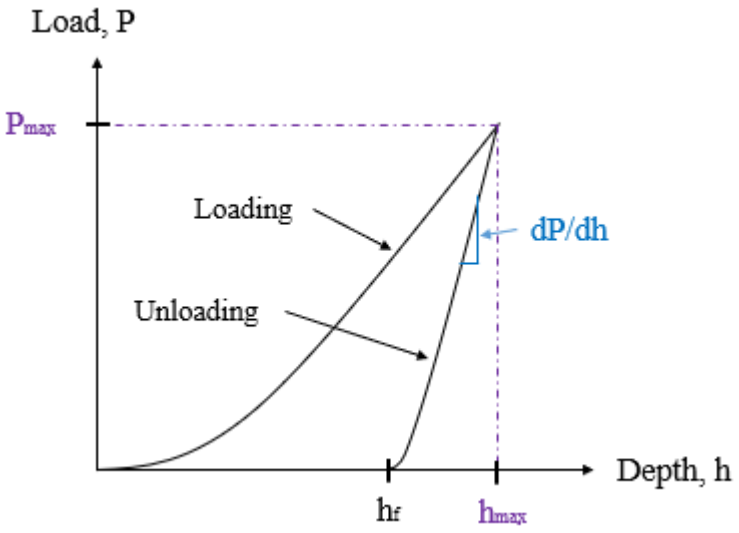

Figure 15. Load vs. Depth Curve

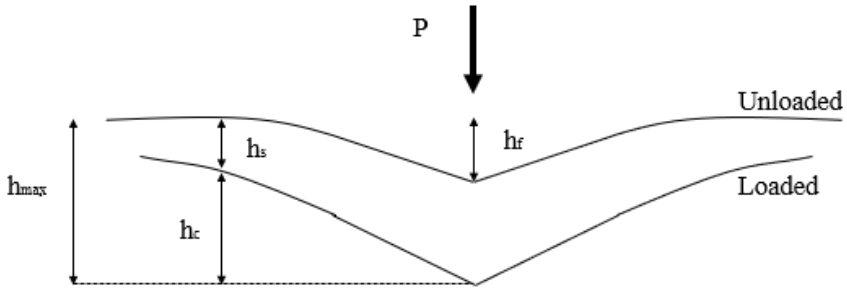

Figure 16. Indentation Impression

For the initial unloading slope, the power law relation can be utilized by taking the derivative of the trendline and evaluating the equation at the maximum depth value, which can be seen through equation 1 to 3.

$$P = K(h - h_f)^m \quad (1)$$

$$S = \frac{dP}{dh} = Km(h - h_f)^{m-1} \quad (2)$$

$$S(h_{max}) = \left.\frac{dP}{dh}\right|_{h_{max}} = Km(h_{max} - h_f)^{m-1} \quad (3)$$

To calculate the contact area (h_c), the sink-in depth (h_s) and the maximum depth are used. The sink-in depth is defined as a relation between the maximum load, contact stiffness, and the intercept factor for a Berkovich indenter. Once the contact area is determined, the projected area of the indenter (A_c) can be calculated, followed by the indentation hardness (H) or mean pressure that a material can withstand under a particular load. For an ideal Berkovich indenter, the area can be approximated as equation 6, however, an area function specific to the indenter in use was determined for more accurate material properties.

$$h_s = \frac{\varepsilon P_{max}}{S} \quad (4)$$

$$h_c = h_{max} - h_s = h_{max} - \frac{\varepsilon P_{max}}{S} \quad (5)$$

$$A_c = f(h_c) = 24.5{h_c}^2 \quad (6)$$

$$H = \frac{P_{max}}{A_c} \quad (7)$$

Furthermore, by using the axisymmetric indenter relation, as well as accounting for the elastic displacements between the indenter and the sample material, equation 8 and equation 9 can be utilized to find the indentation elastic modulus (E). The contact stiffness equation was developed by Sneddon and it was based on the relationship of an elastic half space being indented by any indenter that is considered to be a solid revolution of a smooth function [45]. As for the geometry factor, it was assumed to be unity for ease of calculations, however, deviations in the value have been seen by other researchers through

the use of finite element modeling [45]. Further analysis would be ideal to further understand the geometry factor applications.

$$\mathrm{S} = \beta \frac{2}{\sqrt{\pi}} E^* \sqrt{A} \quad \Rightarrow \quad E^* = \frac{S\sqrt{\pi}}{2\beta\sqrt{A}} \tag{8}$$

$$\frac{1}{E^*} = \frac{1-\nu^2}{E} + \frac{1-\nu_i{}^2}{E_i} \quad \Rightarrow \quad \mathrm{E} = (1-\nu^2)\left(\frac{1}{E^*} - \frac{1-\nu_i{}^2}{E_i}\right)^{-1} \tag{9}$$

3.2.2 Curve Fitting

The loading and unloading curve behavior as a power law has been previously studied. Depending on the type of material, the exponent tends to vary. It is believed that the power law is more suitable when experimenting on work-hardened layers due to the deformation response and the friction between the indenter and the sample surface [10,48,49]. Another reason could be related to the material not being ideally homogeneous [10,48,49]. A common characteristic for the loading curve is that it behaves quadratically (exponent of 2) [46]. However, other experimental studies have shown a slight deviation, which can be seen in Table 5 [10,48-50]. The loading curve exponent of 1.5 also has appeared as a possible behavior of material. Thus, the discrepancy between a universal loading exponent requires further investigation. As for the unloading curve, exponents for medium elastic recovery materials tend to be within 1.2 and 1.6 and are dependent on the indenter geometry [42,46]. A variety of the exponential unloading determinations can be seen in Table 6 [46,51].

Table 5. Loading Curve Characteristics

Material	K (mN/nm^m)	m	Quality, R	Reference
Polycarbonate	-	2.01	0.999	[50]
Sapphire	-	1.97	0.999	[50]
Fused Silica	-	1.94	0.999	[50]
Nanocrystalline Nickel	-	1.92	0.999	[50]
Ultrafine-grained Aluminum	-	1.88	0.999	[50]
Coarse-grained Aluminum	-	1.88	0.999	[50]
API X65 Steel	0.156	1.781	-	[48]
SS400 Steel	0.1473	1.6994	-	[10]
Tungsten	2.98	1.45	-	[49]

Table 6. Unloading Curve Characteristics

Material	K (mN/nm^m)	m	Quality, R	Elastic Modulus (GPa) [14]	Reference
Fused Silica	0.05 -	1.25 1.26	0.999997 -	72	[46] [51]
Soda-Lime Glass	0.0279	1.37	0.999997	72	[46]
Aluminum	0.265	1.38	0.999938	69	[46]
Silica	0.0215	1.43	0.999985	-	[46]
Sapphire	0.0435 -	1.47 1.66	0.999998 -	435	[46] [51]
Tungsten	0.141	1.51	0.999986	400	[46]
Nanocrystalline Nickel	-	1.63	-	-	[51]
Ultrafine-grained Aluminum	-	1.86	-	-	[51]

3.2.3 Area Function

To account for the worn Berkovich indenter, a compliance analysis and a calibration of the indenter shape was performed with the NANOVEA indenter and mechanical tester. For both procedures, fused silica provided by NANOVEA was used as a standard reference material due to its ideal material characteristics, such as a low elastic modulus to hardness ratio [53]. Further properties for a reference material include a uniform composition, isotropic elastic properties, and negligible material pile-up when indented, based on ASTM E 2546-07 [54]. The compliance analysis required a standard calibration test to be run on the fused silica sample with the Berkovich indenter. Multiple tests were used to optimize the machine's compliance and depth values. The results for the compliance analysis can be seen in Table 7. This analysis confirmed to be accurate due to the hardness and elastic modulus values being similar to published results [53,55]. The calibration of the indenter shape was then performed to account for the deviation of the ideal shape based on the single indent method. Various indentation tests were performed. The known material properties of the fused silica in conjunction with the indentation depth were utilized to graph the ratio of experimental to ideal area as a function of depth. A seventh-degree polynomial was fitted to the data to find the area correction equation. The result can be seen as equation 10, where the depth is defined to be in nanometers. For Berkovich indenters, it is standard practice to set the first coefficient to approximately 24.5 due to the ideal area being represented as $24.5h^2$ [2,45,54]. The remaining coefficients are the deviation from the ideal area. The deviation of the areas can be seen graphically in Figure 17 (graph to find curve fit equation) and Figure 18 (comparison of ideal and actual

areas). The determined area equation was used when analyzing the load and displacements graphs for all the indentation tests.

Table 7. Compliance Analysis for Nanovea Nanoindenter

Compliance	0.829
Depth (µm)	5.096
Hardness (GPa)	9.451
Elastic Modulus (GPa)	73.009

$$A(h_c) = 24.49{h_c}^2 - 29174.2047532333h_c + 5445531.07839892h_c^{\frac{1}{2}} - 123460508.762429h_c^{\frac{1}{4}} + 738450724.451231h_c^{\frac{1}{8}} - 1441924856.71432h_c^{\frac{1}{16}} + 821714956.316831h_c^{\frac{1}{32}} \quad (10)$$

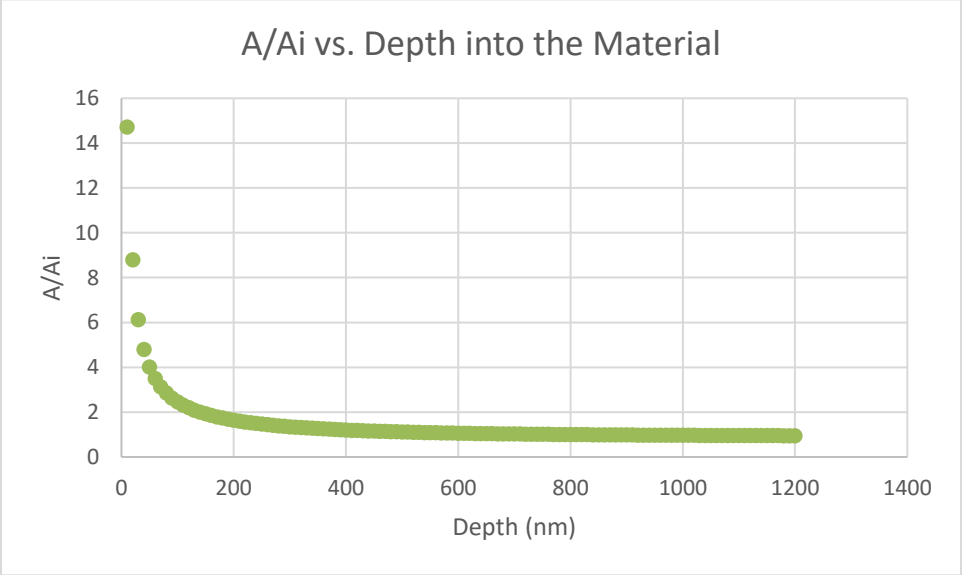

Figure 17. A/Ai vs. Depth

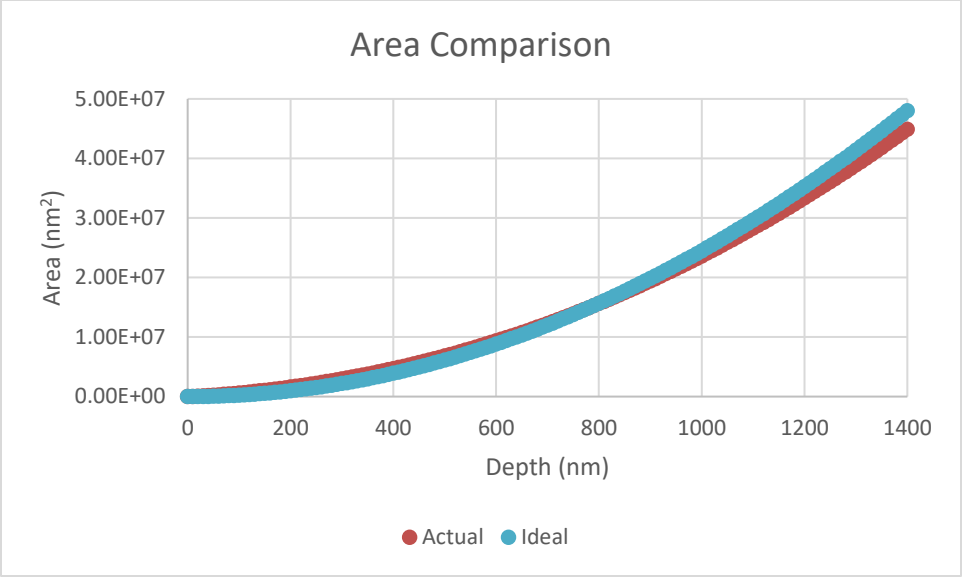

Figure 18. Area Comparison

3.3 Experimental Procedure

3.3.1 Sample Preparation

The DED Ti-6Al-4V sample was made using standard AM techniques. The initial temperature of the substrate plate was 25°C. The DED Ti-6Al-4V was deposited as a 2 mm layer on wrought Ti-6Al-4V substrate of 2 mm thickness. The scanning pattern was considered parallel and no dwells were utilized. The deposition spanned 13 mm by 15 mm on the substrate. The area of interest was the cross-sectional area; therefore, it was cut in the center (in the direction it was built up) to expose the cross-section. Using a diamond cut-off wheel in wet conditions (i.e. water) and a rotation of approximately 550 rpm, the final measurement of the sample was made to be 13 mm by 7.5 mm by 4 mm. For ease of handling, the sample was then mounted in bakelite to expose only the cross-section. The surface was mechanically polished at low speeds with progressing sizes of waterproof silicon carbide paper, ranging from 220 to 4000 grit. A mirror finish was then achieved

using colloidal silica polishing suspension. The sample surface was ultrasonically cleaned using acetone, methanol, and deionized water.

3.3.2 Test Parameters

Single nanoindentation tests were performed with a Berkovich indenter, which had a manufactured radius of 70 nm. The tests were conducted at room temperature using Nanovea's Mechanical Tester Machine equipped with a nano-module. The experimental setup can be seen in Figure 19. A 5 x 10 grid was utilized for the test spacing, which resulted in a horizontal distance of 1.18 mm and a vertical distance of 0.67 mm separating each test. The specimen and test locations can be seen in Figure 20. The software module was load-controlled; therefore, the specified maximum load was inputted as 150 mN, with a loading and unloading rate of 300 mN/min. Thus, one test was approximately a minute long. These parameters were in conjunction with the prescribed conditions recommended by the machine manufacturer.

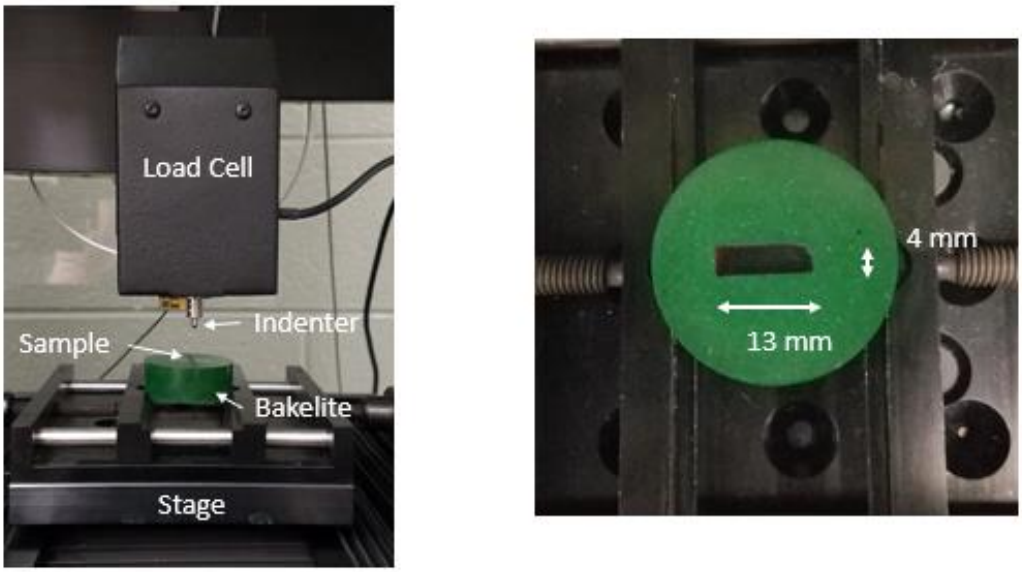

Figure 19. Experimental Setup

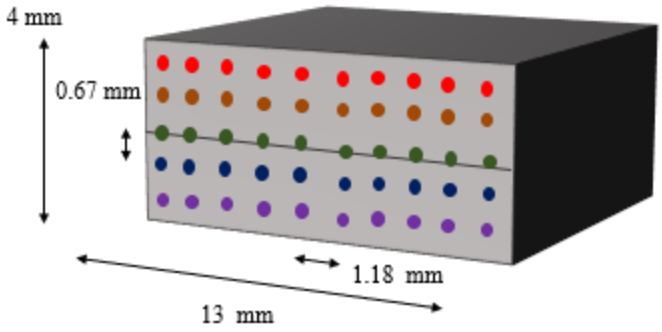

Figure 20. Single Indent Test Positions

3.4 Results

For calculations and analyses, it was assumed that the behavior of each row acted in a similar manner due to the DED process inducing a greater temperature gradient between each layer than within a layer. Therefore, the analysis was based on the variation of nanoindentation results with build height or distance from the bottom of the substrate. However, a depiction of the typical behavior within each row is presented in Figure 21. Figure 21 shows the experimental results for the first row, which is at 0.67 mm from the bottom of the sample.

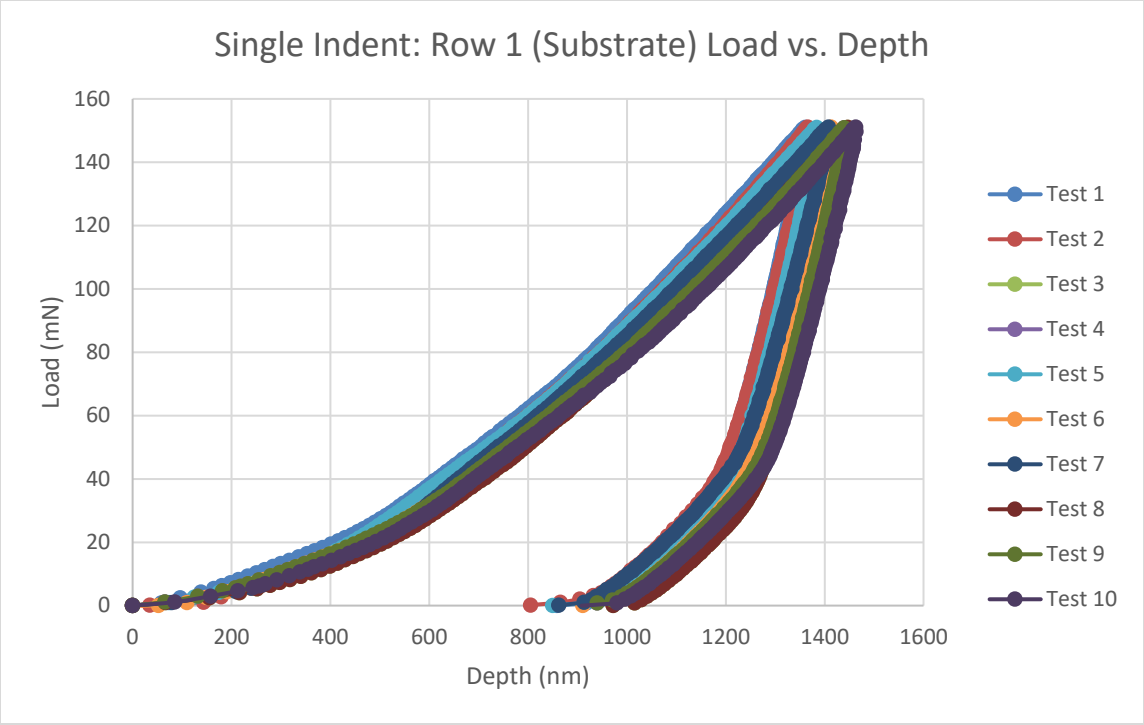

Figure 21. Single Indent: Row 1 (Substrate) Load vs. Depth

For comparison, the experimental loading curves based on the sample height can be seen in Figure 22. The experimental curves were aligned to begin at the zero depth and zero load measurements, which was based on the ASTM standard for nanoindentation. Similarly, the experimental unloading curve behaviors are presented in Figure 23.

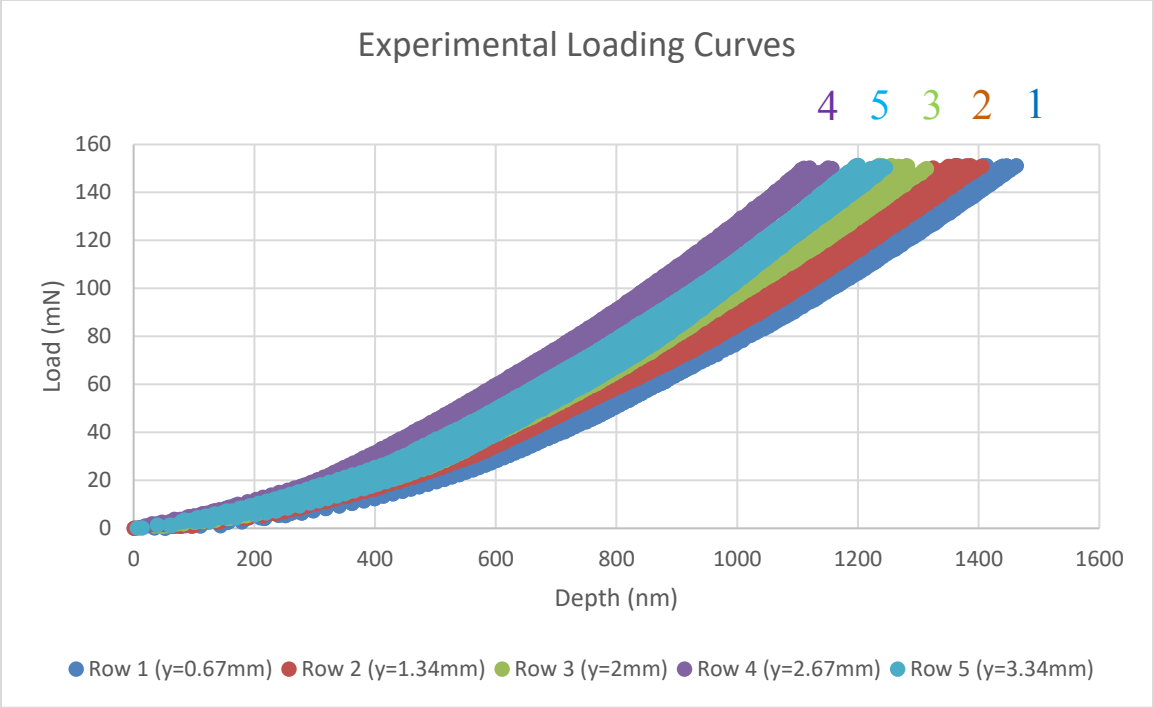

Figure 22. Experimental Loading Curves

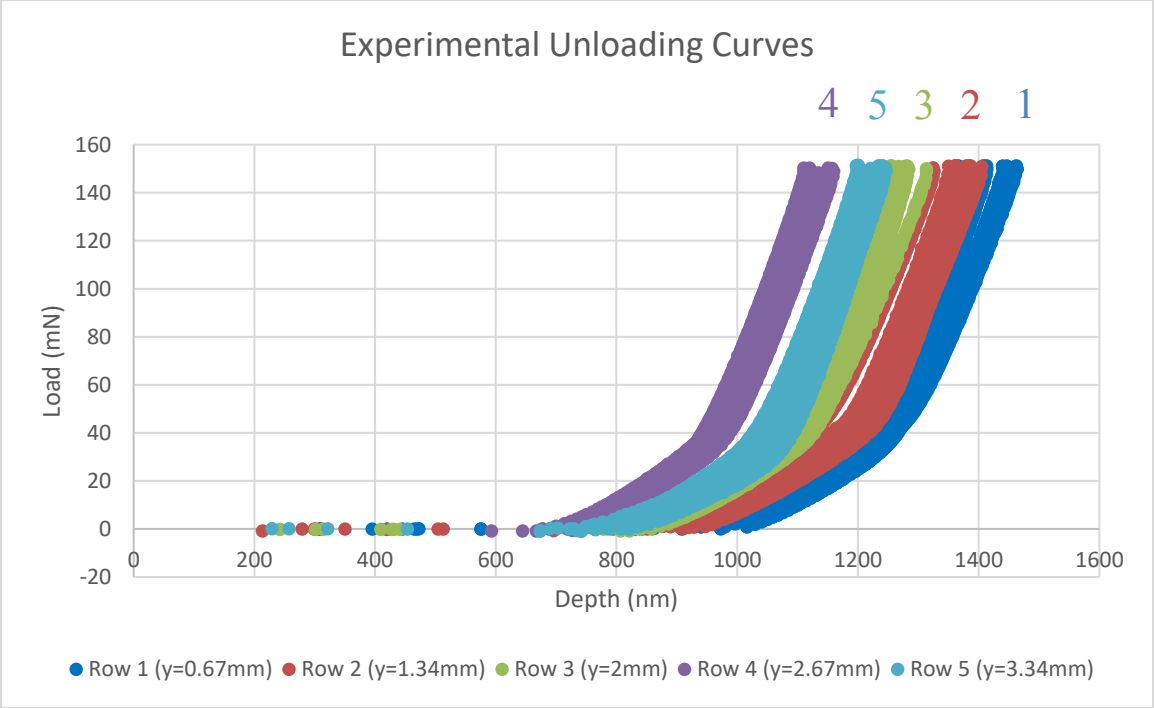

Figure 23. Experimental Unloading Curves

The experimental loading curves and unloading curves corresponding to each row were aligned based on ASTM E2546-07 and fit to one trendline utilizing the power law equation. For the loading curves, all of the data points for the particular row in question were applied to find the power law equation. A representation of finding the loading curve trendline in Excel is shown in Figure 24 for the data from row 1. To find the unloading curves' trendlines, the initial point of each unloading curve was aligned based on the average maximum height value to receive a better representation of the unloading curves. The shifting of the unloading curves to account for the final depth was taken into consideration as well. Another feature of the unloading curves was that for each experiment, there were two distinct behaviors. For the initial unloading nature, it acted close to a power law equation, however, when the load reached less than 60 mN, the curvature decreased more rapidly. Due to the elastic modulus analysis and theory being based on the initial unloading curve, the data points below 80 mN for all tests were excluded when determining the trendline for each row. The data used for the calculation of the unloading trendline for row 1 can be seen in Figure 25 and Figure 26.

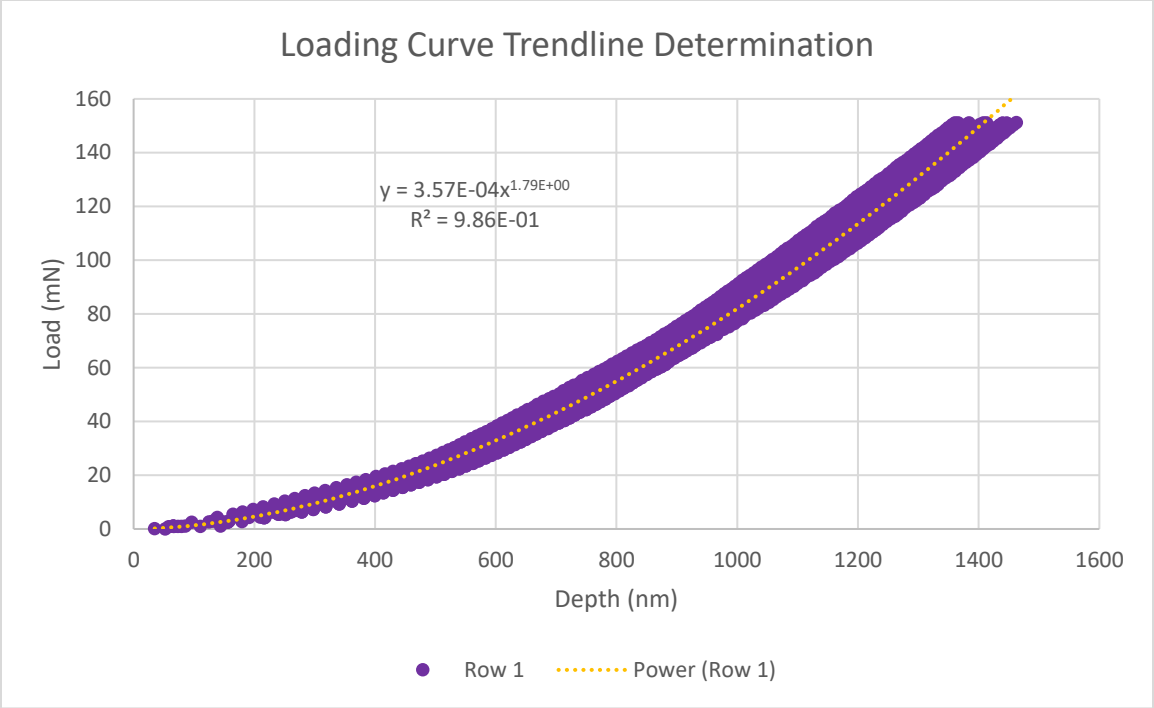

Figure 24. Loading Curve Trendline Determination for Row 1

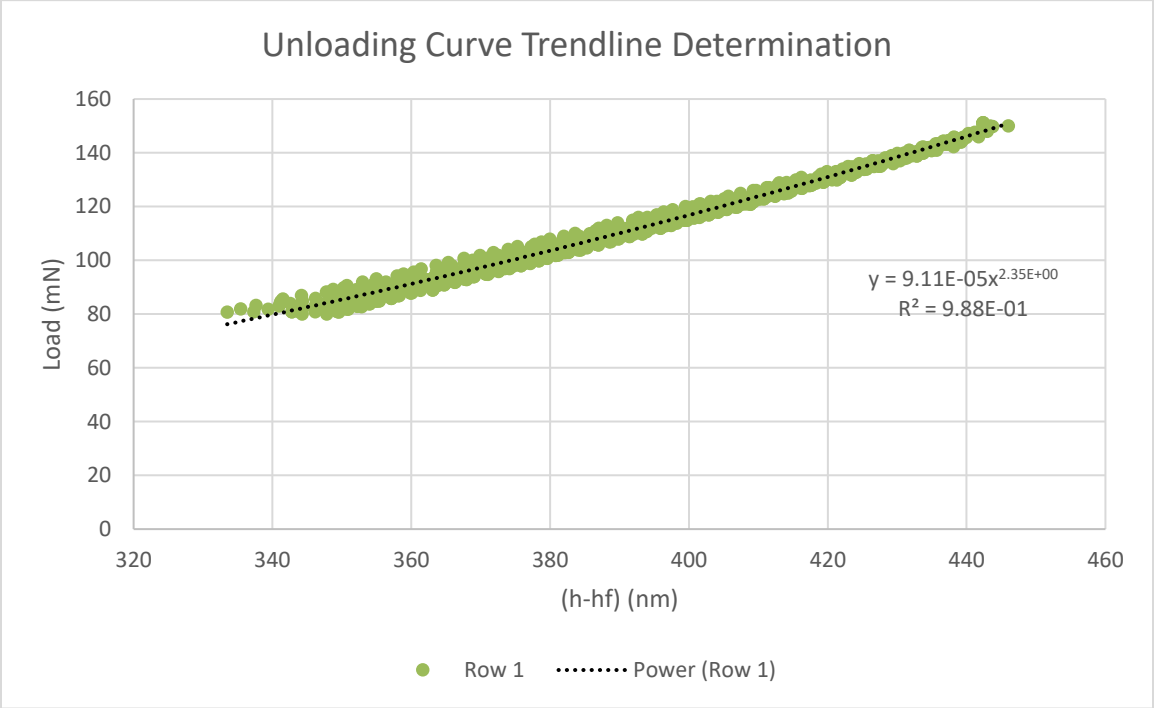

Figure 25. Unloading Curve Trendline Determination for Row 1

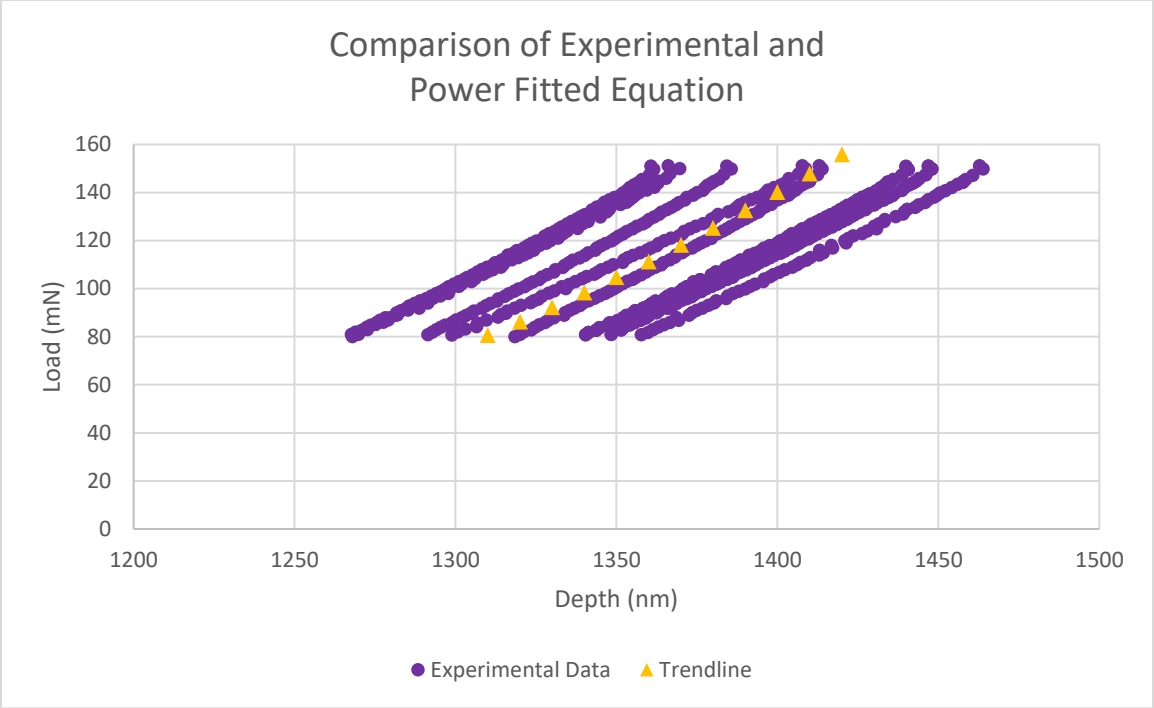

Figure 26. Comparison of Experimental and Power Fitted Equation for Row 1

The representative trendlines for the single indent experimental data can be seen in Figure 27, where the coefficient and exponent for the power law equation can be found in Table 8. Each experimental test was then analyzed to determine the maximum depth and final depth. The contact depth was calculated for each test as well. The depths presented in Table 9 are the average depths for each row.

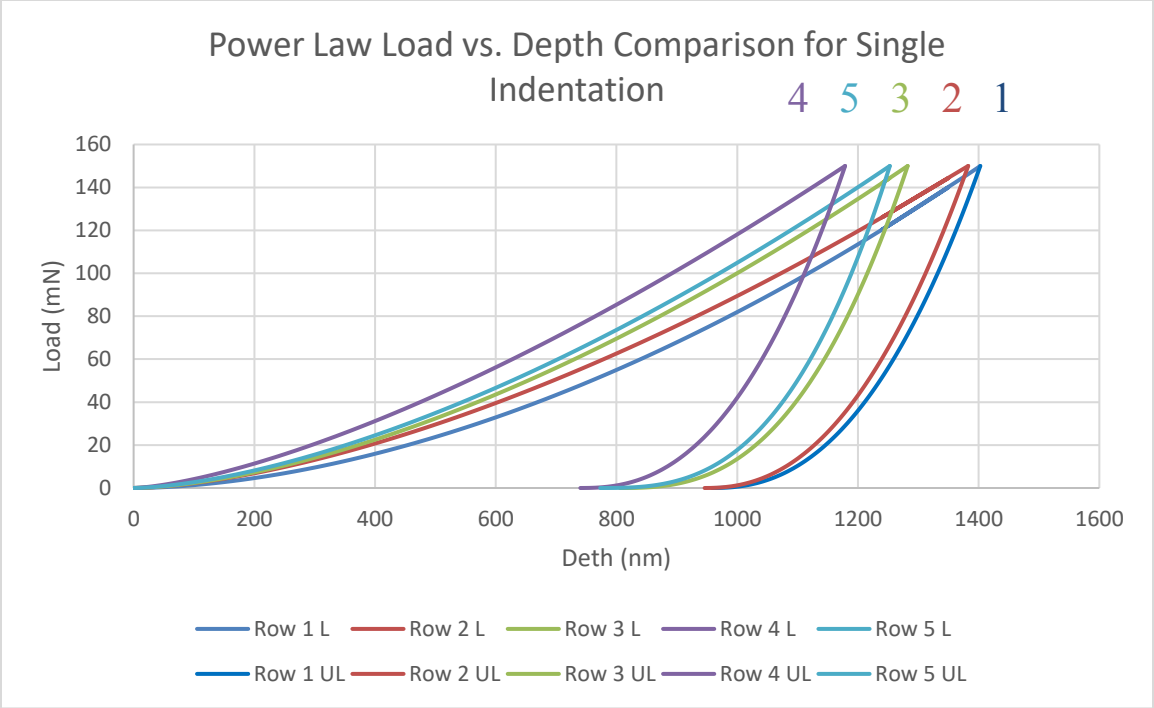

Figure 27. Power Law Load vs. Depth Comparison for Single Indentation

Table 8. Power Fitted Equation Comparison Based on Height for Single Indentation

Row	Height (mm)	Loading Coefficient, K_L (mN/nm^{m}_{L})	Loading Exponent, m_L	Unloading Coefficient, K_{UL} (mN/nm^{m}_{UL})	Unloading Exponent, m_{UL}
1	0.67	3.5733e-04	1.7868	9.1072e-05	2.0938
2	1.34	1.4550e-03	1.5962	1.2749e-04	2.2993
3	2	1.3031e-03	1.6284	9.7828e-06	2.6829
4	2.67	5.1386e-03	1.4538	5.6483e-05	2.4314
5	3.35	1.8276e-03	1.5863	3.3330e-06	2.8545

Table 9. Depth Comparison Based on Height for Single Indentation

Row	Height (mm)	Contact Depth (nm)		Maximum Depth (nm)		Final Depth (nm)		h_f/h_{max}
		h_c	SD	h_{max}	SD	h_f	SD	
1	0.67	1282.7	34.28	1416.81	36.33	947.806	47.89	0.669
2	1.34	1226.2	33.40	1359.01	35.40	891.27	39.27	0.656
3	2	1144.47	20.54	1267.38	22.63	838.765	25.11	0.662
4	2.67	1013.54	17.12	1137.80	15.84	694.408	17.48	0.610
5	3.35	1139.48	33.13	1255.92	33.40	805.426	45.80	0.641

As previously seen, due to the affects residual stress can have on both h_f and h_{max}, the ratio of the two depths would further display the nature of the material and the pile-up present. Based on each test within a row, the depth values were directly taken from the load vs. depth curve and averaged. The depiction of the ratio h_f/h_{max} with respect to the height of the sample is presented in Figure 28.

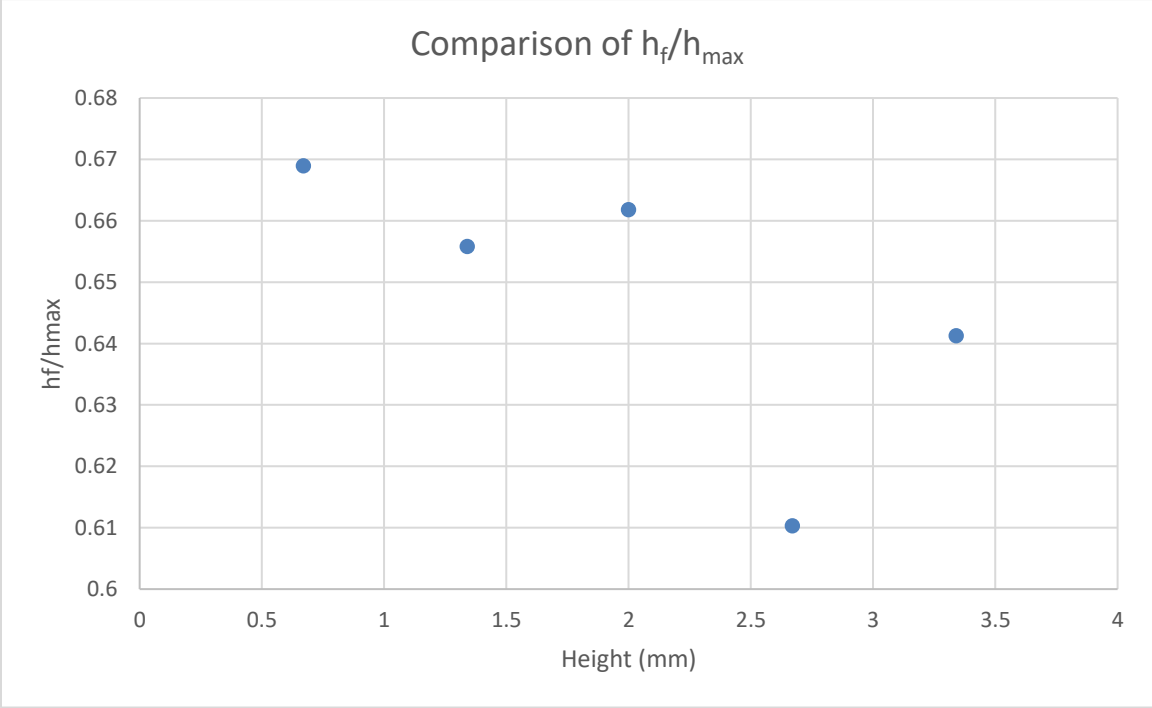

Figure 28. Comparison of h_f/h_{max} for Single Indentation Tests

For each vertical location (row) along the cross-section of the sample, ten hardness calculations were performed and then averaged. The representation of the averaged hardness values based on the build height from the substrate can be seen in Figure 29.

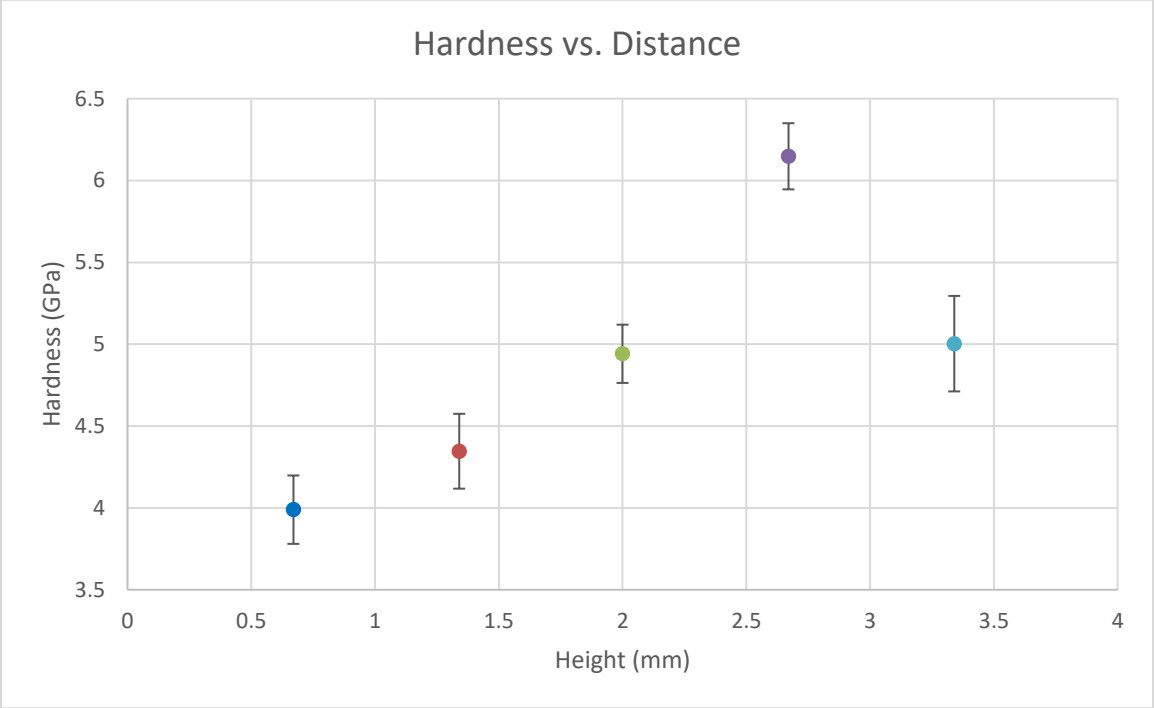

Figure 29. Hardness Comparison

Similar to the hardness calculations, an average elastic modulus was determined using the Oliver-Pharr method and compared based on height from the substrate. The variation of the elastic modulus along the cross-section can be seen in Figure 30.

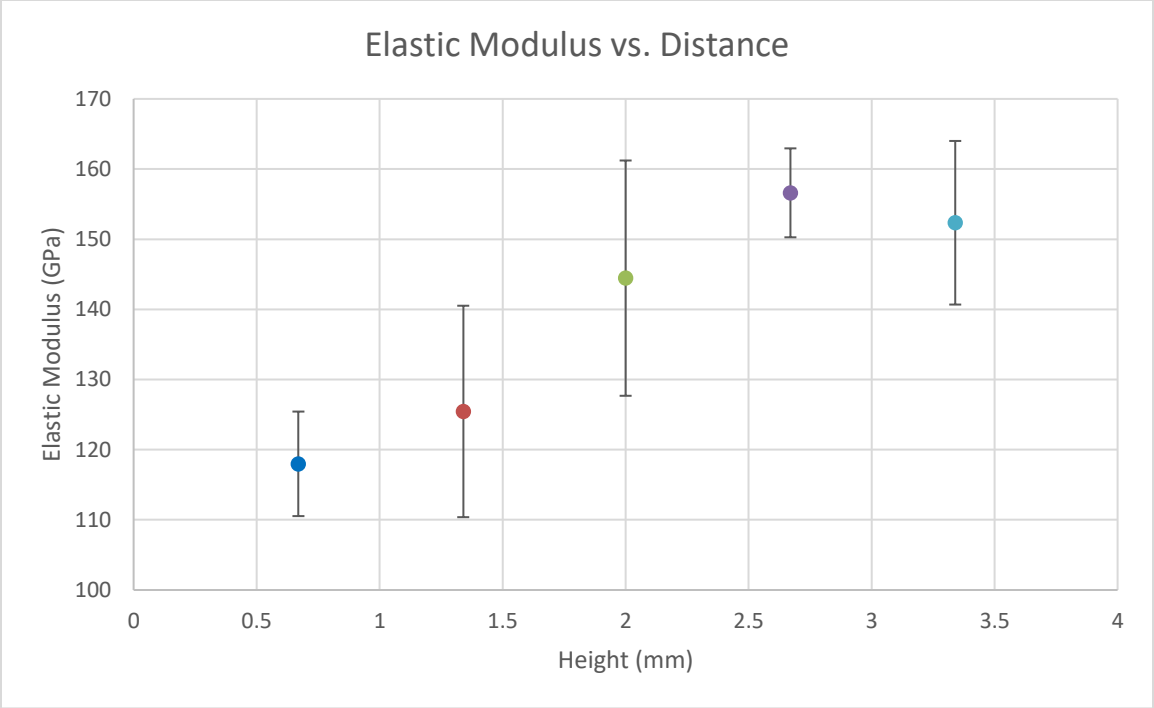

Figure 30. Elastic Modulus Comparison

3.5 Discussion

3.5.1 Load vs. Depth Curves

There were slight variations of the tests in each row. The deviance can be observed through the difference of the lowest and highest maximum depth value as well as the standard deviation of the maximum depth values. For instance, the largest maximum depth value difference was 125 nm, which was seen in row 2 (substrate). The largest standard deviation based on the maximum depth was 36 nm, which existed in row 1 (substrate). The smallest maximum depth value difference and standard deviation on h_{max} was 46 nm and 16 nm, respectively, which was for row 4 (deposition). Thus, similar behaviors were present for each row. Another phenomenon that should be recognized was that the substrate tests had the largest deviations compared to the deposition tests. This made sense due to

the larger grain size in the substrate. Typically, the more grains that the indenter straddles when indenting, the more accurate and consistent the results would be.

When looking at the experimental loading curves, a trend was noticed. As the height along the cross-section is increased (row is increased), the curvature of the loading curves became more inclined. The only discrepancy was between row 4 and row 5. Instead of row 5 becoming steeper, it took the behavior of row 3. However, each row appeared slightly to overlap each other. The behavior that was seen through the loading curve was in turn seen through the unloading curve. Furthermore, the pattern translated to the hardness and elastic modulus calculations.

When determining the loading curve trend line, all of the data was utilized. A comparison to find the best equation was accomplished based on the r-squared values. Typically, a quadratic equation had been used in others' research to depict the behavior of the loading curves. However, it was seen that the power law described the behavior more accurately. Thus, based on the experimental curves, the trendlines determined appeared to be a more accurate representation for the DED Ti-6Al-4V sample. In addition, the depth units used for the trendlines were in nanometers and the load units were in millinewtons. For the unloading curves, two distinct patterns existed. When the unloading initially happened, the power law seemed to fit accurately, but once the load was unloaded to approximately 60 mN, the depth changed more drastically. The second behavior could not be accurately explained through an equation. This could be due to the combination of the load being small and the decrease in amount of data points reported due to the unloading rate. The lack of points at the end of the unloading curve could have affected the determination of the final depth. However, the determination of the depth was carefully

examined for when the load reached a plateau and not necessarily the last point detected by the software.

For the trendlines, a similar behavior to the experimental data was seen. For the same load established, the penetration into the surface became less compared to the initial substrate row. One stipulation with the trend curves was that the unloading curve was only valid for loads ranging from 80 mN to 150 mN. Thus, the behavior below 80 mN did not accurately portray the experimental behavior. In turn, the theoretically determined final depth values could not be compared to the experimental values to check for validity. The maximum depth values (based on the experimental and trendline data) were compared instead to ensure an accurate representation of the trendline. It was seen that the values predicted by the equations were within the standard deviation of the maximum depth values for each row except for row 4. A slight overestimation in the value was seen by approximately 40 nm. However, the behavior between each maximum depth value was what existed experimentally and is presented in Figure 31.

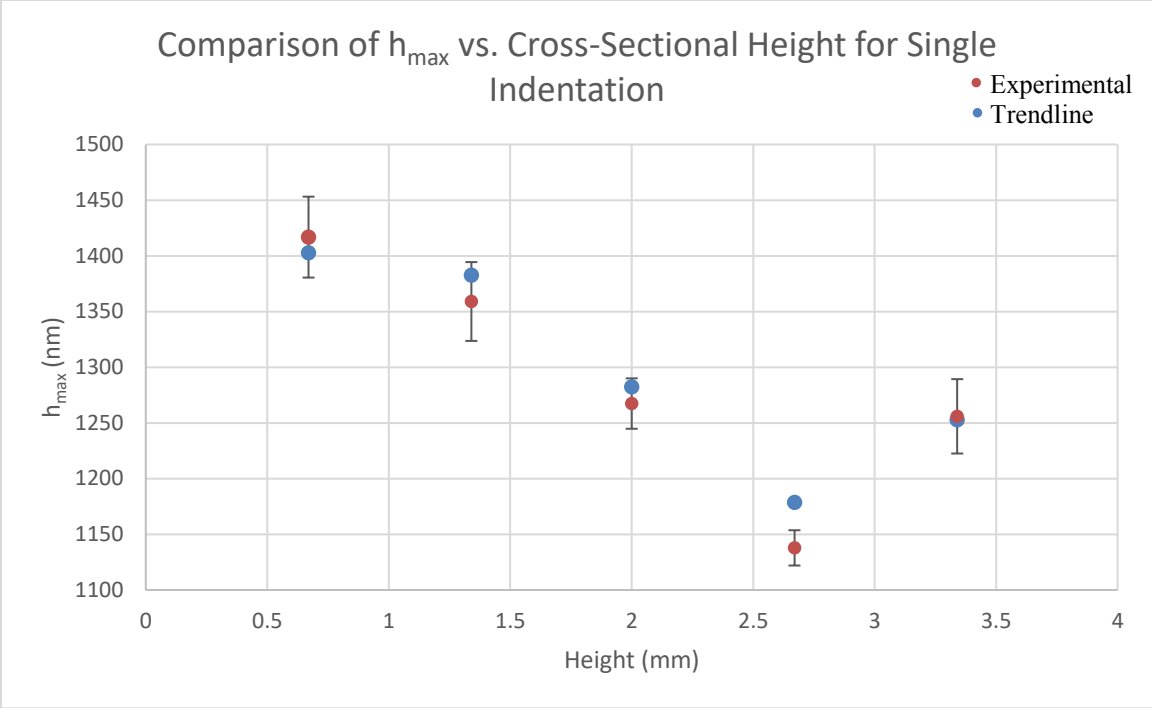

Figure 31. Comparison of Maximum Depth vs. Height for Single Indentation

Then, the exponents were compared for the loading and unloading curves to give a numerical comparison to the visual behavior that was seen. As for the loading exponents compared to the cross-sectional height, a decrease from 1.8 to 1.4 was present. It appeared that the substrate behavior was the closest to the quadratic relation other papers have used for the loading curves (i.e. exponent of 2). As the deposition was reached, other characteristics were involved, such as a change in microstructure and possible residual stresses, thus the material deviated from the bulk characteristics. As for the unloading exponent, there was a slight variation, however, an increasing trend was loosely seen. Typically, the elastic behavior should remain consistent for bulk materials. The DED Ti-6Al-4V is not considered bulk due to the documented variation and process induced features, thus the variation in stiffness made sense. The exponents ranged from 2.3 to 2.8. For Berkovich indenter, the exponent behavior is typically within 1.2 and 1.6, reported by Oliver [45,46]. This was not the case for the DED Ti-6Al-4V sample tests performed. The

closest previously documented unloading exponent found was 1.86 for an ultrafine-grained aluminum. Therefore, it appeared that a finer grained material would inflate these documented exponents. In addition, the materials considered for the 1.2 and 1.6 exponent did not have residual stresses present. The nanoindentation results would differ if a material had residual stresses.

3.5.2 Loading Characteristics

The maximum depth reached was for the first row (height of 0.67 mm) or the substrate at approximately 1416.81 nm. As the height of the sample increased to the interface, the maximum depth reached became distinctly lower. This behavior suggested that the indenter with the same load was penetrating the material less. Once the deposition was reached, the maximum depth continued to lessen, however, there was an increase for the fifth row, which is also in the deposition. This slight increase in the maximum depth suggested the material was easier to penetrate at the top than in the center of the deposited layers. This could be related to row 5's proximity to the free surface compared to row 4. Due to the mathematical relation between the maximum depth and the hardness (or the pressure), the hardness exhibited a similar trend. At the substrate, the hardness was about 4 GPa, which was expected for the hardness of wrought Ti-6Al-4V. As the height of the sample was increased to the deposition, the material became harder. The maximum average hardness calculated was approximately 6.25 GPa at the center of the deposition. At the row closest to the top of the deposition, there was a decrease in the hardness.

When comparing the substrate values with the deposition values, there was a noticeable increase in hardness. Other papers have documented similar findings regarding additive manufactured materials having differed material properties compared to their

wrought counterparts. For example, an experimental investigation by Jun Yu et al. was conducted on laser metal deposited Ti-6Al-4V (which was built on a Ti-6Al-4V substrate) to analyze the material hardness [56]. The test area was approximately 10 mm in height, where the bottom 5 mm was the substrate and the top 5 mm was the deposited layers [56]. The Vickers hardness was determined using a load of 1 kg (1 N) [56]. A total of 18 tests were conducted along the cross-section of the sample at different heights along the centerline [56]. In addition, 2 mm from the top of the deposited layer was not analyzed for hardness. The same test setup was conducted on 3 samples that only differed by the laser power: 380 W, 470 W, and 570 W [56]. The results for the LMD samples showed that there was a distinction between the substrate and deposition regarding the hardness [56]. For the Ti-6Al-4V substrate, the average hardness was approximately 340 HV (3.3 GPa) [56]. As the deposition was reached, the average hardness was determined to be about 360 HV (3.5 GPa) [56].

Another study performed by Lei Yan et al. was done using Vickers hardness to determine the material behavior along the cross-section of a direct laser deposited Ti-6Al-4V sample built on a wrought Ti-6Al-4V substrate [41]. Approximately 10 heights were chosen spanning through 1 mm of substrate and 3.3 mm of deposition [41]. In addition, different laser powers and scanning speeds were employed to further understand the material behavior [41]. It was determined that the hardness of the substrate for each case was relatively lower than the deposited layer [41]. The hardness at the substrate was approximately 325 HV (3.2 GPa), whereas the deposited layer for almost every case (except for the high-power setting of 750 W, which showed to be 525 HV or 5.1 GPa) was on average to be 450 HV (4.4 GPa) [41]. During the 3.3 mm span of the deposition, the

hardness value seemed to level out [41]. The results determined in both the studies deviate slightly in regard to the nanoindentation hardness calculated in this case. This could be due to the differing process parameters when manufacturing the part, the sample size, and the technique for calculating the hardness. For example, the two studies utilized Vickers hardness testers with a 1 kg load and performed only one test for each position on the cross-section. In addition, the Vickers indenter was as large as 50 microns, which covered a greater area compared to the Berkovich indenter used in the nanoindentation experiment. However, the increase in hardness was evident from the substrate to the deposition for all three experiments.

Characteristically, the hardness should remain constant for the same material. Even for the substrate alone, there was an increase in nanoindentation hardness for this case. This could be due to residual stresses and the thickness of the substrate. When the material is heated and solidified on the substrate, residual stresses are induced based on a thermal mismatch. A resultant from this phenomenon is called warping. Warping or distortion occurs in the material due to the residual stresses. A study investigated the influence of the substrate thickness [57]. It was concluded that when the substrate and deposition was increased from 2.56 mm to 12.7 mm and 0.76 mm to 2.56 mm, respectively, the distortion decreased [57]. In addition, for the thinner substrate layer, preheating the substrate also minimized the warping effects [57]. Less distortion means less residual stresses. For this nanoindentation study, the Ti-6Al-4V substrate was not preheated, thus, greater temperature gradients would occur, causing greater residual stresses at the interface. Therefore, the initial temperature of the substrate would also affect the nanoindentation results.

The residual stresses, depending if they are tensile or compressive, can change the nanoindentation hardness. This change is based on the idea that nanoindentation hardness varies from the true material hardness due to the calculation of the impression or indenter area. The sample material can pile-up around the indenter and the impression, which is not accounted for in the traditional Oliver-Pharr method. Therefore, the DED process on the substrate may have caused the material to be strained and become harder. Thus, a change in true area would occur when indented with the same amount of load.

In addition, the distance away from the interface into the substrate for testing would influence the hardness. It was possible that the thickness of the substrate was relatively small so that the average hardness at the bottom of the plate was still enhanced due to strain from the DED process. This occurrence can also be seen in the previously mentioned study done by Lei Yan et al [41]. Each position in a span of 0.9 mm calculated for hardness showed an increasing trend in the substrate [41]. However, when the substrate thickness was approximately 5 mm in the investigation done by Jun Yu et al., a steadier hardness value was determined [56]. Thus, a certain distance away from the interface is required to determine the true nanoindentation hardness of the substrate.

The previously mentioned reasons for the substrate variation assumed that the results were strictly accurate (i.e. increase in hardness of the substrate). There was a possibility that the variation in the substrate was due to the relatively larger grain size. The larger grain size would result in a larger deviation when nanoindenting. Even for the Vickers hardness tests done by Jun Yu et al., there was a large variation in the substrate compared to the deposition layer hardness (approximately 0.4 GPa difference in hardness based on 5 mm of substrate) [56]. However, the size in the Vickers indenter is unknown,

which makes it difficult for further comparison. Thus, the 0.5 GPa difference in this nanoindentation study may have been a result of the nanoindentation test positions and indenter size, and there may not exhibit a true increase.

When considering the heat affected zone (HAZ), it acted as a transition from the substrate to the deposition. The interface would be stronger than the substrate due to the heating from the DED process, but it also can be weaker than the deposition due to the joining of two materials. However, depending on the processing parameters, studies have mentioned that the bottom layer of the deposition may have a finer microstructure, while others have reported that occurrence in the top layer. However, the greatest hardness calculated in this case was within the deposition, not at the interface. As previously mentioned, the substrate characteristics would affect the apparent material properties. Due to the substrate not being preheated, the material properties determined using nanoindentation technique may have been altered. However, an increasing hardness trend was seen by Jun Yu et al. when transitioning from the substrate to the deposition [56]. For the lowest power setting of 380 W, the hardness measurement went from 320 HV (3.1 GPa) to 350 HV to 370 HV (3.7 GPa), showing an increasing trend [56]. In addition, for Lei Yan et al.'s case, when the interface was reached for laser power of 550 W and 650 W, an increasing trend in hardness was also seen through the interface of the sample [41]. However, when the power was increased to 750 W in the study, the interface was determined to be the same hardness as the deposition [41]. Thus, this showed the importance of the processing parameters.

As for the variation in the deposition, this may have been due to the DED process as well. It has been determined that the reheating and fast cooling rates would cause

residual stresses in additively manufactured materials. Many investigations have been done on the selective laser melting (SLM) and the direct metal laser sintering (DMLS) of materials in understanding the residual stresses that are induced. For example, X-ray diffraction and hole-drilling methods have been utilized to determine the residual stress behavior based on additively manufactured samples' height. It has been documented that the residual stresses have been higher than the yield strengths of their wrought counterparts [12]. However, the additive manufacturing process also can affect the microstructure. As previously mentioned, the thermal history directly relates to the microstructure. Continuous heating and solidifying can result in coarser grains. This phenomenon could explain why the first nanoindentation test in the deposition became harder, as similar papers have reported the "bottom" having finer grains. However, this phenomenon would not explain why the top of the deposition would decrease in hardness. It has been suggested that the top of the deposition would have the least amount of heat applied to it, thus having a finer microstructure than the middle of the deposition. The finer microstructure would insinuate an increase in hardness.

In the deposition of Jun Yu et al.'s analysis, a slight decrease in the hardness was noticed as it progressed in the deposition, like what was seen with the nanoindentation hardness [56]. Both occurrences could be due to the test locations in the deposition not being at the true "top" that other investigations have referred to (for having a finer microstructure). It is possible that the deposition thickness could relate to the hardening effect that was previously reported in the deposition layers. The use of different processing parameters would explain the conflicting investigations regarding the hardness variation.

Another possibility for outcome of the hardness results could be due to the technique used when nanoindenting. When performing the nanoindentation tests, they were approximately 1.18 mm horizontally apart for each row. After the tests were done, each impression was examined. It was noticed that six out of the ten tests were conducted within an α colony grain accidentally (Figure 32). Even though the indenter contacted multiple grain boundaries, it is possible that more of the α phase was present. Therefore, since the α phase is typically harder, the results may have showed an abnormal amount of α phase accidentally.

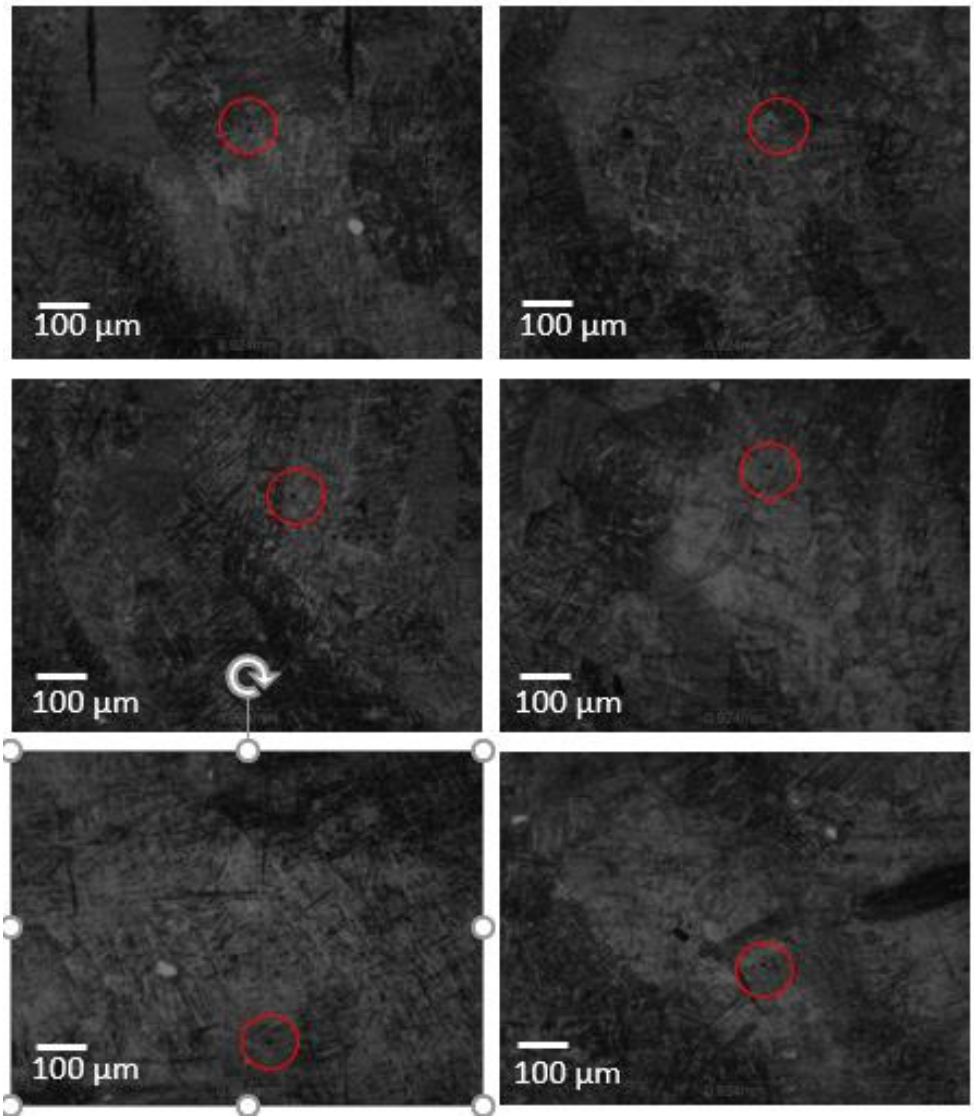

Figure 32. Row 4 Impressions

3.5.3 Unloading Characteristics

Due to the unloading curve, the residual depth or final depth was determined due to the elastic behavior of the material. It was noticed that the depth behavior corresponded similarly to the maximum depth for all cases. The residual depth decreased until the center of the deposition and increased slightly at the top of the deposition. The previously mentioned reasons for this change in behavior for the maximum depth values would be valid for this occurrence as well.

To further understand the relationship between the residual depth and the maximum depth, the ratio of the two values were considered. It had been suggested that this ratio could be a factor to represent structural integrity [58]. More specifically, it was stated that higher values of the ratio correlate to a more tensile residual stress present, whereas lower values could represent a more compressive residual stress [58]. For the nanoindentation results, there was a slight decreasing trend when increasing the height along the sample's cross-section. This could mean that as the sample surface increased in height, the residual stresses present could be more compressive. Another important characteristic was that the average value was approximately 0.65, which was close to the threshold established for work hardening (0.7). Typically, the piling-up of the material on the indenter is significant for low work hardening rate [2]. Thus, for values less than 0.7, work-hardening and pile-up are not significant. The average value of 0.65 indicated that pile-up may not have been a problem for Ti-6Al-4V.

Furthermore, the elastic modulus was calculated with respect to the initial unloading curve. For the bottom of the substrate, the value was determined to be approximately 112 GPa, which was close to the material property of wrought Ti-6Al-4V. This suggested that little to no stress existed at this location. Increasing through the substrate to the center of the deposition, the elastic modulus also increased to a maximum value of 146 GPa. A slight decrease was then exhibited for the last test location, which was located at the top of the deposition. This trend was seen for the hardness values. The direct correlation between the hardness and elastic modulus was expected. If a material is becoming harder, the stiffness or elastic modulus would further increase as well. This supported the validity of the results.

It was evident that the elastic modulus for the wrought and the deposited Ti-6Al-4V varied. This phenomenon has been documented in numerous studies [25,37]. For instance, one particular study compared the material properties of as-built LENS Ti-6Al-4V and wrought Ti-6Al-4V through tensile and fatigue tests [25]. It was experimentally determined that the as-built LENS Ti-6Al-4V elastic modulus was slightly enhanced to 119 GPa, while less elongation was noticeable as well [25]. However, a large deviation in results was present when performing the tensile tests on the LENS specimens [25]. This was believed to be due to the internal defects from the process or powder imperfections [25]. Another report documented the change in wrought and DED Ti-6Al-4V [37]. However, the means of depositing the layer was through an electron beam, and multiple 1 cm tensile samples were cut from the 5 cm deposition thickness [37]. Two zones were analyzed based on the height of the deposition, where zone A was near the bottom and zone B was towards the center or top of the deposition [37]. The elastic modulus for zone A was calculated to be 120.7 GPa and zone B was 126.3 GPa [37]. This not only showed an increase of the elastic modulus in relation to the wrought material, but it also depicted variation in the AM part itself.

As for the trend along the cross-section in this nanoindentation study, the elastic modulus behavior could be due to similar reasons mentioned for the nanoindentation hardness. More specifically, the elastic modulus is an intrinsic property of a material and should be a fixed value. Thus, based on the different properties in the substrate and deposition, another characteristic was at play. As mentioned before, when residual stresses are present, the nanoindentation hardness is affected due to the calculation of area. Based on the Oliver-Pharr method, only the sinking in of the material is considered, not the pile-

up of the material around the indenter. When residual stresses are present, the contact area is affected. Depending on the tensile or compressive natural of the existing stress, the calculation of the incorrect impression area could occur. Thus, the elastic modulus could be over or under-estimated. In addition, the microstructure may be a factor in the change of material properties. It is possible that finer or coarser microstructure may exist throughout the sample due to the thermal effects. Therefore, a synergistic effect may be seen in the nanoindentation results between the residual stress and the microstructure; thus, other methods would need to be applied to untangle these two features.

3.6 Conclusion

Based on the nanoindentation test results, each row seemed to have variability, which showed to be around 30 nm. However, due to performing ten tests for each row, the results appeared to give an accurate representation of the behavior. After averaging the results of each row, it was noticed that the loading curvatures varied with respect to the height along the sample. This variation was also reflected in the calculated nanoindentation hardness and elastic modulus values. The difference indicated that there was an anisotropic behavior present in the DED Ti-6Al-4V sample. Based on the nanoindentation mechanical properties, the material was enhanced in strength compared to its wrought counterpart.

Regarding the microstructure, the hardness and stiffness of the material would be affected by the size and phase distribution of the grains. It would be likely that the combination of a finer microstructure and predominantly more α phase could strengthen the titanium alloy. When comparing the results from the image analysis of Chapter 2 and the nanoindentation results of Chapter 3, a direct relation between the α fraction and the nanoindentation mechanical properties resulted. For example, the α phase increased

slightly halfway through the deposition, but decreased when the top portion was reached (through the investigation of four heights). As for the hardness and elastic modulus in the deposition, both values reached a maximum in the center of the deposition, but decreased at the top (through the representation of three different heights). Theoretically, these results corresponded well to each other, however, possible errors in performing the image analysis may have led to a serendipitous result.

Overall, the results verified that the DED process induced anisotropic behavior. Due to the extraction of heat from the substrate and the rapid cooling rate during solidification of the material, the mechanical properties were affected. More specifically, the increase of row 2 through row 4 in hardness and elastic modulus can also be due to the microstructure change. However, the variation from row 1 to row 2 and the decrease in hardness from row 4 to row 5 could be due to the proximity of the free surface. Investigation into the processing parameters would help to further contribute to the understanding, optimization, and enhancement of the DED process.

Chapter 4: Nanoindentation Based Mechanical Characterization - Multi-Loading Indentation Experiments

4.1 Introduction

4.1.1 Multi-Loading Indentation

Advancements in nanoindentation machines and instruments have established dynamic testing techniques that utilize the repeat testing of a single position [45]. Traditional methods apply a progressive load on a material until a maximum value is reached, then the indenter is unloaded. This can be considered as a single cycle test and allows for the determination of a single hardness or elastic modulus calculation at a specific indentation load and depth. With dynamic testing techniques, the material is repeatedly loaded and unloaded. Therefore, for each loading and unloading portion, mechanical properties such as hardness and elastic modulus can be calculated. This repeat loading and unloading would help to examine the deformation reversibility and to achieve a more elastic behavior in the unloading curve for analysis purposes [45]. Furthermore, depending on the loading condition, mechanical properties could also be found at different loads and depths based on one test. This technique would be useful, especially for nonuniform materials, such as graded or multilayer specimens, where the microstructure or mechanical properties vary with depth [45]. In addition, the reloading feature on porous materials, like bones, could help eliminate the adverse effects from the pores [47].

There are two established loading methods that utilize multiple loading conditions, which are termed as continuous stiffness measurement (CSM) technique and multi-load cycle. CSM is a method in which a harmonic load is added to a nominally increasing force [45]. Thus, small oscillations are present during the loading cycle of the tests. For each

oscillation, it acts as a loading and unloading curve, which can be used to calculate various material properties. The test is usually performed with a Berkovich tip and a frequency of 45 Hz; however, the amplitude of the cyclic load and the maximum load is dependent on the material [45]. As for the multi-cycle method, there are two further subcategories used, which includes the use of a constant or progressive load. Both load conditions require the specification of the number of loading cycles, referring to the amount of times the indenter is loaded and unloaded, and the percentage of the maximum load for unloading during the intermediate cycles.

The use of multiple loading conditions has expanded the capabilities of nanoindentation. Due to the repeat load cycles, especially with sinusoidal loads and high frequencies, it can act like a nanoscale fatigue test [45]. This would benefit the analysis of thin films and microbeams, magnetic storage devices, and microelectromechanical systems (MEMS) technology [45]. For example, the change in contact stiffness of these materials during a nanoindentation test could be monitored and since damage formation affects contact stiffness, the nanoscale fatigue behavior could be examined [45]. An additional factor that can be acquired is the creep behavior of materials. Creep is a material property in which time-dependent deformation happens when a load is applied [45]. This phenomenon is characteristic of polymers and metals at elevated temperatures [45]. For an indentation creep test, a constant load is applied, and the indentation depth is tracked with respect to time [45]. Thus, creep measurements on the nanoscale can be done by comparing the changes in displacement with stress relaxion [45]. When considering standard tensile creep tests, CSM is beneficial due to the ability to model creep based on asperity contact [45].

When utilizing the multi-load method, certain factors need to be considered for reliable and accurate results. For instance, compared to the single indentation test, the process will inherently take longer when the greater number of cycles and percentage of unloading is used. Due to the length of time, a phenomenon known as thermal drift may need to be considered [42]. Thermal drift refers to the heat that is generated during the indentation process and how it can cause additional linear movement that is read by the depth sensor [42]. Thus, the longer the indentation cycle, the more heat generated, and the greater the chance there is of the rate of thermal drift changing and affecting the results [42]. The CSM method, however, is not affected by drift because of the cyclic loading. This would make the use of CSM for creep tests ideal due to the extended periods of time that could be achieved [45]. Another factor that should be taken into consideration is the projected area. Due to the repeat loading in the same position, the impression area may change throughout the process and be difficult to obtain the true contact area.

4.1.2 Objective

As mentioned in the previous chapters, DED induced features, such as the variation in mechanical properties and the existence of residual stresses, are a concern. Thus, the same DED Ti-6Al-4V sample and cross-sectional surface was experimented on, however, the multi-loading technique was utilized. Therefore, when performing the multi-load nanoindentation tests, the variation in load vs. depth curve, maximum penetration depth, final depth, hardness, and elastic modulus were analyzed based on the distance from the bottom of the substrate. These results were compared and verified to the results from Chapter 3.

4.2 Method

As outlined in Section 3.2, the same methodology was applied to the multi-indentation technique. For determination of the nanoindentation hardness and elastic modulus, the Oliver-Pharr theory (equation 1-9) was utilized. In addition, when using the equations, the same area function previously determined for the Berkovich indenter was used for the calculations (equation 10). The only difference in methodology from Section 3.2 was that the final unloading curve for the multi-indentation testing was analyzed.

4.3 Experimental Procedure

4.3.1 Sample Preparation

The same sample prepared in Section 3.3.1 was utilized for the multi-loading indentation testing. It consisted of DED Ti-6Al-4V that was deposited as a 2 mm layer on wrought Ti-6Al-4V substrate of 2 mm thickness. The area of interest was the cross-sectional area; therefore, it was cut in the center (in the direction it was built) and measured to be 13 mm by 7.5 mm by 4 mm. The surface was polished and a mirror finish was achieved using colloidal silica polishing suspension. The sample surface was ultrasonically cleaned using acetone, methanol, and deionized water.

4.3.2 Test Parameters

Multi-load nanoindentation tests were performed with a Berkovich indenter, which had a manufactured radius of 70 nm. The tests were conducted at room temperature using Nanovea's Mechanical Tester Machine equipped with a nano-module. A 5 x 10 grid was utilized for the test spacing, which resulted in a horizontal distance of 1.18 mm and a vertical distance of 0.67 mm separating each test. The specimen and test locations can be seen in Figure 33. The software module was load-controlled; therefore, the prescribed

maximum load was inputted as 150 mN, with a loading and unloading rate of 300 mN/min. For the multi-load setting, it was specified to cycle (unload and reload) 3 times to 90% of the maximum load each time. Thus, one test was approximately three minutes long. These parameters were in conjunction with the prescribed conditions recommended by the machine manufacturer.

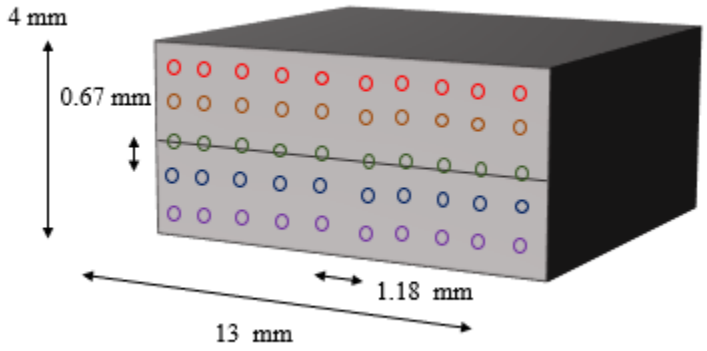

Figure 33. Multi-Load Indentation Test Positions

4.4 Results

For calculations and analyses, it was assumed that the behavior of each row acted in a similar manner; therefore, the analysis is based on the variation of nanoindentation results with build height. A depiction of the typical behavior within each row is presented in Figure 34 utilizing row 1 data.

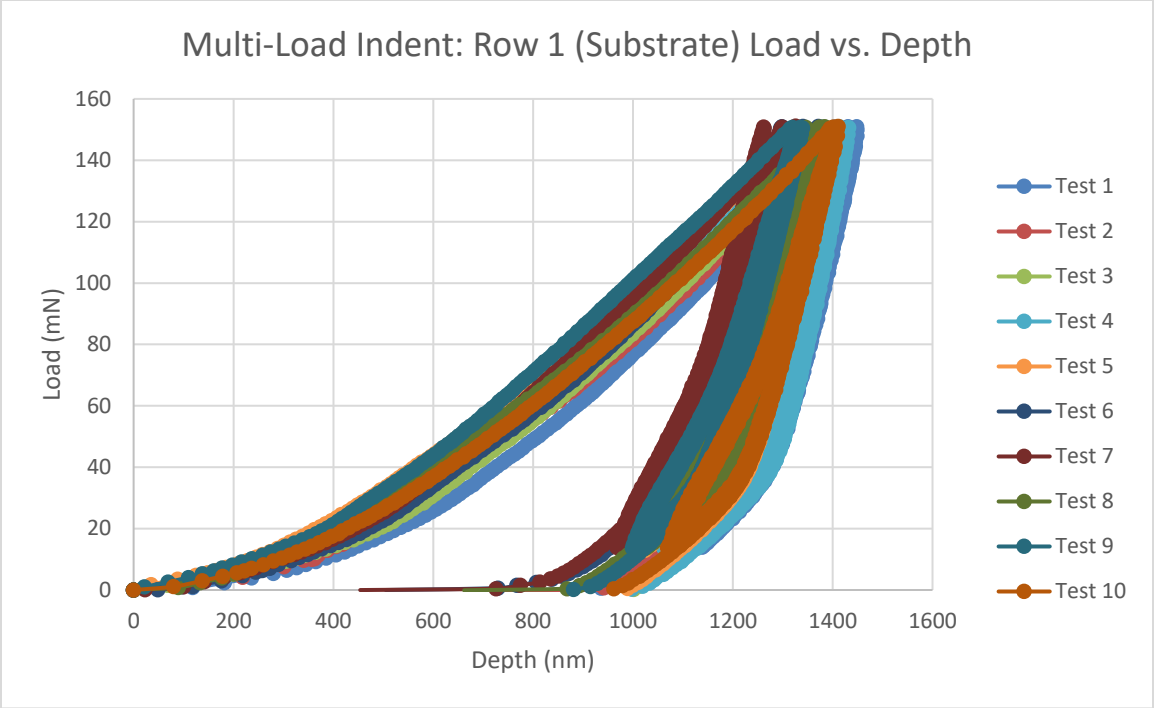

Figure 34. Multi-Load Indent: Row 1 (Substrate) Load vs. Depth

For comparison, the experimental loading curves based on the sample height can be seen in Figure 35. The experimental curves were aligned to begin at the zero depth and the zero load measurements, which was in accordance with the ASTM standard for nanoindentation. Similarly, the experimental unloading curve behaviors are presented in Figure 36.

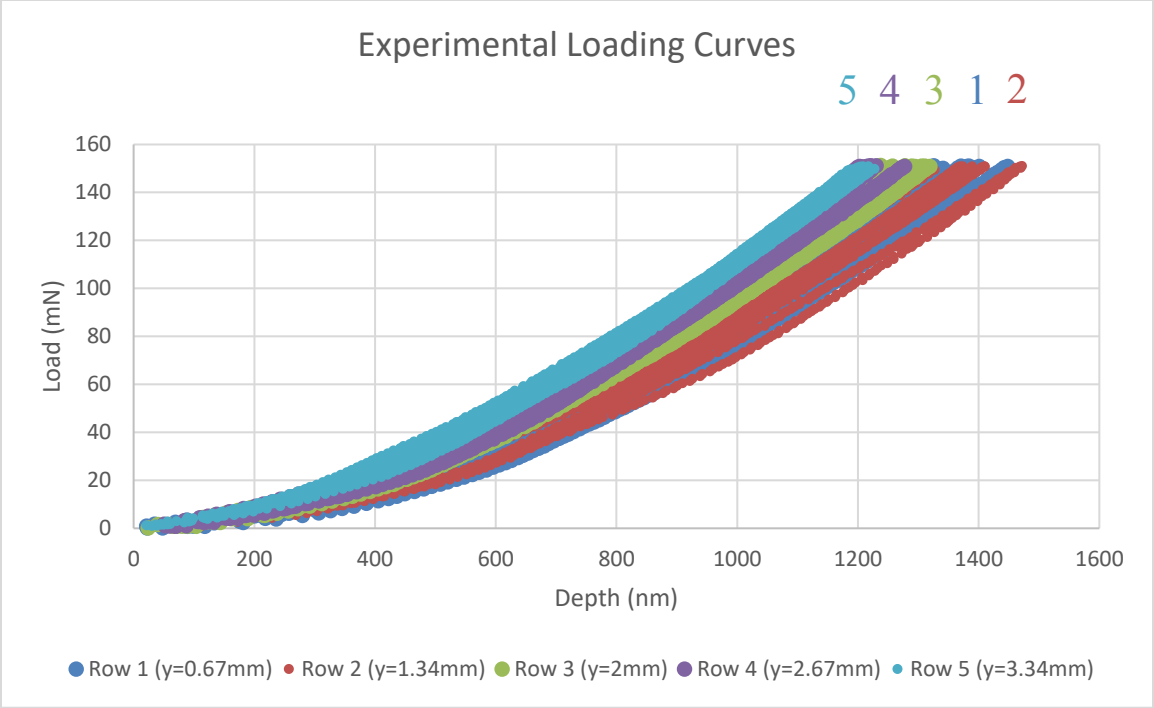

Figure 35. Experimental Loading Curves for Multi-Loading

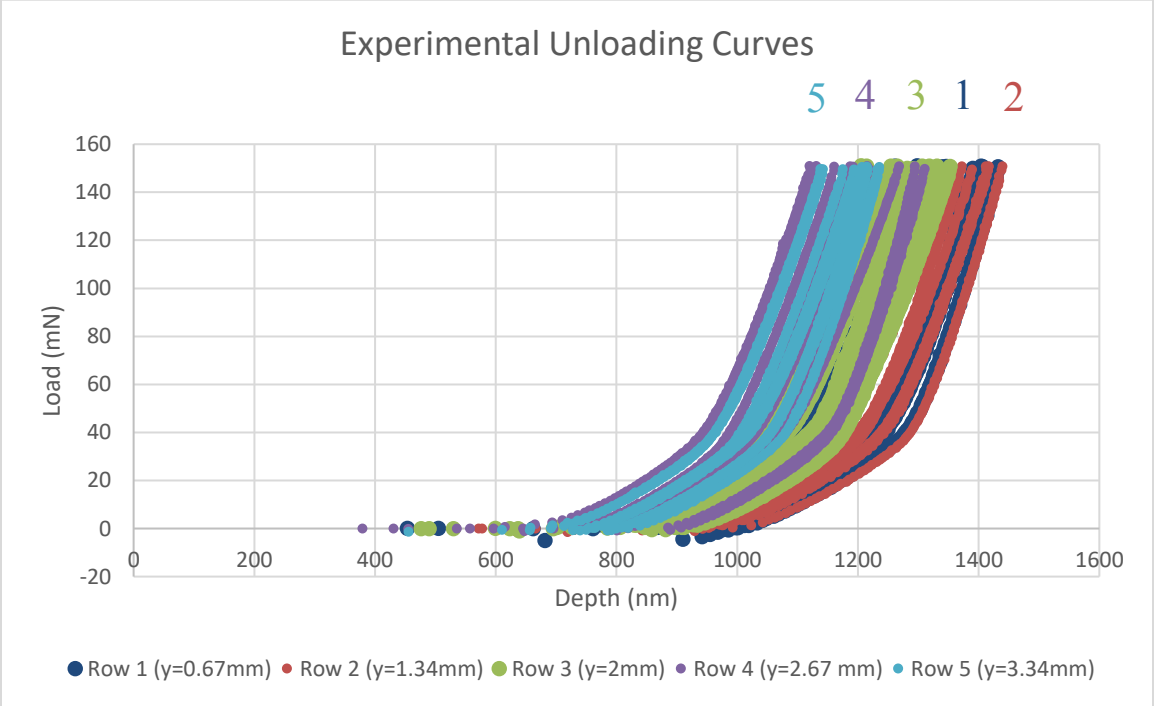

Figure 36. Experimental Unloading Curves for Multi-Loading

A comparison between the single and multi-load indentation experimental data for row 1 can be seen in Figure 37.

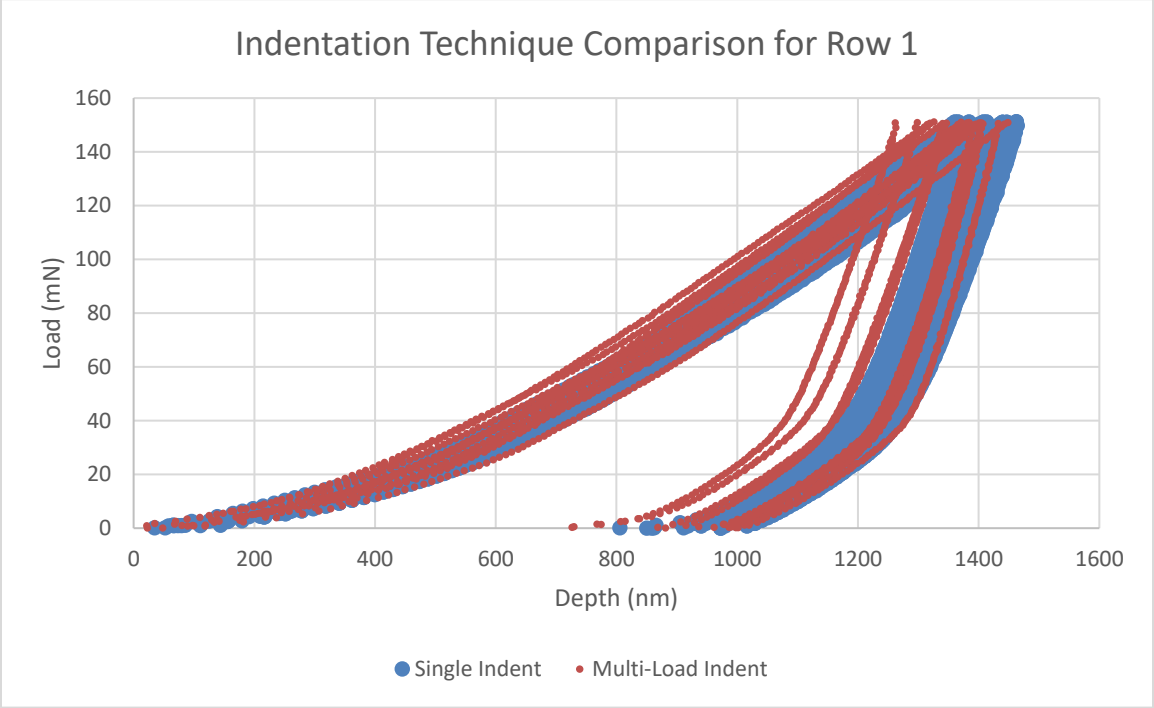

Figure 37. Indentation Technique Comparison for Row 1 Data

The experimental loading curves and unloading curves corresponding to each row were aligned based on ASTM E2546 and fit to one trendline using the power law equation. The loading curves were determined by the same method outlined in Chapter 3. For the unloading curves, the final unloading curve was analyzed. However, the same process used in Chapter 3 to find the power law equation for the unloading curve was used for the multi-load indentation data. The trendlines for the multi-load indentation curves can be seen in Figure 38. The coefficients and exponents for the representative curves can be found in Table 10. Each experimental test was then analyzed to determine the maximum depth and final depth. The contact depth was calculated for each test as well. The depths presented in Table 11 are the average depths for each row. A comparison of the maximum depth for the single indent and multi-load indent method is

shown in Figure 39. For clarity, the maximum depths for the single indent method were offset in Figure 39, however, the same heights were utilized for both techniques.

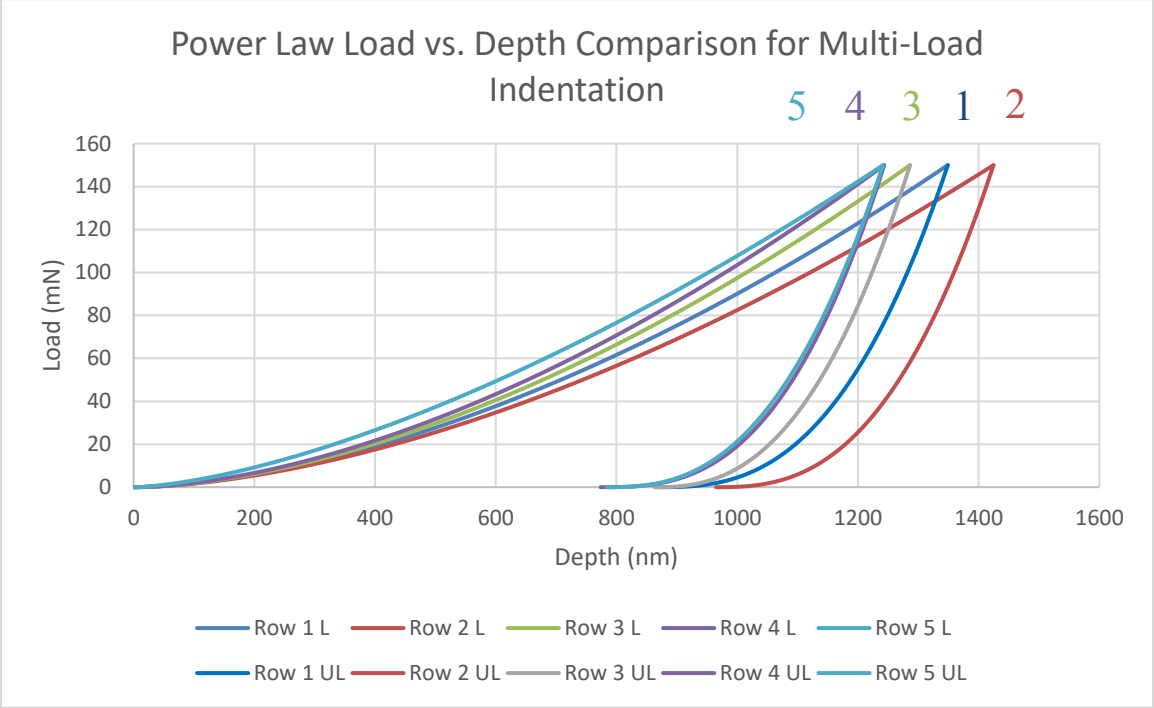

Figure 38. Power Law Load vs. Depth Comparison for Multi-Load Indentation

Table 10. Power Fitted Equation Comparison Based on Height for Multi-Load Indentation

Row	Height (mm)	Loading Coefficient, K_L (mN/nm^{m_L})	Loading Exponent, m_L	Unloading Coefficient, K_{UL} ($mN/nm^{m_{UL}}$)	Unloading Exponent, m_{UL}
1	0.67	0.0007	1.7032	9.0764e-06	2.5956
2	1.34	0.0007	1.6904	1.3944e-05	2.8193
3	2	0.0007	1.7145	3.6775e-05	2.5172
4	2.67	0.0008	1.7039	4.3923e-06	2.8193
5	3.35	0.0028	1.5284	1.8650e-05	2.5956

Table 11. Depth Comparison Based on Height for Multi-Load Indentation

Row	Height (mm)	Contact Depth (nm)		Maximum Depth (nm)		Final Depth (nm)		h_f/h_{max}
		h_c	SD	h_{max}	SD	h_f	SD	
1	0.67	1239.45	69.97	1368.48	54.97	912.58	77.02	0.667
2	1.34	1246.97	59.68	1373.73	55.56	906.31	53.83	0.660
3	2	1153.19	51.85	1282.25	48.17	840.94	66.23	0.656
4	2.67	1081.33	78.93	1209.44	69.17	775.99	77.98	0.642
5	3.35	1074.65	38.95	1196.15	34.35	752.50	43.98	0.629

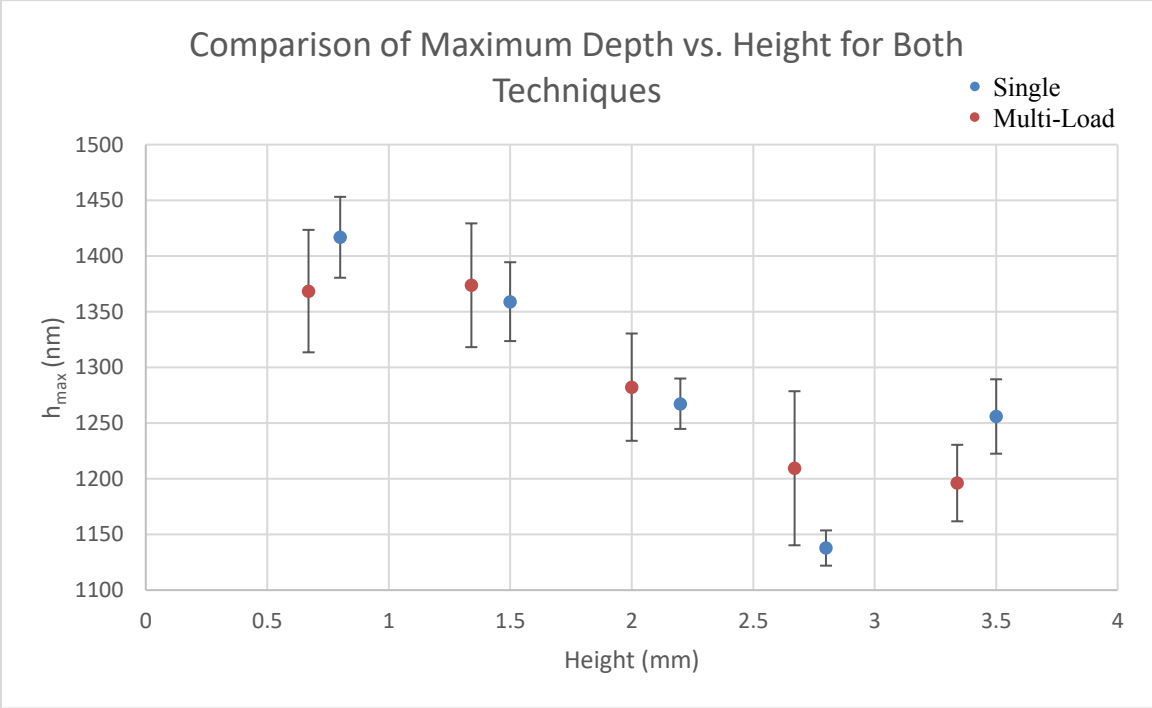

Figure 39. Comparison of h_{max} vs. Depth for Both Indent Methods

As previously seen, due to the affects residual stress can have on both h_f and h_{max}, the ratio of the two depths would further display the nature of the material and the pile-up present. Based on each test within a row, the depth values were directly taken from the load vs. depth curve and averaged. The comparison of the ratio h_f/h_{max} with each technique is presented in Figure 40.

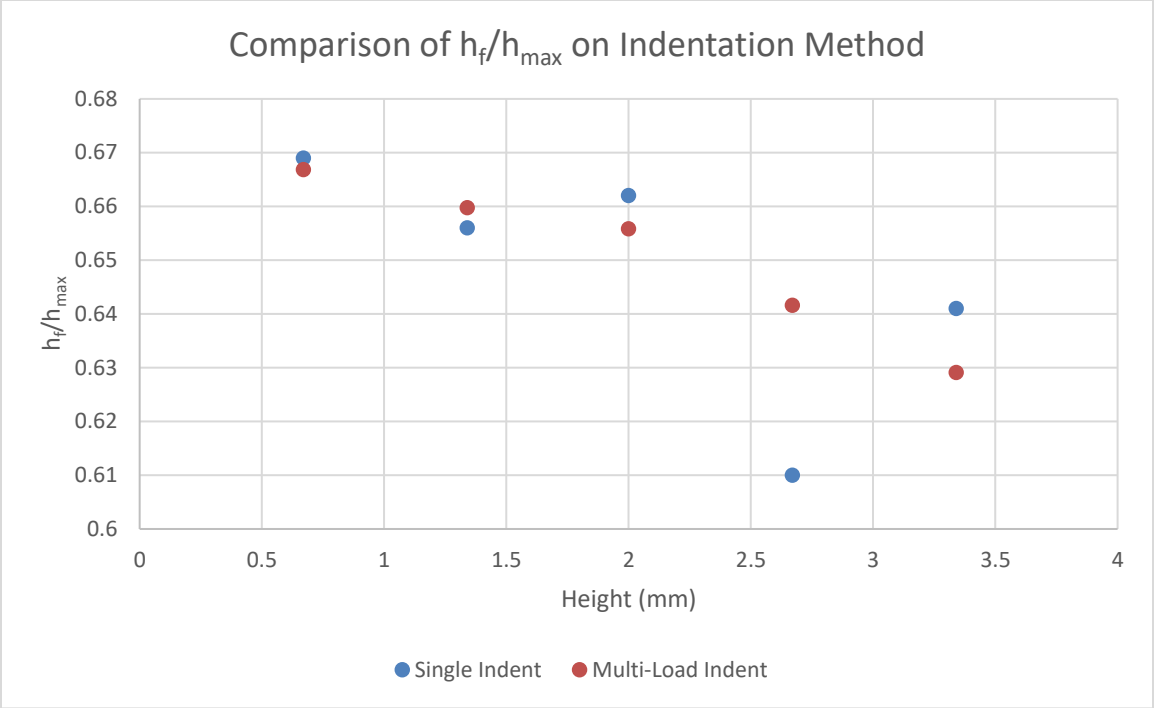

Figure 40. Comparison of h_f/h_{max} on Indentation Method

For each vertical location (row) along the cross-section of the sample, ten hardness calculations were performed and then averaged. The representation of the averaged hardness values for each indentation method based on the build height from the substrate can be seen in Figure 41. In addition, each method utilized the same height dimensions for test positions, however, for clarity, the single indentation hardness values are slightly translated 0.15 mm for presentation purposes.

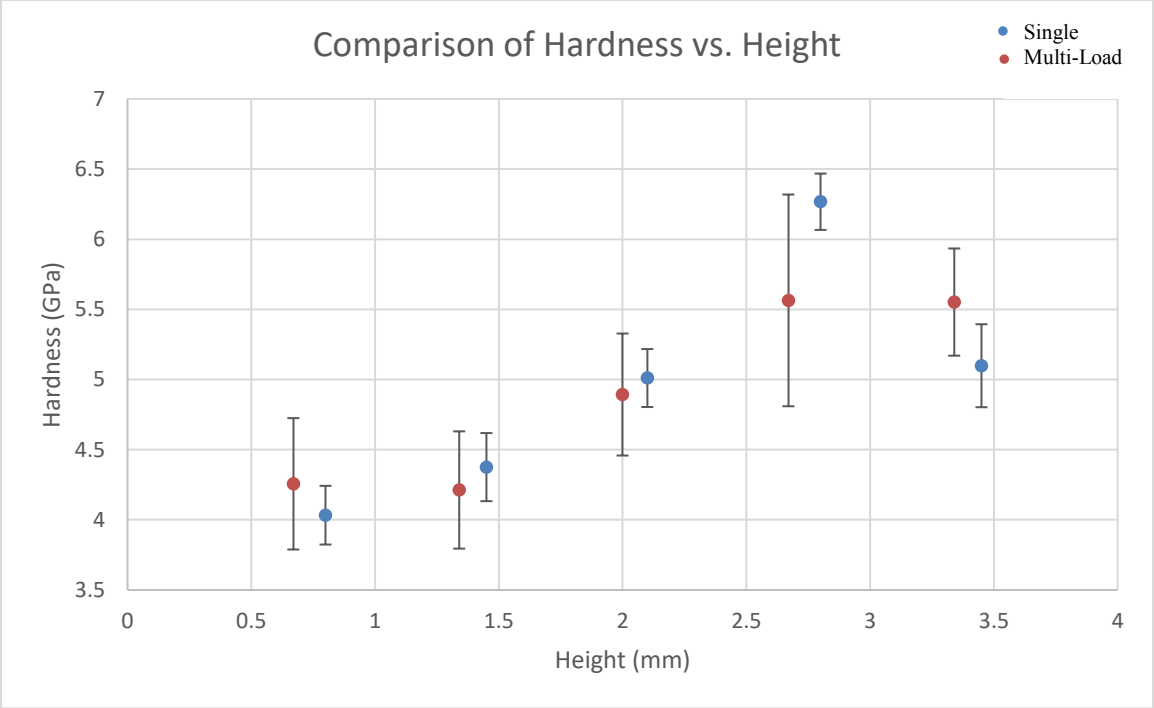

Figure 41. Comparison of Hardness vs. Height

Similar to the hardness calculations, an average elastic modulus was determined using the Oliver-Pharr method and compared based on height from the substrate. The variation of the elastic modulus along the cross-section for each method can be seen in Figure 42. As mentioned for the hardness, each method utilized the same height dimensions for test position, but for presentation purposes, the single indentation elastic moduli values are slightly translated 0.15 mm.

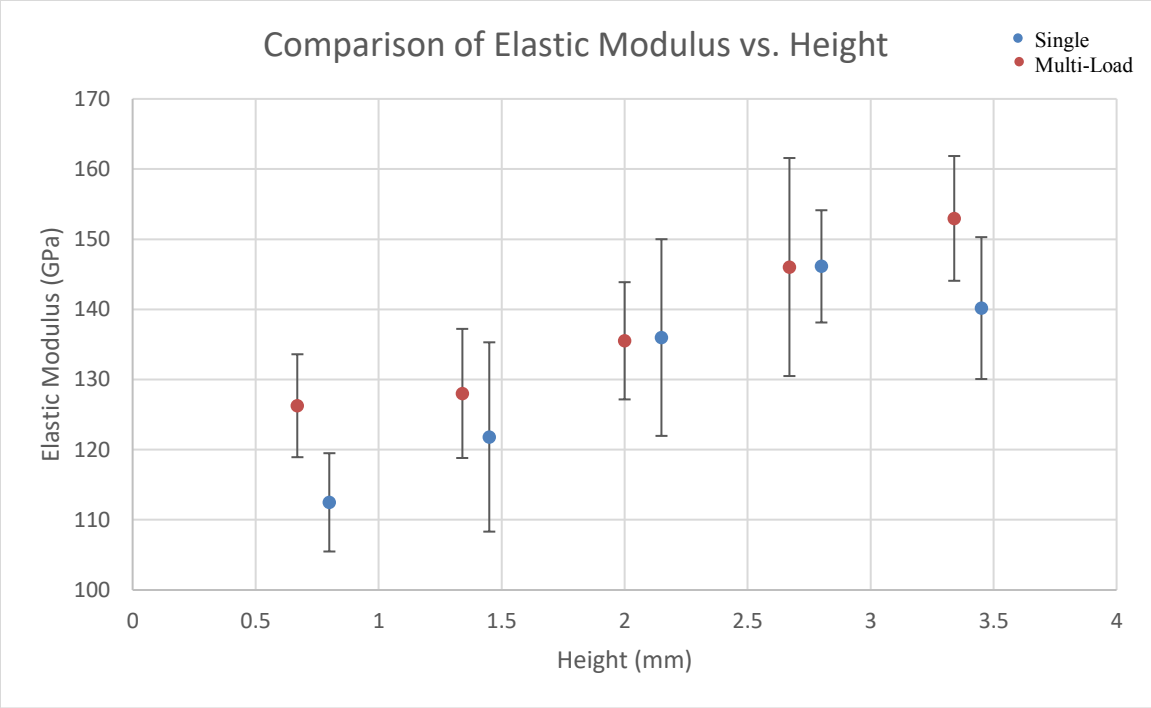

Figure 42. Comparison of Elastic Modulus vs. Height

4.5 Discussion

4.5.1 Load vs. Depth Curves

Similar to the single indent tests, there were deviations within each row. The largest maximum depth value difference for the multi-cycle tests was 188 nm in row 2 (substrate). This was a similar occurrence in the single indent tests. The largest standard deviation based on the maximum depth was 69 nm in row 4 (deposition) for the multi-cycle tests. The smallest maximum depth value difference and standard deviation on h_{max} was 97 nm and 34 nm, respectively, which was for row 5 (deposition). Similar behaviors were present for each row, however, more variation in the rows were seen in the multi-cycle than the single tests. This could be due to the testing positions within each row or the repeat loading and unloading that occurred for the multi-load experiments. The distance between the two different nanoindentation tests lend itself to not be within the same columnar grain, which could affect the variation. Yet, it should show consistent results due to the belief that the

positions within the row should behave in the same manner. Theoretically, the row should be the same due to the temperature difference in a whole layer being less than the temperature gradient when comparing surrounding layers. In addition, the alignment for the experimental data (human error) could have affected the variation, even though the same method used was consistent between the two test types.

When examining the experimental loading curves for the multi-cycle tests, a similar trend existed. Even though there was overlapping between the data for each row, as the height along the cross-section was increased (row was increased), the curvature of the loading curves became, for the most part, more inclined. However, when transitioning from row 1 to row 2, the curvature decreased slightly. This could be an indication that the first two rows were similar to each other when referencing Chapter 3's results. Due to the single tests showing an increase in curvature and the multi-cycle tests presenting a decrease in curvature, the behavior can be that there was no difference in curvature between row 1 and row 2. Furthermore, the results of row 4 were also seen to be different for each nanoindentation analysis. In the single cycle tests, the curvature was steeper compared to the curvature for the multi-cycle tests. As previously mentioned, this could be due to the nanoindentation test positions. Theoretically, there should be no difference in the loading curve of a single cycle test and a multi-cycle test on the same sample with the same test parameters. For example, when Lee et al. conducted a single indentation and multi-indentations on a SS400 steel beam, the loading curves were precisely aligned with each other [4]. Thus, the microstructure or alignment of the data could have caused the variation in this study.

Using the loading data, a trend line was found based on the power law using nanometers and millinewtons for the depth and load units, respectively. For the unloading curves in the multi-cycle tests, two curvatures existed for high and low loads, which was also the case for the single tests. This made sense because, if full elastic recovery was achieved, the unloading curves would be the same. Thus, the two curvatures of the unloading curves were most likely an artifact of the experiment. In addition, it could be possible that a full elastic recovery was not achieved in the single indent tests, however, that would have affected only the initial unloading slope.

For the trendlines of the multi-cycle, a similar behavior for the experimental data was seen. For the same load established, the penetration into the surface became less compared to the substrate. The maximum depth values were compared to ensure that the trend lines were an accurate representation, which is presented in Figure 43. It was seen that the values predicted by the equation were within the standard deviation of the maximum depth values for each row except for row 5. A slight overestimation in the value was seen by approximately 10 nm. This is due to row 5 having the smallest standard deviation. However, the relation between each maximum depth value was what existed in the experimental data.

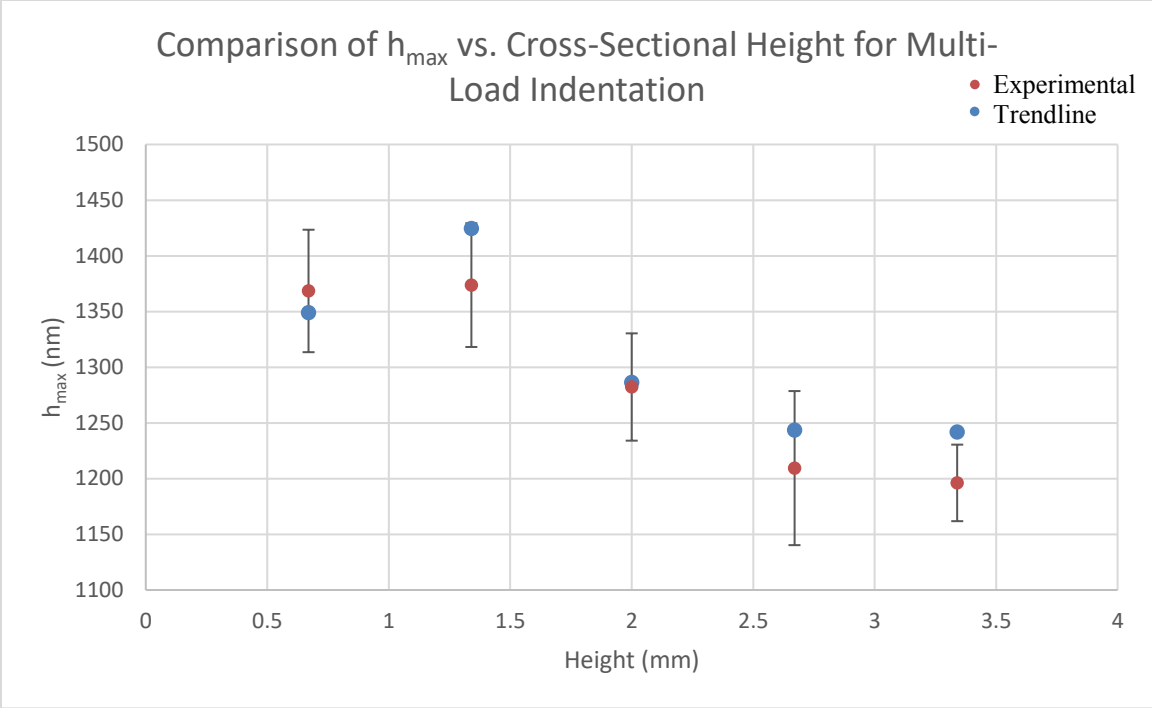

Figure 43. Comparison of Maximum Depth vs. Height for Multi-Load Indentation

Furthermore, the exponents were compared for the loading and unloading curves. For the loading exponents based on the cross-sectional height, there were minor variations. Each row had the exponent of approximately 1.7 except for the fifth row, which showed a decrease to 1.5. This would indicate that the loading coefficients were the source of curvature to match the experimental data. In addition, the difference in exponents made sense due to other characteristics being involved at the deposition, such as a change in microstructure and possible residual stresses. However, an increase in an exponent relates to less penetration and a harder material. Experimentally, the material became harder, however, the exponent decreased. This would show that the exponent was not the best value for comparison. Thus, comparing the trendline exponents or coefficients by themselves is not an accurate representation. As for the unloading exponent, there was a slight variation, however, it appeared to be consistently around 2.7. Theoretically, the elastic behavior should show the same results for the same material. However, the DED

Ti-6Al-4V is not considered a bulk material due to the documented variation and process induced features, thus the variation in stiffness would exist.

When comparing the loading (Figure 44) and unloading (Figure 45) exponents based on test method, there was not a clear pattern. For two rows, the single test loading exponents were greater, whereas, for the rest of the rows, they were less than what was predicted for the multi-cycle tests. The difference between exponents was approximately 0.1 for each row, except row 4, which amounted to a difference in 0.2. This larger difference in row 4 made sense due to the experimental data variance. As for the unloading exponents, it was more sporadic. The difference in exponent for each method was approximately 0.2 to 0.3, which showed more variation than the loading curve exponents did. This would indicate that the single indent tests did not reach full elastic recovery when unloading or the multi-load cycle caused the material to become stiffer.

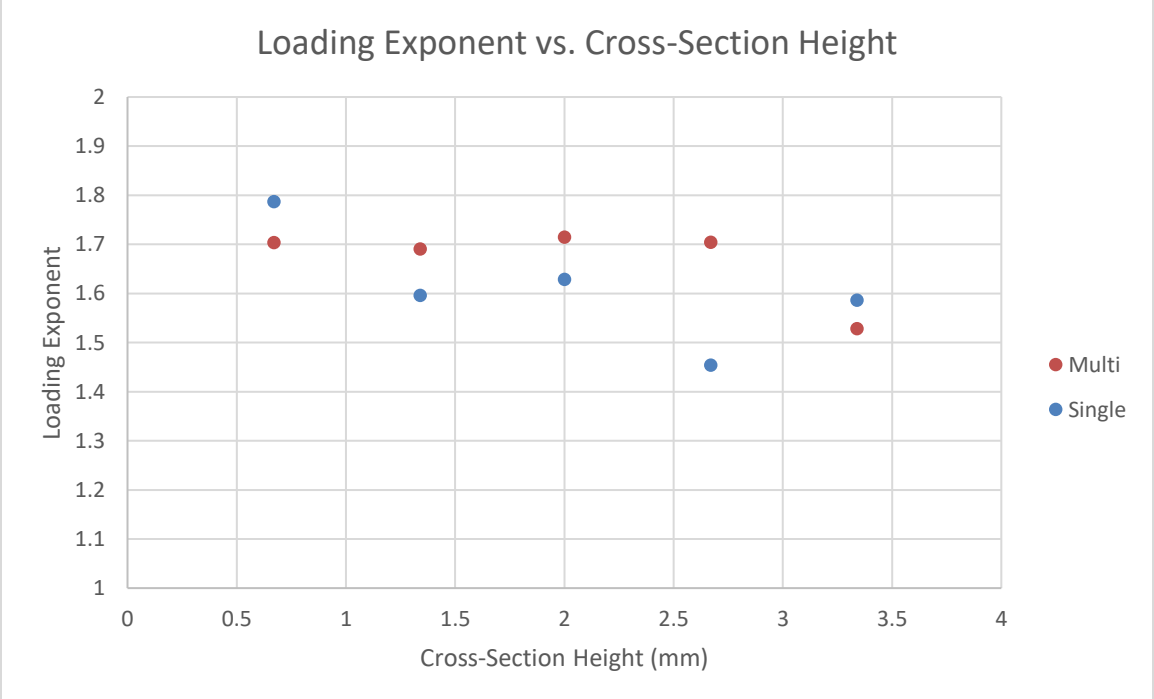

Figure 44. Comparison of Loading Exponent Based on Test Method

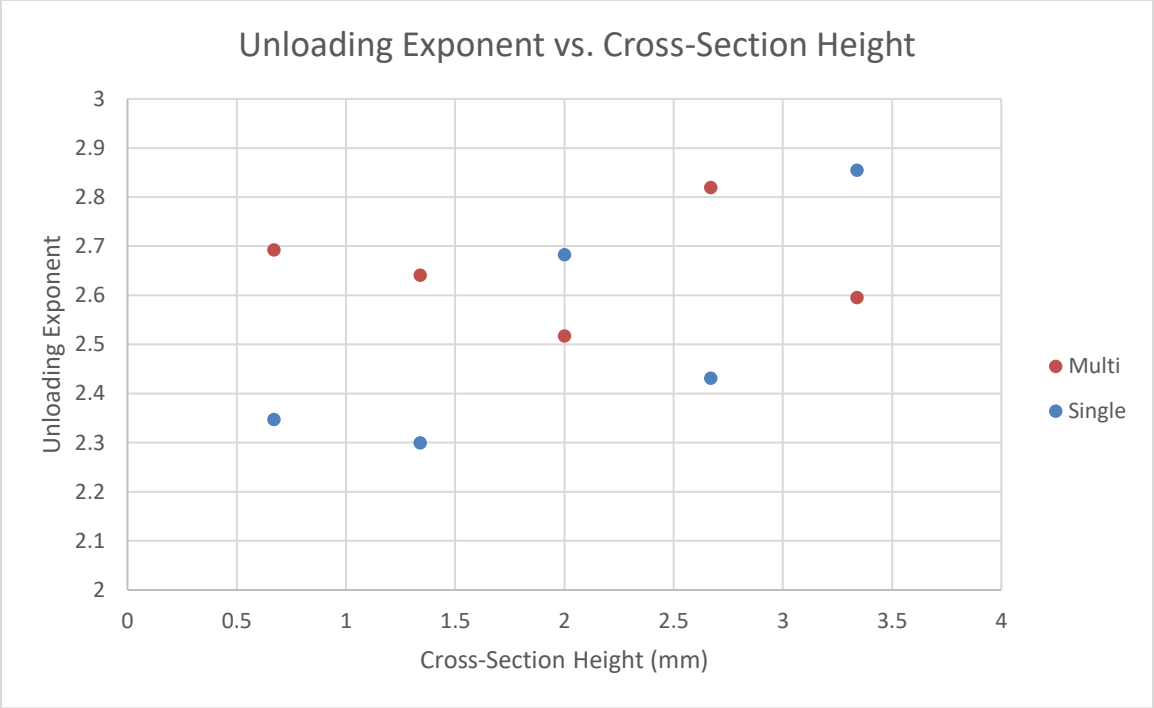

Figure 45. Comparison of Unloading Exponent Based on Test Method

4.5.2 Loading Characteristics

The behavior that was seen through the curves was reflected through the depth values, hardness, and elastic modulus. The maximum depth reached was for the first row (height of 0.67 mm) and was approximately 1368 nm, which was slightly lower than the single test result. However, both average maximum depth values for row 1 were within the calculated standard deviation of the other (Figure 39). As the height of the sample increased another 0.67 mm, the average maximum depth remained about the same. When comparing the second-row average value for both techniques, they were approximately 10 nm different. This consistency ensured the result of the behavior of the second row. When increasing through the interface to the deposition, the maximum depth reached became distinctly lower. Once the deposition was reached, the maximum depth remained about the same (10 nm difference). This indicated that the indenter penetrated the material about the

same. Hardness was also used to further depict this phenomenon (Figure 41). At the substrate, the hardness was about 4.25 GPa, which was slightly greater than what was expected for wrought Ti-6Al-4V. This difference could have related to the more elastic recovery achieved during the multi-load indentation. As the height of the sample was increased from interface to deposition, the material became harder. The maximum average hardness calculated was 5.5 GPa at the top of the deposition. When comparing the two methods, there was an evident difference between the substrate and the deposition, however, the behavior within each layer was less distinguished.

When comparing the substrate values with the deposition values, there was a noticeable increase in hardness. As previously mentioned, the hardness values between the deposition and the substrate have increased from 3.3 GPa to 3.5 GPa for a 10 mm high sample, and 3.2 GPa to 4.4 GPa for a 4 mm high sample in other studies [41,56]. In addition, it has been documented that the process parameters influence the hardness as well. When comparing the two methods used for this investigation, it was more evident that there was a difference between the substrate and the deposition. By examining the average hardness value, it appeared that the substrate nanoindentation hardness was 4.25 GPa and the deposition was 5.5 GPa. This roughly 1.25 GPa increase was about the same increase as seen in the Lei Yan et al. study (1.2 GPa) in which a 4.2 mm testing area was used [41]. Thus, the results through nanoindentation seem plausible.

The behavior within the substrate or deposition layers were less distinct. For the substrate, an increase in nanoindentation hardness of 0.3 GPa was seen for the single indent test, however, the hardness practically remained the same for the multi-load test. In addition, the standard deviation was determined to be approximately doubled for the multi-

cycle test compared to the single cycle test. This occurrence thus lends itself to be explained through grain size. The larger grain size would result in a larger deviation when nanoindenting. Furthermore, each average hardness value for the single indent tests fell within the standard deviation of the multi-cycle tests. This would specify consistency, yet, too much variation was seen to concluded there was an increase in the substrate for this sample. As been stated, residual stresses and thermal mismatch could harden the material, however, the effective zone within the substrate is uncertain. In addition, the effects from the DED process could have reached through the two rows (substrate) that were measured. This would explain the enhancement of the hardness from the wrought value. Another possibility for the enhancement could be due to the area function calibration. It was possible that a human error could have occurred when the area function was calibrated, which could cause all the result values to be slightly off, but this would not affect the relative behavior.

When considering the heat affected zone (HAZ), a strong transition was seen from the substrate to the deposition in the results of both methods. A few studies have reported that the bottom layer of the deposition may exhibit a harder behavior due to a finer microstructure. This factor relating to the process may have been a reason for the transition. Furthermore, additional deformation from compressive residual stresses could also have been a reason for the occurrence.

As for the variation in the deposition, it seemed to be due to the DED process as well, whether it be related to causing residual stresses or affecting the microstructure. Similar to the substrate, a clear trend when comparing the two methods could not be determined for the deposition. For deciding which test was more accurate, the equations

can be considered. The hardness was determined using the contact depth. This depth utilized the maximum load, maximum depth, and slope of the unloading curve. Due to the involvement of the unloading, one would believe that the multi-cycle would be more accurate due to more elastic recovery. However, the determination of area was still a concern. By repeatedly indenting in the same position as multi-cycle does, area calculations may vary compared to the true area. As stated, some papers have documented a variation in the hardness for DED materials [41,56]. The conflicting results between how it behaves further made sense. It appears that a standard is lacking for manufacturing of DED materials and the processing parameters. For this study, more nanoindentation tests performed and an understanding of the processing parameters may have established a clearer behavior for within the deposition layer.

4.5.3 Unloading Characteristics

Due to the unloading curve, the residual depth or final depth was determined due to the elastic behavior of the material. A similar trend compared to the maximum depth was noticed for most of the rows, where there was an evident decrease from substrate to deposition. However, a greater decrease in the final depth from row 4 to row 5 was more prominent that the maximum depth value results. To further investigate the final depth, the final depth to maximum depth ratio was analyzed. A more consistent decrease in the ratio was seen for the multi-cycle results compared to the single test results. It had been stated that higher values of the ratio correlate to a more tensile stress present and lower values represent a more compressive residual stress [58]. When looking at the substrate and deposition separately, the decrease would relate itself to the existence of compressive stresses.

Furthermore, the elastic modulus was calculated with respect to the initial unloading curve. For the lowest row on the substrate, the value was determined to be 126 GPa, which is larger than the substrate value for the single test method (Figure 42). The elastic modulus than increased only by 2 GPa when increasing in height to the interface. More evident increases in the elastic moduli were present through the rest of the height of the sample. The maximum nanoindentation elastic modulus achieved was 153 GPa. This value was larger than the maximum elastic modulus determined using the single indent technique. When comparing the two methods, the elastic moduli for row 1 was approximately 12 GPa apart, with the multi-cycle being the larger value. For this case, even the standard deviation did not overlap. The rest of the results for each test position were within the standard deviation of the other. For rows 2 through 4, similar results were found between the two methods. For row 3 and row 4, the results were nearly identical, further solidifying the elastic modulus behavior calculated. The last row within the deposition had an increase in behavior for the multi-cycle tests, but a decrease was seen in the single cycle tests. In all, the elastic moduli for the multi-load indentations were either the same or greater than the single indentation results. This suggested that the multi-cycle technique affected the nanoindentation elastic modulus. By indenting in the same position multiple times, more elastic recovery was established and the material became stiffer.

For the multi-cycle tests, the direct correlation between the hardness and elastic modulus was not as prominent as it was for the single tests, but it still existed. When the material was shown to be harder, the stiffness or elastic modulus was enhanced as well. This further supported the validity of the results.

It is evident that the elastic modulus for the wrought and the deposited Ti-6Al-4V varied. This phenomenon has been documented in numerous studies. As previously mentioned, in one study, an increase in elastic modulus of 5.6 GPa was exhibited in a few centimeters difference along the deposition [37]. In this nanoindentation study, the difference within a few millimeters was approximately 27 GPa. This seemed like a significant increase for such a short distance; however, the processing parameters to build the part and the technique for determination were different. The technique used in the mentioned study was through tensile testing [37]. It could be possible that the localized properties varied from the bulk, especially considering how the internal defects from the process or powder would affect the tensile testing method more so than nanoindenting. Another possibility that would explain the possible difference in finding the elastic modulus could be due to the presence of residual stresses. Nanoindentation is greatly affected by residual stress, whether it is tensile or compressive. For tensile testing, if the residual stresses present were tensile, theoretically, less force would be required to break the specimen. However, if compressive stresses existed in the part, more force would be needed to induce failure. Either way, a variation in the material due to the process was detected.

4.6 Conclusion

Through examination of the DED Ti-6Al-4V cross-section, a noticeable increase was seen for the nanoindentation hardness and elastic modulus when transitioning from the substrate to the deposition. This was seen in the single indentation tests as well. The reasons could be related to the processing parameters, the temperature gradient developed between the layers, and the microstructure that was a result of the continuous heating.

When utilizing the multi-indentation technique, the elastic moduli either increased or remained the same regarding the single indentation technique. This was a clear indication that the repeat loading altered the results. By repeat loading and taking a greater amount of time (two minutes more), the material was able to recover more elastically. In addition, DED Ti-6Al-4V is a textured material. The multiple load cycles thus would more accurately determine the mechanical properties. Therefore, the behavior that was observed through this method was believed to be a more accurate representation of the mechanical behavior along the cross-section.

Chapter 5: Determination of Residual Stress

5.1 Introduction

5.1.1 Residual Stress

Residual stresses can be developed through inhomogeneous plastic deformation and manufacturing processes. With additive manufacturing processes like DED and SLM, a high-power laser is utilized to melt and build the part one layer at a time [6]. The heat would travel slowly through the previously placed layer and the top layer would experience expansion, cooling, and contraction, which produces residual stresses [6]. This is similar to the welding of materials. The residual stresses in AM can be either tensile or compressive and have been seen to vary in AM parts. For instance, it has been reported that residual stresses in direct metal laser sintering (DMLS) parts have been highly tensile and their magnitudes may have been based on sample height [12]. Others have reported that tensile stresses are larger at the top of the part and at the interface between the substrate and the deposition [12]. Overall, the residual stress distribution has varied due to the use of different processing parameters and material properties [12].

The existence of residual stresses in structural components and parts is important to understand due to their effect on structural integrity and mechanical behavior. There are various destructive and non-destructive methods to quantify residual stresses in materials. Determination methods for residual stresses that have been applied to AM parts include the stress relaxation through hole drilling and the use of X-ray diffraction. One investigation was done by Knowles et al., in which residual stresses were measured for a selective laser melted Ti-6Al-4V using the hole drilling method [27]. The hole to depth ratio was varied to investigate the percentage of strain relieved based on the detection from

strain gages [27]. It was determined that the residual stresses were non-uniform and they approached the yield strength of the material [27]. Another experimentation was performed by Yang Liu et al. that involved the use of X-ray diffraction to measure the residual stress of a 316L stainless steel specimen manufactured using selective laser melting (SLM) [5]. When using X-ray diffraction, which is one of the most common determination methods, the interplanar spacing for stressed and unstressed lattices were compared [11]. Multiple samples were manufactured of varying build height to understand the behavior of the residual stresses [5]. It was determined that at the bottom of the deposition for three different samples of heights 12 mm, 16 mm, and 20 mm, the residual stresses were compressive [5]. At the center of the deposition, the maximum compressive stress was achieved, and at the top of the deposition, the residual stress was at its peak tensile value [5].

The mentioned methods are the traditional means for determining the residual stress. For each method, there exists advantages and disadvantages. For the hole drilling approach, factors such as the hole depth and the bonding of the strain gages could affect the results [27]. This destructive approach would also have its limitations in industrial applications [27]. As for X-ray diffraction, the penetration of the x-rays into the material may be too shallow, however, the ease of use is appealing [9-11]. Another technique that has the potential to be utilized is through indentation. Indentation can be applied efficiently and on a range of scales. It was discovered that when a force was applied to a material, the nanoindentation results would vary compared to the unstressed results. It has been noticed that applied stresses affect the nanoindentation hardness, loading curve, unloading curve, material pile-up, and contact area [3,9]. For instance, Lee et al. performed an investigation

on a heat-treated SS400 steel beam by designing a uniaxial stress-generating apparatus [10]. In conjunction with strain gages mounted on the sample, a bending stress was applied and nanoindentation tests were performed along the surface [10]. Through the nanoindenation results, the loading curves were defined through a power law fitting and were able to be examined based on varying the applied stress state [10]. It was determined that the exponent became greater for increasing tensile stresses [10]. Thus, by understanding the behavior of the nanoindentation results for a known force or stress, nanoindentation could then be applied to a material with an unknown stress state. This has led to the derivation of various models, such as the Suresh Model, Lee Model, Xu Model, and Swadener Model, which focuses on the use of different characteristic parameters and indenter types to calculate the residual stress [3,9].

5.1.2 Effects on Nanoindentation

The investigation on using experimental and simulated indentation techniques to understand and quantify residual stresses in materials is a topic of interest. Studies and experiments have been conducted on various materials through the application of stresses to determine the effects on nanoindentation load verses depth curves, as well as the intrinsic material properties. It has been proven that the application of a constant stress or the existence of residual stresses affects the nanoindentation hardness, loading curve, unloading curve, material pile-up, and contact area [3,9].

As for the load verses depth curves and how residual stresses influence them, noticeable shifts have been documented in the curves when applying tensile and compressive loads to various materials. More specifically, for fixed depths, the loading curves for tensile stresses are lower than those for the stress-free state, which can be seen

in Figure 46 [10,27,48,49]. Similarly, loading curves of a material with a compressive stress state is higher compared to the curves for stress-free state [10,27,48,49]. This was shown through various experimentation on materials such as SS400 steel, API X65 steel, and (100) tungsten [10,27,48,49]. The behavior is due to the compressive stress constraining the indentation plasticity, leading to a higher indentation load; whereas, the tensile stress boosts the indentation plasticity and lessens the load [9]. The unloading portion of the curve correspondingly shifts due to the loading behavior. For a compressive stress state, the curve will be displaced leftward, and for a tensile stress state, the curve will move rightward. Thus, more elastic recovery and a smaller residual depth would be characteristic for compressive stresses, and the opposite would occur for tensile stresses [9].

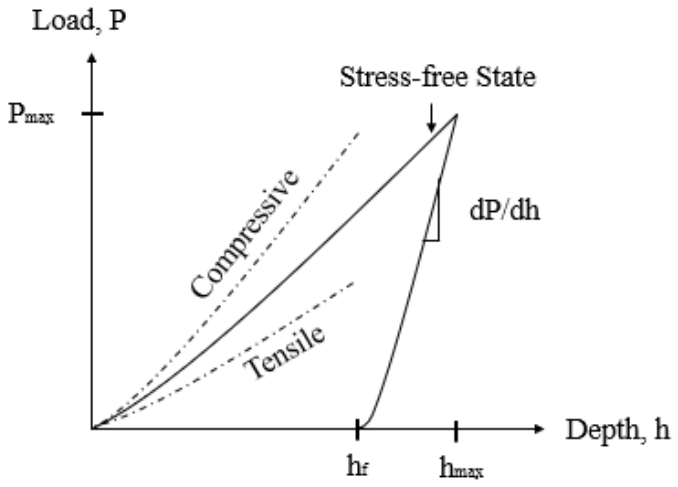

Figure 46. Effect of Residual Stress on Nanoindentation Curve

When using standard methods (mathematically determined projected area) for calculating the indentation hardness, the hardness has been seen to decrease with the existence of tensile stresses and increase when compressive stresses were present

[10,27,48,49,58]. For example, a study was done on an Al 8009 alloy under uniaxially and biaxially applied stress where the hardness was analyzed using a mathematically calculated projected area and a contact area found through optical techniques [3]. It was determined that the indentation hardness varied with applied stresses when using the calculated area, however, there was a minor change in hardness when visually determining the area [3]. The discrepancy with the value of the hardness and the projected area has been proven to be an experimental artifact due to the influence of stress on the material pile-up around the indentation impression [3]. For this case, the calculated area deviated by up to 15% [3]. This phenomenon can further be explained based on the concept of shear plasticity [48,49]. When indenting to a fixed depth, the indenter causes a compressive force on the material, which acts perpendicularly to the surface [48,49]. When tensile residual stresses exist, the shear stress between the indenter and the material increases compared to the shear stress of a surface without residual stresses [48,49]. With an increase in shear stress, the deformation around the indent will increase as well [48,49]. This results in a reduction of hardness [48,49]. If a compressive residual stress was present, the shear stress between the two surfaces would cause less deformation, therefore, resulting in an increased hardness [48,49]. Thus, the nanoindentation hardness estimated by a curve analysis will severely be affected by residual or applied stresses, whereas the true or real hardness will remain the same [3].

To further consider the effects of residual stresses, it is important to consider the pile-up of the material around the indenter and impression. Without the existence of residual stress, the amount of pile-up varies based on different materials. Usually, this is due to a material having a low strain hardening behavior and the incompressibility of

plastic deformation. The pile-up of a material usually increases the effective contact area [42]. In addition, when residual stresses exist, pile-up can further be induced. For a constant depth, pile-up is believed to be larger when large compressive stresses are present due to material getting pushed toward the surface of the indenter. For larger tensile stresses though, the pile-up of the material is relatively smaller compared to the compressive stress because the material will be drawn in to decrease the amount of pile-up, which can be seen in Figure 47 [9]. However, even if a material exhibits a large amount of pile-up, the hardness may not be greatly affected by residual stress when the proper area is considered. An indicator used to determine the work hardening and plastic deformation behavior is defined as the ratio between the final depth and the maximum depth of the nanoindentation test [9]. If this ratio is less than 0.7, only a small amount of pile-up will occur [9].

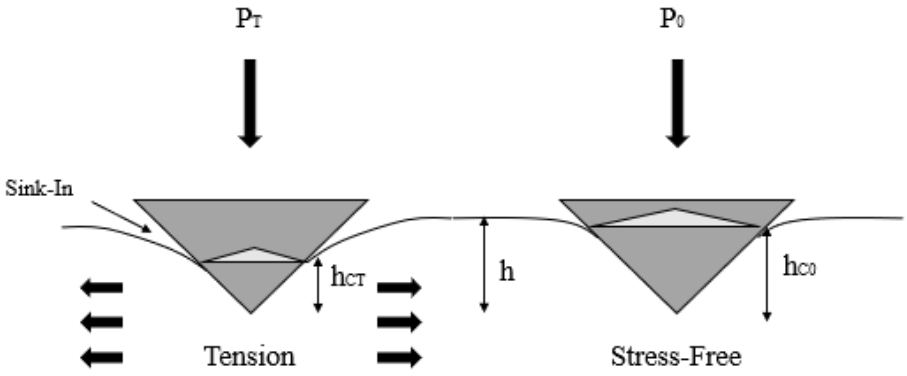

Figure 47. Effect of Contact Area on Tensile Stress State

Similar to the effects of residual stresses on indentation hardness, the elastic modulus is also affected. It has been reported that when compressive stresses are present in a material, the indentation elastic modulus increases [9]. Conversely, when tensile stresses exist in a material, the indentation elastic modulus decreases [9]. The hardness and the elastic modulus are intrinsic properties of a material, thus, the stress applied or existing

should not affect their value. Therefore, when the current pile-up around the indentation impression is not accounted for, it affects the projected area, which in turn affects the elastic modulus.

Additional investigations of residual stress behavior on nanoindentation results have been through finite element modeling. One experiment conducted by Chen et al. modeled and simulated the behavior of various materials when indentation was performed with a sharp indenter [3]. When residual stresses were induced, the ratio of the elastic modulus to the yield strength was compared with the hardness, stiffness, and plastic flow [3]. It was concluded that when E/σ_y was greater than 300, the normalized hardness was not affected; however, when E/σ_y was less than 300, the hardness decreased and the plastic flow was enhanced [3]. In addition, when the elastic modulus to yield strength was less than 30, the contact stiffness was increased with tensile residual stress [3]. Based on the found results, an algorithm was developed to determine the residual stress, yield strength, and elastic modulus if the load verse depth curve was known [3].

5.1.3 Objective

Numerous studies have applied and compared the mentioned traditional residual stress determination techniques with nanoindentation, as well as only observe the effects of residual stresses through load vs. depth curves. For example, a study reproduced comparable results when using X-ray diffraction on a thin aluminum film. However, it has also been reported that there can be a high variability when measuring residual stresses due to the results being sensitive to metallurgical factors, like grain size, texture, and environmental factors [10]. Materials previously studied have been thin films, coating, single crystal tungsten, and various steels. To the best of the author's knowledge, previous

residual stress investigations through nanoindentation have not been performed on additively manufactured materials. Therefore, in order to progress the use of nanoindentation and attempt to understand the material behavior of DED Ti-6Al-4V, the Suresh Model was applied to the nanoindentation results of Chapter 3 and Chapter 4.

5.2 Method

To quantify the residual stress through nanoindentation, the Suresh Method was used. Initial assumptions outlined in Suresh et al. required a frictionless, quasi-static sharp indentation of an isotropic substrate by an elastic indenter [59]. In addition, the material was assumed to have gone through non-uniform cooling from the processing temperature, be a coating or film on a substrate, have an applied bending or normal load, had experienced mechanical working, or exhibited a phase transformation [59]. Thus, the residual stresses that existed were considered to be equal-biaxial (equation 11) and be less than the yield strength if only elastic residual stresses were present (equation 12) [59].

$$\sigma_{x,0}{}^{R} = \sigma_{y,0}{}^{R} \tag{11}$$

$$\left|\sigma_{x,0}{}^{R}\right| = \left|\sigma_{y,0}{}^{R}\right| \leq \sigma_{y} \tag{12}$$

To start the derivation, Suresh assumed that the loading curve of the stress-free and stressed samples acted in accordance with Kick's Law, which is that the load is proportional to the depth squared [59]. However, in Chapter 3 and Chapter 4, it was determined that the loading curves for DED Ti-6Al-4V varied from this law and exhibited exponents ranging from 1.4 and 1.8. Thus, the previously defined power law trends for the loading curve were used instead. Therefore, in general terms, the load-depth loading curve equation for an unstressed and stressed sample were defined as equation 13 and equation 14, respectively, where K_0, K, m_0, and m were already determined coefficients. Similarly, the area function

for the unstressed sample had been determined based on the previously mentioned area function calibration and is presented in a more general form as equation 15. However, the stressed area was yet to be determined, but the general formula is depicted as equation 16, where D_i and $D_{0,i}$ are the fitted coefficients.

$$P_0 = K_0 {h_0}^{m_0} \tag{13}$$

$$P = Kh^m \tag{14}$$

$$A_0 = D_{0,0}{h_0}^2 + D_{0,1}h_0 + D_{0,2}{h_0}^{1/2} + \ldots \tag{15}$$

$$A = D_0h^2 + D_1h + D_2h^{1/2} + \ldots \tag{16}$$

Since the average pressure or hardness is not affected by stress, the stress-free and stressed relationship is defined as equation 17.

$$H = p_{ave} = \frac{P_0}{A_0} = \frac{P}{A} = \frac{K_0{h_0}^{m_0}}{D_{0,0}{h_0}^2 + D_{0,1}h_0 + D_{0,2}{h_0}^{1/2} + \ldots} = \frac{Kh^m}{D_0h^2 + D_1h + D_2h^{1/2} + \ldots} \tag{17}$$

5.2.1 Tensile Residual Stress

When considering tensile and compressive residual stress, separate approaches have to be considered. For a biaxial tensile residual stress at the surface, it was broken into the addition of a hydrostatic and a deviator stress, which can be seen in Figure 48 [59]. The hydrostatic stress is not affected by the plastic deformation caused from the indenter [59]. Thus, the hydrostatic stress was unaffected by the average indentation pressure due to its invariance [59]. The deviator stress component is a uniaxial stress that would induce a differential indentation force (Figure 49) [59]. It was assumed that the residual stress was equal to the hydrostatic stress, as seen in equation 18 [59]. When applying the indentation force to the stressed and unstressed sample, a differential indentation force could be found, which is presented in equation 19. This force is the amount of load that relates to the residual stress.

$$\sigma_{x,0}{}^{R} = \sigma_{y,0}{}^{R} = \sigma_{z,0}{}^{R} = \sigma_H \tag{18}$$

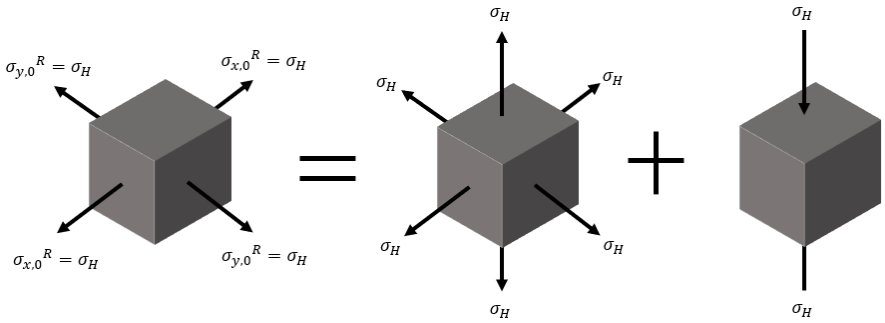

Figure 48. Representation of Residual Stress State

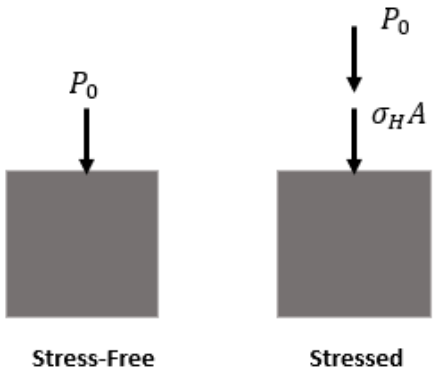

Figure 49. Comparison of Stress-Free and Stressed State

$$dP = \sigma_H A \tag{19}$$

Depending if the indentation process is depth-controlled or load-controlled, a slight adjustment was made for the derivation. This difference is depicted in the following figures (Figure 50 and Figure 51), as well as in equation 20 and 21 [59]. It can be seen that, based on the relationship between the stressed (tensile) and unstressed, the load differential is either added or subtracted [59].

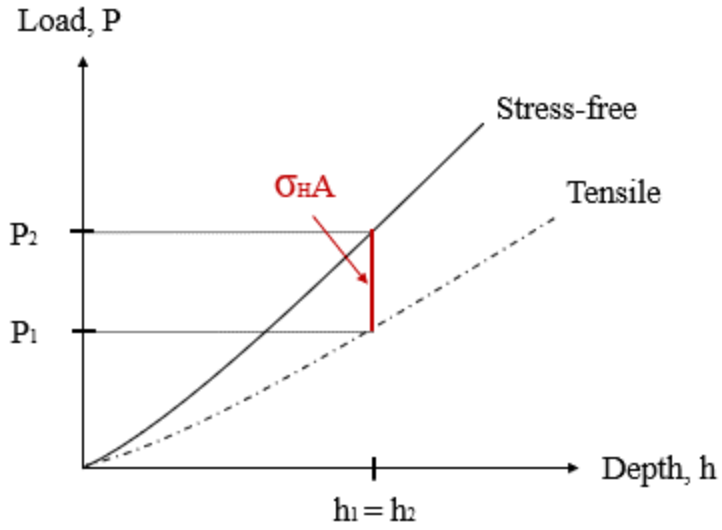

Figure 50. Tensile Residual Stress, Depth Controlled

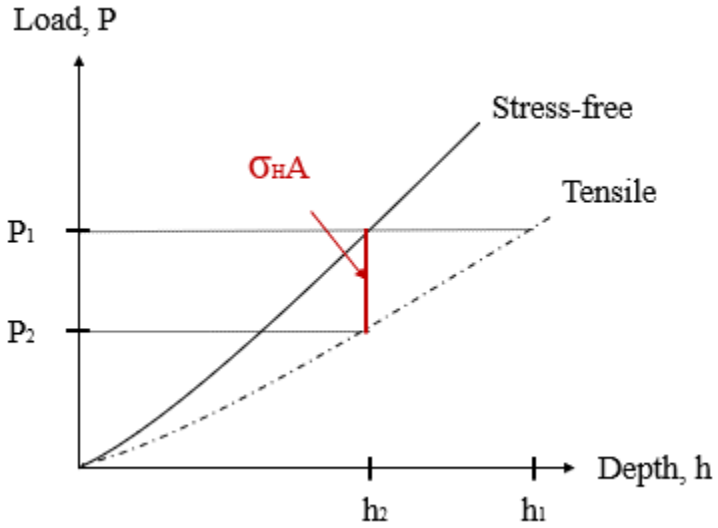

Figure 51. Tensile Residual Stress, Load Controlled

$$P_0 = P + \sigma_H A \tag{20}$$

$$P_0 = P - \sigma_H A \tag{21}$$

Since the previous tests were performed using load-controlled nanoindentation, equation 21 was further examined. To determine the actual area due to the tensile residual

stress, equations 13, 14, and 16 were substituted into equation 21. Equation 17 was then utilized to simplify the manipulated equation, which resulted in equation 22, the true contact area.

$$K_0 {h_0}^{m_0} = Kh^m - \sigma_H(D_0h^2 + D_1h + D_2h^{1/2}+\dots)$$

$$\frac{K_0 {h_0}^{m_0}}{Kh^m} = \frac{Kh^m}{Kh^m} - \frac{\sigma_H(D_0h^2+D_1h+D_2h^{1/2}+\dots)}{Kh^m}$$

$$\frac{p_{ave}A_0}{p_{ave}A} = 1 - \frac{\sigma_H}{p_{ave}}$$

$$\frac{A_0}{A} = 1 - \frac{\sigma_H}{p_{ave}}$$

$$A_0 = A - \frac{\sigma_H A}{p_{ave}}$$

$$A = A_0 + \frac{\sigma_H A}{p_{ave}} \quad (22)$$

In the derived area equation, the unstressed area was known due to the calibrated area function, the average pressure could be determined based on the unstressed sample's load and area, and the differential load could be measured from the power-fitted loading curves. Thus, the theoretically true contact area could be calculated. Once the area was known, the hydrostatic or residual stress could be determined based on the force differential equation.

5.2.2 Compressive Residual Stress

For a biaxial compressive residual stress at the surface, the method used for the tensile residual stress cannot be applied because the uniaxial stress could cause a loss of contact at the contact perimeter [59]. Thus, the contact surface must be examined more closely through Figure 52 [59].

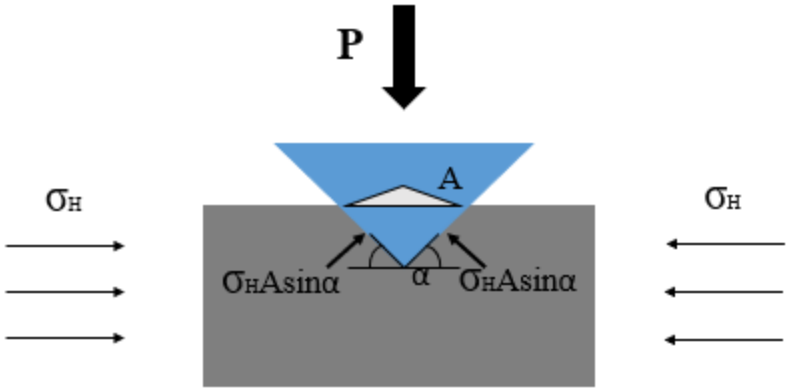

Figure 52. Compressive Residual Stress Diagram

The component of the residual compressive stress on the surface acts normal to the inclined indenter face [59]. For the Berkovich indenter, the angle with respect to the surface is 22°. Thus, the load differential required an additional sinα term (equation 23).

$$dP = \sigma_H A sin\alpha \tag{23}$$

Similarly to the tensile residual stress derivation, the relationship between the stressed (compressive) and unstressed loads are different between the depth and load controlled methods, as shown in Figure 53 and 54 [59]. Therefore, the load differential relationship for the depth-controlled is presented as equation 24, and the load-controlled is equation 25.

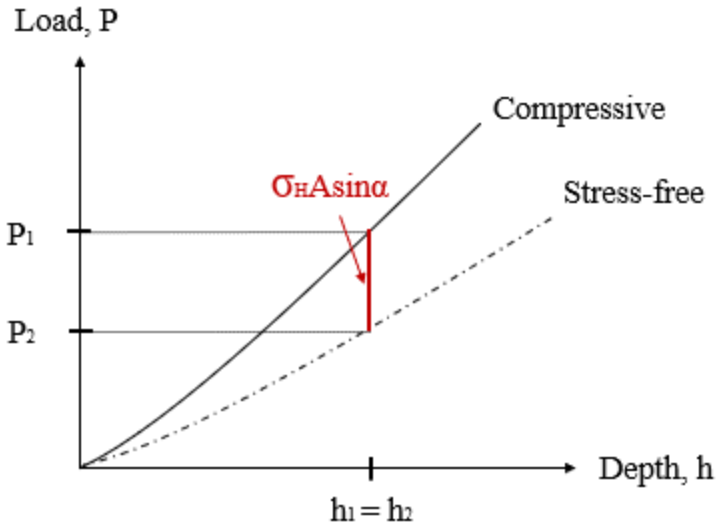

Figure 53. Compressive Residual Stress, Depth Controlled

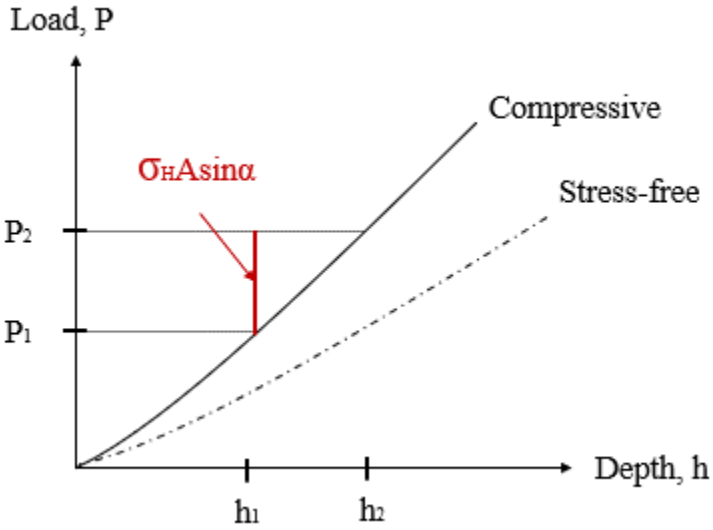

Figure 54. Compressive Residual Stress, Load Controlled

$$P_0 = P - \sigma_H A sin\alpha \tag{24}$$

$$P_0 = P + \sigma_H A sin\alpha \tag{25}$$

Utilizing the load-controlled equation, as well as the previously defined load, area, and average pressure, the true contact area was found (equation 26).

$$K_0 {h_0}^{m_0} = Kh^m + \sigma_H (D_0 h^2 + D_1 h + D_2 h^{1/2} + \ldots) sin\alpha$$

$$\frac{K_0 {h_0}^{m_0}}{Kh^m} = \frac{Kh^m}{Kh^m} + \frac{\sigma_H(D_0h^2+D_1h+D_2h^{1/2}+\ldots)sin\alpha}{Ch^m}$$

$$\frac{p_{ave}A_0}{p_{ave}A} = 1 + \frac{\sigma_H sin\alpha}{p_{ave}}$$

$$\frac{A_0}{A} = 1 + \frac{\sigma_H sin\alpha}{p_{ave}}$$

$$A = A_0 - \frac{\sigma_H A sin\alpha}{p_{ave}} \quad (26)$$

Once the true area is known due to a compressive stress, the residual stress can be determined based on the force differential equation.

5.3 Results

Based on the results from Chapter 3 and Chapter 4, as well as the application of Suresh's method, the possible residual stresses for the DED Ti-6Al-4V sample were calculated. When applying the necessary equations, the stress-free surface was assumed to be the first row in the substrate. Based on that assumption, the loading curves in relation to the unstressed curve were then defined as being either compressive or tensile. In addition, the initial depth values of 0 through 300 nm were truncated due to the power fitted loading curves overlapping and not representing the true behavior of the experimental data. As the depth increased, a clearer distinction between each curve was seen and utilized for finding a more accurate residual stress calculation.

The residual stresses were determined for depth increments of 10 nm until 1150 nm and averaged based on row. The magnitude of the residual stresses for each method are presented in Figure 55 and Figure 56 with respect to the height of the sample. For Figure 55 and Figure 56, the multi-load indentation residual stress values were taken at the same height as the single indentation. However, for presentation and clarity purposes, a slight translation of height was done.

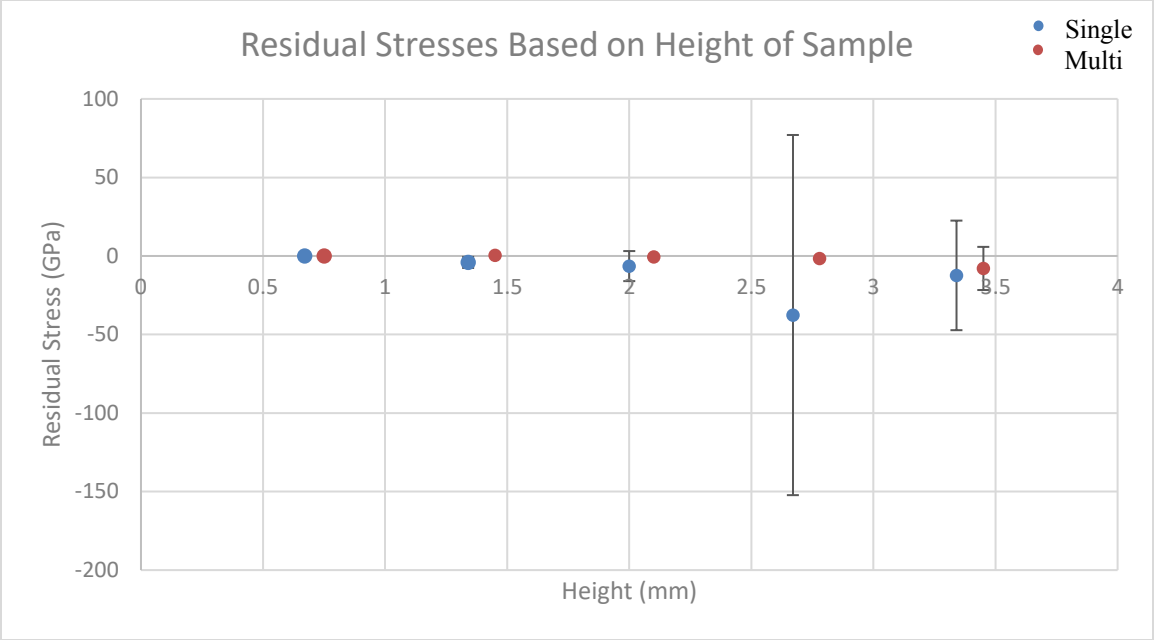

Figure 55. Residual Stresses

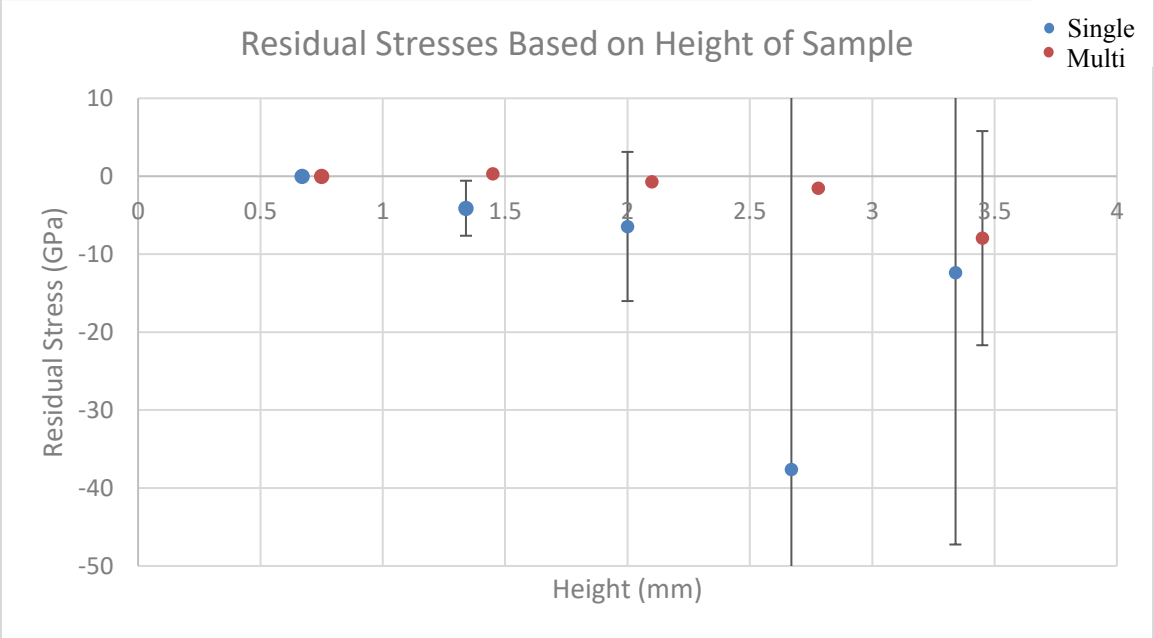

Figure 56. Residual Stresses Magnified

5.4 Discussion

Based on Suresh's method, the residual stresses for each nanoindentation technique were calculated. It was determined that there was a compressive behavior present along the

cross-section, except for the second row (y=1.34 mm) of the multi-load indentation. At this particular point, there was barely any stress relative to the assumed stress-free point due to the closeness in results. However, based on Suresh's methodology, this row had minor tensile residual stress.

When considering the magnitudes of the residual stresses, their behavior along the cross-section of the sample was directly related to the hardness and elastic modulus behavior. When the material increased in hardness, the residual stress had also increased. In addition, in the single indentation results, row 4 (y=2.67 mm) showed to be the maximum nanoindentation hardness. This behavior was seen through the residual stresses, where it had the maximum value at 37 GPa. In addition, this particular height had a large variation. This could have been due to its steep curvature compared to the other positions. This also indicated that the stresses changed more with respect to depth into the material.

Regarding the multi-load indentation, an increasing trend was seen, which was anticipated due to the loading curves curvature. Other researchers have documented that with an increase in sample height, the residual stresses were seen to increase as well [5,12]. One study investigated the residual stress of SLM stainless steel based on sample height [5]. Three different specimens of different heights were made, and the technique utilized to determine the residual stresses was the X-ray diffraction method [5]. For each sample built, measurements 4 mm apart were taken [5]. Each sample indicated that the layer nearest to the base exhibited a compressive stress, and a maximum compressive stress existed at the center of the build height [5]. As the height increased beyond the middle, the stresses became more tensile [5]. This was explained to be due to the initial contraction of the material [5]. When additional layers were built, compression of the underlying layers

occurred, thus causing compressive residual stresses near the base plate [5]. As for the tensile stresses, it was believed that as more layers were added, the heat accumulated and lowered the temperature difference between the layers [5]. Therefore, a transition from compressive to tensile stresses would occur [5]. The smallest sample height that had this behavior was 10 mm tall [5]. Based on the DED Ti-6Al-4V part utilized in this study, a 4 mm test area may not have been a large enough thickness to portray the behavior seen in the steel sample.

When comparing both nanoindentation techniques, the single indentation resulted in higher residual stresses than the multi-load indentation. This occurrence could be due to the nanoindentation positions and the surrounding microstructure or the amount of elastic recovery that was achieved. It could be possible that by indenting multiple times, the stresses in the vicinity were slightly relaxed. In addition, less variance was seen for the multi-load indentation. This made sense due to the variance being based on the residual stress and depth into the surface. As mentioned, DED Ti-6Al-4V was considered a textured material. When repeatedly loading and unloading, a more consistent representation of the material behavior could be achieved. Therefore, this could have related to the small standard deviation compared to the single indentation tests.

Another concern with the results was the magnitude at which the residual stresses were calculated to exist. The residual stresses were deemed to be on the order of gigapascals; thus, the stress values exceeded the yield strength of wrought Ti-6Al-4V. This did not agree with the assumption that only elastic residual stresses would be present. Therefore, the model chosen may not have accurately represented the stresses that were in the part. However, it has been documented for various AM materials that the residual

stresses have been beyond the yield strength [12]. For example, a study was done on DMLS Ti-6Al-4V in which X-ray diffraction was used to measure the residual stresses [12]. The results showed that the maximum residual stress was near the substrate and exceeded the ultimate yield strength of wrought Ti-6Al-4V [12]. However, the residual stresses in that study were not as large as the stresses in this nanoindentation study. This could be due to processing parameters, investigative techniques, and microstructural influences. For the nanoindentation results found, it was possible that the stress values were inflated due to additional hardness induced by the microstructure. While using methods like X-ray diffraction and hole-drilling techniques, the results would be less influenced by the microstructure.

5.5 Conclusion

The residual stresses along the cross-section of a DED Ti-6Al-4V sample were investigated using Suresh's nanoindentation method. Due to the relation of the loading curves and the determination of the possible true contact area, the relative residual stresses were seen to be compressive and become larger as the sample height increased. The compressive nature of the stress near the substrate was anticipated due to the contraction of the material as it was heated and solidified. Thus, the layering and heating process induced distortion between the layers and increased along the part height. In addition, when considering the single indent results, it is possible that the residual stress behavior decreased near the top of the deposition due to the relation with the free surface. The free surface may have caused less constrain, thus, it reflected a relaxation in the residual stresses. However, to compare with documented studies, the stresses determined in this analysis were large. This could be due to the influence of the microstructure that was not

considered when utilizing the mathematical derivation. Further investigation is necessary to understand the extent at which the microstructure affected the nanoindentation results.

Chapter 6: Conclusion and Future Works

With the additive manufacturing process, DED, documented anisotropy has been found to directly relate to the processing parameters. Ideally, finding an optimum combination of parameters would be necessary to ensure functionality of the AM part. However, in order to optimize the process, the effects and relationship between mechanical properties, porosity, and residual stress must be understood. Therefore, determining the causes and magnitudes of residual stress, as well as the hardness and the elastic modulus, was imperative to understand the material and part functionality.

In this study, various methods were utilized to understand the possible variation along the cross-section of a DED Ti-6Al-4V sample. For example, the microstructure was investigated based on elemental composition and α phase ratio. It was determined that there was a minor decrease in vanadium and a possible variation in the α phase when comparing the different heights along the sample. A decrease in vanadium has been documented by other researchers when using the DED process due to uneven material distribution. In addition, a possible change in microstructure could have occurred due to an inconsistent cooling rate when the material was built. Therefore, it would be of interest to examine more positions along the sample to develop a more accurate representation for the DED sample. Similarly, the images used and the binary conversion to differentiate the α and β phases should be further considered by using additional methods to increase the accuracy of the results.

In addition, nanoindentation was utilized to determine the mechanical properties. The results showed that an increase in nanoindentation hardness and elastic modulus was present when increasing in height of the sample. This phenomenon was plausible and can

be due to the increase in residual stresses or the existence of a finer microstructure. Both features are characteristic of DED materials due to the energy source and large temperature gradients in the part as it is built layer by layer.

Based on the results from various nanoindentation techniques, a mathematical model derived by Suresh was used to determine the potential residual stresses in the part. It was calculated that, with respect to the base plate, an increase in compressive residual stresses were present with an increase in sample height. In addition, a slight decrease in residual stress existed as the top of the sample was reached. This could be due to the proximity of the free surface and it causing less constrain on the material. The increase in compressive stresses would be beneficial due to the increase fatigue strength that would result from resistance to crack propagation. However, porosity and microstructure were not considered in this model, and thus could have affected the nanoindentation results.

Therefore, for future works, a more thorough investigation into the overall influences of the nanoindentation results would be helpful in stating a firm conclusion about the material behavior. To further understand the results, another technique to find residual stresses should be implemented for comparison of the residual stresses determined in Chapter 5. Another method could include X-ray diffraction, which utilizes the interplanar spacing of stressed and unstressed lattices in the material. This method is believed to be less influenced by microstructure and would help to check the validity of the Suresh method on DED Ti-6Al-4V parts.

References

[1] Schijve, J. (2009). Residual Stress. In J. Schijve (Eds.), *Fatigue of Structures and Materials* (pp. 89-104). https://doi.org/10.1007/978-1-4020-6808-9_4

[2] Taylor, C. A., Wayne, M. F., and Chiu, W. K. S. (2003). Residual stress measurement in thin carbon films by Raman spectroscopy and nanoindentation. *Thin Solid Films*, 429, 190-200.

[3] Jang, J. (2009). Estimation of residual stress by instrumented indentation: A review. *Journal of Ceramic Processing Research*, 10, 391-400.

[4] Tong, J., Bowen, C. R., Persson, J., and Plummer, A. (2016). Mechanical properties of titanium-based Ti-6Al-4V alloys manufactured by powder bed additive manufacture. *Journal of Materials Science and Technology*, 33, 138-148. https://doi.org/10.1080/02670836.2016.1172787

[5] Liu, Y., Yang, Y., and Wang, D. (2016). A study on the residual stress during selective laser melting (SLM) of metallic powder. *International Journal of Advanced Manufacturing Technology*, 87, 647-656. doi:10.1007/s00170-016-8466-y

[6] Casavola, C., Campanelli, S. L., and Pappalettere, C. (2008). Experimental analysis of residual stresses in the selective laser melting process. Proceedings of the XIth International Congress and Exposition. Society for Experimental Mechanics Inc.

[7] Yadroitsava, I., Grewar, S., Hattingh, D. G., and Yadroitsev, I. (2015). Residual stress in SLM Ti6Al4V alloy specimens. *Materials Science Forum*, 828-829, 305-310. doi:10.4028/www.scientific.net/MSF.828-829.305

[8] "Contour." (2018). VEQTER Residual Stress Experts. Retrieved on 15 Mar. 2018 from http://www.veqter.co.uk/residual-stress-measurement/contour

[9] Zhu, L., Xu, B., Wang, H., Wang, C. (2015). Measurement of residual stresses using nanoindentation method. *Solid State and Materials Sciences*, 40(2), 77-89. doi:10.1080/10408436.2014.940442

[10] Lee, Y., Ji, W., and Kwon, D. (2004). Stress measurement of SS400 steel beam using the continuous indentation technique. *Society for Experimental Mechanics*, 55-61. doi:10.1177/0014485104039750

[11] Atar, E., Sarioglu, C., Demirler, U., Kayali, E. S., and Cimenoglu, H. (2003). Residual stress estimation of ceramic thin films by X-ray diffraction and indentation techniques. *Scripta Materialia*, 48, 1331-1336. https://doi.org/10.1016/S1359-6462(03)00019-8

[12] Yadroitsava, I. and Yadroitsev, I. (2015). Residual stress in metal specimens produced by direct metal laser sintering. *South African Journal of Industrial Engineering*, 614-625.

[13] Khan, M. K., Fitzpatrick, M. E., Hainsworth, S. V., and Edwards, L. (2011). Effect of residual stress on the nanoindentation response of aerospace aluminum alloys. *Computational Materials Science*, 50, 2967-2976. https://doi.org/10.1016/j.commatsci.2011.05.015

[14] LaFontaine, W. R., Paszkiet, C. A., Korhonen, M. A., and Li, C. (1991). Residual stress measurements of thin aluminum metallizations by continuous indentation and x-ray stress measurement techniques. *Journal of Materials Research*, 6, 10, 2084-2090. https://doi.org/10.1557/JMR.1991.2084

[15] Wong, K. V. and Hernandez, A. (2012) A review of additive manufacturing. *International Scholarly Research Network (ISRN) Mechanical Engineering*, 1-11. doi:10.5402/2012/208760

[16] Bian, L., Thompson, S. M., and Shamsaei, N. (2015). Mechanical properties and microstructural features of direct laser-deposited Ti-6Al-4V. *Journal of Metals*, 67, 629-638. doi:10.1007/s11837-015-1308-9

[17] Zhai, Y., Galarraga, H., and Lados, D. A. (2016). Microstructure, static properties, and fatigue crack growth mechanisms in Ti-6Al-4V fabricated by additive manufacturing: LENS and EBM. *Engineering Failure Analysis*, 69, 3-14. http://dx.doi.org/10.1016/j.engfailanal.2016.05.036

[18] Wolff, S., Lee, T., Faierson, E., Ehmann, and Cao, J. (2016). Anisotropic properties of directed energy deposition (DED)-processed Ti-6Al-4V. *Journal of Manufacturing Processes*, 24, 397-405. http://dx.doi.org/10.1016/j.jmapro.2016.06.020

[19] Yan, M. and Yu, P. (n.d.) An overview of densification, microstructure and mechanical property of additively manufactured Ti-6Al-4V – Comparison among selective laser melting, electron beam melting, laser metal deposition and selective laser sintering, and with conventional powder metallurgy. Chapter 5. 1-30. http://dx.doi.org/10.5772/59275

[20] Frazier, W. (2014). Metal additive manufacturing: A review. *Journal of Materials and Performance*, 23, 1917-1928. doi:10.1007/s11665-014-0958-z

[21] Kruth, J. P., Leu, M. C., and Nakagawa, T. (1998). Progress in additive manufacturing and rapid prototyping. *CIRP Annals*, 47, 525-540.

[22] Pederson, R. (2002). Microstructure and phase transformation of Ti-6Al-4V [PDF document]. Retrieved from https://www.diva-portal.org/smash/get/diva2:991369/FULLTEXT01.pdf

[23] Froes, F. H. (2015). Titanium: Physical metallurgy, processing, and applications. ASM International. 141-147.

[24] Oliveira, V., Silva, M., Pinto, C., Suzuki, P., Machado, J., Chad, V., and Barboza, M. (2015). Short-term creep properties of Ti6Al4V alloy subjected to surface plasma carburizing process. *Journal of Materials Research and Technology*, 4, 359-366. doi:10.1016/j.jmrt.2015.05.006

[25] Sterling, A. J., Torries, B., Shamsaei, N., Thompson, S. M.m and Seely, D. W. (2015). Fatigue behavior and failure mechanisms of direct laser deposited Ti-6Al-4V. *Materials Science & Engineering A*, 655, 100-112. http://dx.doi.org/10.1016/j.msea.2015.12.026

[26] Sterling, A. J., Torries, B., Shamsaei, N, and Thompson, S. M. (2016). *Data in Brief*, 6, 970-973. http://dx.doi.org/10.1016/j.dib.2016.01.059

[27] Knowles, C. R., Becker, T. H., and Tait, R. B. (2012). Residual stress measurements and structural integrity implications for selective laser melted Ti-6Al-4V. *South African Journal of Industrial Engineering*, 23, 119-129.

[28] ASTM Standard E3-11, 2017, "Standard Guide for Preparation of Metallographic Specimens," ASTM International, West Conshokocken, PA, 2017, www.astm.org.

[29] "Energy dispersive X-Ray spectroscopy (EDS)." (2014). Materials Evaluation and Engineering, Inc. Retrieved from https://www.mee-inc.com/hamm/energy-dispersive-x-ray-spectroscopyeds/

[30] Erinosho, M. F., Akinlabi, E. T., and Pityana, S. (2016). Exploration of microstructure and wear behaviour of laser metal deposited Ti6Al4V/Cu composites. *Lasers in Engineering,* 35, 15-16.

[31] Kok, Y., Tan, X. P., Wang, P., Nai, M. I. S., Loh, N. H., Liu, E., and Tor, S. B. (2018). Anisotropy and heterogenity of microstructure and mechanical properties in metal additive manufacturing: A critical review. *Materials and Design*, 139, 565-586. https://doi.org/10.1016/j.matdes.2017.11.021

[32] Heat-Affected Zone (HAZ). (n.d.). In International Association of Drilling Contractors (IADC) Lexicon. Retrieved from http://www.iadclexicon.org/heat-affected-zone-haz/

[33] Rafi, H. K., Karthik, N. V., Gong, H., Starr, T. L., and Stucker, B. E. (2013). Microstructures and mechanical properties of Ti6Al4V parts fabricated by selective laser melting and electron beam melting. *Journal of Materials Engineering and Performance*, 22(12), 3872-3883. doi:10.1007/s11665-013-0658-0

[34] Semiatin, S. L., Fagin, P. N., Glavicic, M. G., Sukonnik, I. M., and Ivasishin, O. M. (2001). Influence on texture on beta grain growth during continuous annealing of Ti-6Al-4V. *Materials Science and Engineering A299*, 225-234.

[35] Wolff, S., Lin, S., Faierson, E., Liu, W. K., Wagner, G., and Cao, J. (2017). A framework to link localized cooling and properties of directed energy deposition

(DED)-processed Ti-6Al-4V. *Acta Materialia*, 132, 106-117. http://dx.doi.org/10.1016/j.actamat.2017.04.027

[36] "Alpha Grain Characterization in Titanium." (n.d.). Clemex Image Analysis Report #258 [PDF document]. Retrieved from http://www.clemex.com

[37] Hayes, B. J., Martin, B. W., Welk, B., Kuhr, S. J., Ales, T. K., Brice, D. A., Ghamarian, I., Baker, A. H., Haden, C. V., Harlow, D. G., Fraser, H. L., and Collins, P. C. (2017). Predicting tensile properties of Ti-6Al-4V produced via directed energy deposition. *Acta Materialia*, 133, 120-133. http://dx.doi.org/10.1016/j.actamat.2017.05.025

[38] Ryu, J. J., Shrestha, S., Manogharan, G., and Jung, J. K. (2018). Sliding contact wear damage of EBM built Ti6Al4V: Influence of process induced anisotropic microstructure. *Metals*, 8(2), 131. doi:10.3390/met8020131

[39] "Ti6Al4V titanium alloy." (n.d.). Arcam AB [PDF document]. Retrieved from http://www.arcam.com/wp-content/uploads/Arcam-Ti6Al4V-Titanium-Alloy.pdf

[40] Caiazzo, F., Alfieri, V., Astarita, A., Squillace, A., and Giuseppe, B. (2017). Investigation on laser welding of Ti-6Al-4V plates in corner joint. *Advances in Mechanical Engineering*, 9(1), 1-9. doi:10.1177/1687814016685546

[41] Yan, L., Chen, X., Li, W., Liou, F., and Newkirk, J. (2016). Direct laser deposition of Ti-6Al-4V from elemental powder blends. *Rapid Prototyping Journal*, 22(5), 810-816. https://doi.org/10.1108/RPJ-10-2015-0140

[42] Moharrami, N. (2013). "Extracting reliable mechanical properties using the nanoindentation technique," Doctor of Philosophy, Newcastle University, Newcastle upon Tyne U. K.

[43] Dean, J., Wheeler, J. M., and Clyne, T. W. (2010). Use of quasi-static nanoindentation data to obtain stress-strain characteristics for metallic materials. *Acta Materialia*, 58, 3613-3623. doi:10.1016/j.actamat.2010.02.031

[44] Fischer-Cripps, A. C. (2011). *Nanoindentation*. 3rd ed. doi:10.1007/978-1-4419-9872-9

[45] Li, X. and Bhushan, B. (2002). A review of nanoindentation continuous stiffness measurement technique and its application. *Materials Characterization*, 48, 11-36.

[46] Oliver, W. C. and Pharr, G. M. (2004). Measurement of hardness and elastic modulus by instrumented indentation: Advances in understanding and refinements to methodology. *Journal of Materials Research*, 10(1), 3-20.

[47] Ramirez, J. (2010). Cyclical nanoindentation stress-strain measurement. Nanovea [PDF document]. Retrieved from https://www.nanovea.com

[48] Lee, Y. H. and Kwon, D. (2003). Estimation of biaxial surface stress by instrumented indentation with sharp indenters. *Acta Materialia*, 52, 1555-1563.

[49] Lee, Y. H. and Kwon, D. (2003). Measurement of residual-stress effect by nanoindentation on elastically strained (100) W. *Acta Materialia*, 49 459-465. doi:10.1016/S1359-6462(03)00290-2

[50] Merle, B., Maier, V., and Durst, K. (2014). Experimental and theoretical confirmation of the scaling exponent 2 in pyramidal load displacement data for depth sensing indentation. *Scanning*, 36, 526-529.

[51] Merle, B., Maier, V., Goken, M. and Durst, K. (2012). Experimental determination of the effective indenter shape and ε-factor for nanoindentation by

continuously measuring the unloading stiffness. *Journal of Material Research*, 27(1), 214-221. doi:10.1557/jmr.2011.245

[52] Engineering ToolBox, (2003). Young's modulus – tensile and yield strength for common materials. [online] Retrieved from https://www.engineeringtoolbox.com/young-modulus-d_417.html

[53] Saber-Samandari, S. and Gross, K. A. (2010). The use of thermal printing to control the properties of calcium phosphate deposits. *Biomaterials*, 21, 6386-6393. doi:10.1016/j.biomaterials.2010.05.012

[54] ASTM E2546-07, "Standard Practice for Instrumented Indentation Testing," ASTM International, West Conshokocken, PA, 2007, www.astm.org.

[55] Nanovea. (2015). *M1 tester: User guide*. Publisher location: Publisher.

[56] Yu, J., Rombouts, M., Maes, G., and Motmans, F. (2012). Material properties of Ti6Al4V parts produced by laser metal deposition. *Physics Procedia*, 39, 416-424. doi:10.1016/j.phpro.2012.10.056

[57] Corbin, D. J., Nassar, A. R., Reutzel, E. W., Kistler, N. A., Beese, A. M., and Michaleris, P. (2016). Impact of directed energy deposition parameters on mechanical distortion of laser deposited Ti-6Al-4V. *Solid Freeform Fabrication*, 670-679.

[58] Warren, A. W., Guo, Y. B., and Weaver, M. L. (2006). The influence of machining induced residual stress and phase transformation on the measurement of subsurface mechanical behavior using nanoindentation. *Surface & Coatings Technology*, 200, 3459-3467. doi:10.1016/j.surfcoat.2004.12.028

[59] Suresh, S. and Giannakopoulos, A. E. (1998). A new method for estimating residual stresses by instrumented sharp indentation. *Acta Mater*, 46(16), 5755-5767.